This is to certify that the

dissertation entitled

Dissipative Quantum Tunneling of a Single Defect in a Submicron Bi wire below 1 K

presented by

Kookjin Chun

has been accepted towards fulfillment
of the requirements for

Ph. D degree in Physics

Norman O. Birge
Major professor

Date 11-17-93

DISSIPATIVE QUANTUM TUNNELING OF A SINGLE DEFECT IN A SUBMICRON Bi WIRE BELOW 1 K

By

Kookjin Chun

A DISSERTATION

Submitted to
Michigan State University
in partial fulfillment of the requirements
for the degree of

DOCTOR OF PHILOSOPHY

Department of Physics and Astronomy
and Center for Fundamental Materials Research

1993

ABSTRACT

DISSIPATIVE QUANTUM TUNNELING OF A SINGLE DEFECT IN A SUBMICRON Bi WIRE BELOW 1 K

By

Kookjin Chun

The quantum mechanical problem of a particle tunneling in a double-well potential is of great theoretical and experimental interest. Interaction of the tunneling system with a dissipative environment can have a striking effect on the tunneling dynamics. A very interesting case is that of ohmic dissipation, which occurs when an atom tunnels in a metal in the presence of conduction electrons.

We have studied the electrical resistance of submicron Bi wires at low temperature. Due to quantum interference of the conduction electrons, the resistance is highly sensitive to the motion of even a single scattering center. We observe discrete switching of the resistance due to the motion of bistable defects in the sample. We have measured the tunneling rates of a particular defect over the temperature range 0.1-2 K and magnetic field range 0-7 T. The energy asymmetry, ε, of this defect varied over the range 40-420 mK depending on the value of the magnetic field. The temperature dependence of the tunneling rates is qualitatively different for the cases $k_B T << \varepsilon$ and $k_B T >> \varepsilon$. We observe that for $k_B T << \varepsilon$, the fast rate (transition rate from upper state to lower state) is roughly temperature independent and the slow rate (transition from lower state to upper state) decreases

exponentially, as expected from a simple picture of spontaneous emission and stimulated absorption. When $k_B T >> \varepsilon$, however, both rates increase as the temperature is lowered, as predicted by dissipative quantum tunneling theory. We fit our data to the theory and discuss the defect-electron bath coupling parameter α, and the renormalized tunneling matrix element Δ_r.

We have also studied the effect of Joule heating on the dynamics of the defect in the same sample. The ratio of the fast and slow transition rates of a defect depends on temperature through the detailed balance relation, $\gamma_f / \gamma_s = e^{\varepsilon / k_B T}$. We interpret this ratio as a local thermometer. When $\varepsilon / k_B T > 1$, this ratio is sensitive to small changes in the temperature T seen by the defect. Since the defect is strongly coupled to the conduction electrons in the sample below 1 K, we interpret its sensitivity to drive current as an indication of electron heating. As the drive current increases, the defect temperature approaches a power law dependence with the drive current, independent of the nominal lattice temperature. The data are consistent with a simple model of heating, and strong thermal coupling between the defect and the electron bath. We also tried to measure the electron temperature directly, based on the temperature dependence of the amplitude of the resistance fluctuations, δR. Since δR depends only on the electron temperature, we expected δR would serve as a good electron thermometer. The electron thermometer does not follow the simple heating model.

To my dearest wife Young Ae and my children, James and Christine

ACKNOWLEDGEMENTS

I would like to thank my advisor Professor Norman O. Birge for making my contribution to this research a remarkably cherishable and enjoyable experience. His invaluable guidance and extraordinary patience made this work much more fruitful and rewarding. I thank Professors Michael Dubson, S. D. Mahanti, Daniel Stump and Horace Smith for serving on my guidance committee. Special thanks go to Professor Dubson for the use of his lithographic facilities for sample fabrication.

The friendship and valuable help of fellow students was indispensible. Paul McConville provided a lot of valuable effort on this work and helped me with many discussions in performing the experiment. Jeong Sun Moon is also acknowledged for his valuable opinions about the experiment, and his cheerful personality.

I thank my family for continous aid and support, which I sometimes take for granted. Special thanks go to my parents who have been patiently waiting for this moment for a long time. Finally, I thank my wife Young Ae, who has always been with me, giving invaluable support both mentally and physically. Without her warm support and patience, this moment would have never come to pass.

This work was supported by the National Science Foundation under grant DMR-9023458.

TABLE OF CONTENTS

Appendices

LIST OF TABLES

LIST OF PUBLICATIONS

1. "Dissipative Quantum Tunneling of a Single Defect in Bi"; Kookjin Chun and Norman O. Birge, Phys. Rev. **B 48**, 11500 (1993)

2. "A Single Defect Thermometer as a Probe of Electron Heating in Bi"; Kookjin Chun and Norman O. Birge, submitted and accepted to Phys. Rev. **B.**

3. "Dissipative Quantum Tunneling of Defects in a Mesoscopic Metal"; Norman O. Birge, Kookjin Chun, Glen B. Alers and Brage Golding, to appear in Physica **B**, Proceedings of the 20th International Conference of Low Temperature Physics, Eugene, OR, August 1993.

LIST OF FIGURES

Chapter 1

Introduction

The conduction electrons in a metal are scattered from lattice vibrations, impurities and structural defects while traveling through the sample, giving rise to the electrical resistance of the sample. At high temperatures, the dominant scattering mechanism is the scattering of the electrons from the lattice vibrations, which is inelastic scattering. At low temperatures, on the other hand, the scattering is from static impurities and lattice defects, which is elastic scattering. Only recently it has been appreciated that these two types of scattering mechanisms have fundamentally different effects on the resistance of metals. Inelastic scattering destroys the quantum-mechanical phase coherence of the electronic wavefunction, while elastic scattering does not. Hence quantum interference phenomenon are important at low temperature, when the phase coherence length, L_ϕ, is longer than the elastic mean free path, l_e. In particular, the exact spatial configuration of the elastic scattering centers is important because the interference of multiply scattered electrons depends on the locations of the scatterers.[1-3] Since the electron wavefunction is phase-coherent over the distance L_ϕ, the electrical resistance can not be derived simply by adding independently the contributions from all the defects and impurities. Instead, the scattering amplitudes from different trajectories interfere quantum-mechanically, so that the conductance

(inverse of the resistance) is due to the coherent sum of the amplitudes.

The consequences of quantum interference are greatly enhanced in mesoscopic samples, samples with dimensions comparable to L_ϕ. Such samples have properties that differ drastically from those of the "ensemble average".[4] The effects of quantum interference have been widely observed in small samples with fixed impurity configuration at low temperature. By varying a magnetic field, which causes the interference to change in a complicated way, one observes time-independent fluctuations of the conductance as a function of the magnetic field.[5] These conductance fluctuations are aperiodic and vary in detail between samples. For mesoscopic samples, the magnitude of the conductance fluctuations is of order e^2/h. The universality of these fluctuations at low temperature has been confirmed in several different metallic systems. This phenomenon is called "universal conductance fluctuations".[1-3]

One of the most interesting predictions of the theory of the universal conductance fluctuations is that the conductance of a mesoscopic sample can be quite sensitive to the motion of a single atom.[6-7] In a very small sample the motion of a single defect can totally scramble the phase of the electron wavefunction and produce as much conductance change as moving the entire configuration of defects. For a weakly disordered one-dimensional or two-dimensional mesoscopic sample, the magnitude of the conductance fluctuations is approximately e^2/h. This dynamic feature of universal conductance fluctuations can be used to study microscopic phenomena such as the dynamics of defects in metals and their relationship to $1/f$ noise. It has been proposed[8]

that $1/f$ noise is caused by the linear superposition of a large number of independent defect motions with a broad distribution of transition rates.

The dynamics of such defects arises from two different mechanisms: thermally activated hopping over the potential barrier at high temperatures and quantum tunneling through the barrier at low temperatures. At high temperatures, a defect in a double-well potential hops back and forth between the two wells over the barrier. The distribution of defect hopping rates is given from the broad distribution of activation energies. As the temperature is lowered, the defect dynamics will cross over to tunneling though the barrier.

When the temperature is lower than the vibrational energy in a single-well, the defect motion is limited to the quantum tunneling between the lowest levels in each well. In a metal, the defect interacts strongly with the bath of conduction electrons, leading to dissipative quantum tunneling.[9] The dissipation has three primary influences on the tunneling dynamics: (1) the tunneling is an incoherent rate process rather than a coherent oscillation between the two wells (due to the strong coupling of the defect with electron bath); (2) the tunneling matrix element is renormalized due to the interactions with high-energy electron-hole excitations; and (3) the tunneling rates can increase with decreasing temperature, in some circumstances. The tunneling rates of a particular defect can be characterized by three parameters: the energy asymmetry, ε, which is the energy difference between the ground states in the two wells, the renormalized tunneling matrix element, Δ_r, and the coupling constant between the defect and the bath of electrons, α. The energy asymmetry, ε, for a single defect

has been observed to vary with magnetic field[10], as predicted[11] based on local fluctuations in the electron density that occur in disordered metals.

This thesis describes measurements of the dynamics of a single defect in a submicron Bi wire over the temperature range 0.1 - 2.0 K. The temperature dependence of the defect tunneling rates were measured for several values of magnetic field up to 7 Tesla. The temperature dependence of the tunneling rates shows excellent agreement with the predictions of dissipative quantum tunneling theory for each value of the magnetic field . Fits of the experimental tunneling rates to the theory for each magnetic field yield values of ε, α and Δ_r as a function of the magnetic field. The value of ε varies randomly with field, consistent with previous work.[10-11] The question of whether α and Δ_r vary with magnetic field is more difficult to address quantitatively, because the theoretical fits to the data depend only weakly on α over the experimental temperature range. A scaling plot shows that our data is consistent with the hypothesis[12] that α and Δ_r are independent of field for this defect, which was assumed in a previous study.[12]

A study of the effect of Joule heating on the dynamics of the defect is also included in the thesis. We measured the transition rates of a single defect and the amplitude of the resistance fluctuations as a function of the drive current for different lattice temperatures. The ratio of the two transition rates of a defect depends on temperature through the detailed balance relation, $\gamma_f / \gamma_s = e^{\varepsilon/k_B T}$. We interpret this ratio as a local thermometer at the defect site. Since the defect is strongly coupled to the conduction electrons in the sample below 1 K, we

interpret its sensitivity to drive current as an indication of electron heating. The Joule heating data are consistent with a model of electron heating studied previously.[13] However, we could not determine the absolute electron-phonon scattering rate from this experiment, due to the sample geometry.

The organization of the thesis is as follows: Chapter 2 presents the theoretical background necessary to understand the experiments; Chapter 3 contains the details about the experimental techniques and apparatus used in this work. Chapter 4 is the central part of the thesis and illustrates the data-acquisition, analysis, and interpretation in terms of the theory of dissipative quantum tunneling. Chapter 5 describes the effect of Joule heating on the defect dynamics and its use as a local thermometer to study electron heating. The thesis ends with a summary in Chapter 6.

References

1. P. A. Lee and A. D. Stone, Phys. Rev. Lett. **55**, 1622 (1985).
2. B. L. Al'tshuler, and B. I. Shklovskii, Zh. Eksp. Teor. Fiz. **91**, 220 (1986) [Sov. Phys. JETP **64**, 127 (1986)].
3. P. A. Lee, A. D. Stone, and H. Fukuyama, Phys. Rev. **B 35**, 1039 (1987).
4. A. D. Stone, Phys. Rev. Lett. **54**, 2692 (1985).
5. C. P. Umbach, S. Washburn, R. B. Laibowitz and R. A. Webb, Phys. Rev. **B 30**, 4048 (1984).
6. B. L. Al'tshuler and B. Z. Spivak, Pis'ma Zh. Eksp. Teor. **42**, 363 (1985) [JEPT Lett. **42**, 447 (1985)].
7. S. Feng, P. A. Lee and A. D. Stone, Phys. Rev. Lett. **56**, 1960, 2772(E) (1986).
8. P. Dutta and P. M. Horn, Rev. Mod. Phys. **53**, 497 (1981).
9. See "Quantum Tunneling in Condensed Matter", ed. Yu. Kagan and A. J. Leggett, Elsevier, New York 1993; also A. J. Leggett et al., Rev. Mod. Phys. **59**, 1 (1987) and references therein.
10. N. M. Zimmerman, B. Golding and W. H. Haemmerle, Phys. Rev. Lett. **67**, 1322 (1991).
11. B. L. Al'tshuler and B. Z. Spivak, Pis'ma Zh. Eksp. Teor. Fiz. **49**, 671 (1989) [JEPT Lett. **49**, 772 (1989)].
12. B. Golding, N. M. Zimmerman and S. N. Coppersmith, Phys. Rev. Lett. **68**, 998 (1992).
13. M. L. Roukes et al., Phys. Rev. Lett. **55**, 422 (1985).

Chapter 2

Background and Theory

2.1 Classical Transport

The classical picture of electrical conduction in metals is based on Drude theory[1]. It is assumed that when atoms of a metallic element are brought together to form a metal, the nuclei and the core electrons bound to them form the immobile metallic ions, while the valence electrons are allowed to wander freely through the metal. These electrons, called conduction electrons, are responsible for the conduction mechanism in metals. The disorder in the lattice gives rise to electrical resistance. This disorder comes from vibrations of lattice atoms, impurities and lattice defects. All of these cause scattering of the conduction electrons, with a total scattering rate $1/\tau_t = 1/\tau_e + 1/\tau_\phi$. Here, τ_e is the elastic scattering time, i.e. the time between collisions with the impurities and defects, while τ_ϕ is the inelastic scattering time, i.e. the time between inelastic scattering events, such as electron-phonon and electron-electron collisions. Figure 2.1 (a) illustrates the scattering of conduction electrons off the lattice vibrations, impurities and defects.

In the presence of an applied electric field, the relationship between the electric field $\mathbf{E}$ at a point in the metal and the current density $\mathbf{j}$ is $\mathbf{j} = \sigma \mathbf{E}$, where σ is the conductivity. From kinetic theory, the current density is given as $\mathbf{j} = -ne\mathbf{v}$, where n is the electron carrier density. Assuming that an electron emerges from each scattering

event in a random direction, the average electronic velocity is $\mathbf{v}_{ave} = -\frac{e\mathbf{E}\tau_t}{m}$, where e is the electron charge and m is its mass and accordingly, $\mathbf{j} = \left(\frac{ne^2\tau_t}{m}\right)\mathbf{E}$. Equating the two expressions of $\mathbf{j}$, one has $\sigma = \frac{ne^2\tau_t}{m}$. The conductance is $G = \sigma A / L$, where A is the cross-sectional area of the sample and L is the length. At high temperatures, inelastic phonon scattering is the dominant scattering mechanism. As the temperature decreases, τ_ϕ increases due to the decreasing rate of electron-phonon collisions, but τ_e remains finite, leading to a residual conductance, $G = \sigma_0 A / L$, where $\sigma_0 = \frac{ne^2\tau_e}{m}$. Figure 2.1 (b) shows the graph of resistivity versus temperature for a typical metal.

2.2 Quantum Transport

Drude theory has a questionable feature when applied to metals at low temperature, since it treats elastic and inelastic scattering as having equivalent effects on the conductivity. In a metal at sufficiently low temperatures, one has to distinguish between the two different scattering processes because the inelastic scattering time τ_ϕ exceeds the elastic scattering time τ_e by several orders of magnitude. In this regime, τ_ϕ is called the "phase-breaking scattering time" because an electron loses its phase coherence through inelastic scattering events. Quantum interference[2], whose effect is neglected in the classical picture, becomes important in a metallic sample whenever the phase coherence length, L_ϕ, is longer than the elastic mean free path, l_e. L_ϕ is defined as the distance an electron can

diffuse elastically without undergoing an inelastic collision. It is related to the phase-breaking time, τ_ϕ, by the relation $L_\phi = \sqrt{D\tau_\phi}$, where $D = \frac{1}{3} v_F l_e$ is the diffusion constant and v_F is the Fermi velocity. Since the electronic wavefunction is phase-coherent over the distance L_ϕ, the electrical resistance cannot be derived simply by adding independently the scattering rates from all the defects and the impurities. Instead, the amplitudes of multiply scattered waves from different trajectories interfere quantum-mechanically, so that the conductance is due to the coherent sum of the amplitudes. The effect of quantum interference gives rise to quantum corrections to the electrical conductance.[2]

The consequences of quantum interference are greatly enhanced in mesoscopic samples where the sample size is comparable to L_ϕ. One consequence of quantum interference on the length scale L_ϕ is the phenomenon of "universal conductance fluctuations"[3-6] to be described below. These fluctuations can be observed by applying a magnetic field to a metal sample or by the motion of scattering centers.

2.2.1 Universal Conductance Fluctuations (static)

The application of a magnetic field is one way to change the relative phases of the interfering electron waves, resulting in the phenomenon of universal conductance fluctuations[3]. Electron wave functions enclosing a magnetic flux exhibit a phase shift introduced by the magnetic vector potential $\mathbf{A}$[7]. Figure 2.2 (a) shows a schematic diagram of the phase change due to the magnetic field. Consider the

complete trajectory A → B → C → D → A, encircling the area through which a magnetic flux penetrates. Electrons traveling along one trajectory A → B → C will acquire a phase change and electrons in the other trajectory A → D → C will experience a different phase change. Changing the magnetic flux enclosed by these trajectories will tune the phase change along one trajectory by an amount $\delta_1 = \frac{e}{\hbar}\int_{A\to B\to C}\mathbf{A}\cdot d\mathbf{l}$ and $\delta_2 = \frac{e}{\hbar}\int_{A\to D\to C}\mathbf{A}\cdot d\mathbf{l}$ along the other trajectory. The phase tuning appears as a cycle of constructive and destructive interference of the wave functions, the period of the cycle being $\Phi_0 = h/e$. In a one-dimensional ring in the mesoscopic size range with a flux Φ through the hole, there is coherent interference between the waves propagating through each arm of the ring. The magnetic field changes the relative phase of the contributions from each arm of the ring by an amount $2\pi\Phi/\Phi_0$, giving rise to magnetoresistance fluctuations periodic in Φ_0.

For a mesoscopic wire in a magnetic field, the electrons traveling along the different paths acquire different phase changes from the field because trajectories enclose different amounts of flux. Thus, variation of the field causes the phase dependent contribution to the conductance to vary randomly, and gives rise to an aperiodic fluctuation[8] of the resistance. These conductance fluctuation phenomena are, therefore, sample specific and aperiodic. The other unique feature of the fluctuations is that they are time-independent and reproducible within a given sample. These fluctuations have a universal magnitude $\delta G \approx e^2/h$ for samples with dimensions smaller than L_ϕ. The universal conductance fluctuations induced by the field are static, and are called the "magnetofingerprint".

2.2.2 Universal Conductance Fluctuations (dynamic)

Another way to observe universal conductance fluctuations is to change the locations of all of the scattering centers, i.e. the impurities and defects[9-10]. Figure 2.2 (b) is a schematic diagram of the phase shift due to the motion of a *single* scatterer in the sample. If the scatterer moves, it changes the phases of all the Feynman-like paths that scatter from this scatterer, resulting in a conductance change. For a disordered metal in the diffusive regime (i.e. when $L_\phi >> l_e$), multiple elastic scattering is very much like a random walk process with a step size l_e. In quasi one-dimensional systems, each Feynman path actually passes through a given site many times; therefore the motion of a single scatterer will affect all the scattered paths and accumulate sufficient phase shift to change the conductance by $\delta G \approx e^2/h$, as much as if all the scatterers are moved around. In two dimensions the number of sites visited by each Feynman path that traverses a sample of size L is of order $(L/l_e)^2$. This means that a finite fraction of all the Feynman paths pass through a site and the motion of a single defect will alter the phase of all the paths passing through that site. Thus, the motion of a scatterer induces a change in the conductance that is typically a finite fraction of that induced by the motions of all scatterers. In d≥2 dimensions, a fraction $(L/l_e)^{(2-d)/2}$ of the Feynman paths pass through a given site and the conductance change is of order $\delta G \approx e^2/h(L/l_e)^{(2-d)/2}$. The quantitative descriptions are, respectively,[10-11]

(1) 1-D (wire) case : $l_e << L_x \approx L_y << L_z < L_\phi$;

$$(\delta G_1)^2 = C_1 \left(\frac{e^2}{h}\right)^2 \frac{1}{(k_F\, l_e)^2} \alpha(k_F \delta r)\ \frac{l_e L_z}{L_x L_y}$$

(2) 2-D (film) case : $l_e < L_x << L_y = L_z < L_\phi$;

$$(\delta G_1)^2 = C_2 \left(\frac{e^2}{h}\right)^2 \frac{1}{(k_F\, l_e)^2} \alpha(k_F \delta r)\ \frac{l_e}{L_x}$$

(3) 3-D (cubic) case : $l_e << L_x = L_y = L_z = L < L_\phi$;

$$(\delta G_1)^2 = C_3 \left(\frac{e^2}{h}\right)^2 \frac{1}{(k_F\, l_e)^2} \alpha(k_F \delta r)\ \frac{l_e}{L}$$

where C's are constants of order unity which depends on dimensionality. The function $\alpha(x) = 1 - \sin^2(x/2)/(x/2)^2$ accounts for the phase shift due to moving a scatterer a distance δr. L_x , L_y , L_z , are thickness, width and length, respectively.

If more than a single scatterer is moved within a single coherence volume (i.e. a box of dimensions L_ϕ), the effect on the conductance change is additive as long as $\delta G_{box} << e^2/h$. Thus one has

$$(\delta G_{box})^2 = (\delta G_1)^2\ n_s(T)\ V_{box}$$

where $n_s(T)$ is the density of moving scatterers within a single coherence volume V_{box}. The magnitude of the conductance fluctuations is reduced when $k_B T > \hbar \tau_\phi^{-1}$, due to "energy averaging". At finite temperature the incident electron distribution is smeared out over a range $k_B T$ around the Fermi energy E_F. Therefore, the conductance is

the sum of $k_B T/\hbar\tau_\phi^{-1}$ uncorrelated interference patterns, where $\hbar\tau_\phi^{-1}$ is the energy over which the conductance fluctuations are correlated. The conductance fluctuations are reduced in magnitude by $(\hbar\tau_\phi^{-1}/k_B T)^{1/2}$ due to averaging over these $k_B T/\hbar\tau_\phi^{-1}$ uncorrelated patterns. This process is called energy averaging. In this case the expression of $(\delta G_{\text{box}})^2$ is multiplied by the factor $\hbar\tau_\phi^{-1}/k_B T = L_T^2/L_\phi^2$, where $L_T = \sqrt{\hbar D/k_B T}$ is called the thermal length. L_T is the distance over which electrons differing in energy by $k_B T$ become out of phase with each other.

If only one single defect is moving in a one dimensional sample of size $L_z > L_\phi$, the conductance change is

$$\left(\frac{\delta G}{G}\right) = \frac{L_\phi}{L_z}\left(\frac{\delta G_{\text{box}}}{G_{\text{box}}}\right)$$

One can extend this consideration to a two dimensional sample with $L_y, L_z > L_\phi$. In this case, the conductance change is given as

$$\left(\frac{\delta G}{G}\right) = \frac{L_\phi^2}{L_y L_z}\left(\frac{\delta G_{\text{box}}}{G_{\text{box}}}\right)$$

The total conductance G is related to G_{box} by the sample geometry and the standard rules for combining resistors in series and parallel. The two results shown above can both be expressed as

$$\delta G = \frac{L_\phi^2}{L_z^2}\delta G_{\text{box}}$$

For a large sample where all coherence volumes fluctuate, the conductance fluctuations in the different coherence volumes are statistically independent and one combines them classically to obtain the conductance variance. Therefore

$$\left(\frac{\delta G}{G}\right)^2 = \frac{1}{N}\left(\frac{\delta G_{\text{box}}}{G_{\text{box}}}\right)^2$$

where N is the number of coherence boxes in the entire sample.

For a one dimensional or two dimensional sample with dimensions comparable to L_ϕ, the motion of a single scatterer is sufficient to yield a conductance fluctuation comparable to the universal magnitude, e^2/h. The universal conductance fluctuations due to the motion of scatterers are dynamic, in contrast to the static universal conductance fluctuations observed as a function of magnetic field.

2.2.3 Characteristic Magnetic Field Scale

Figure 2.3 (a) shows a magnetofingerprint of a Bi sample with dimensions 3 μm long, 0.15 μm wide, and 10 nm thick at 0.8 K. The magnetofingerprint can be characterized by two quantities, the amplitude of the conductance fluctuations and the characteristic magnetic field scale. This can be seen most easily by calculating the autocorrelation function:

$$C(\Delta B) = \langle \delta G(B)\ \delta G(B+\Delta B) \rangle$$

where the bracket indicates an average over the magnetic field B. A schematic diagram of $C(\Delta B)$ is shown in Figure 2.3 (b). When $\Delta B = 0$, the correlation function $C(\Delta B)$ is equal to the variance, $<\delta G^2>$. As ΔB increases , the fluctuations in δG will tend to vary randomly in sign, and on average, the product will tend to zero at large ΔB. The magnetic field where $C(\Delta B)$ drops to half its maximum value is called the "characteristic magnetic field scale", B_c. B_c is the typical spacing of the peaks and valleys in $\delta G(B)$.

An estimate of B_c can be obtained by the following argument: the largest areas between Feynman paths that interfere quantum-mechanically are of order L_ϕ^2. Putting half a flux quantum through that area will totally alter the interference between those paths. Hence in a two dimensional sample, $B_c \approx \Phi_0 / L_\phi^2$.

2.3 Defect dynamics

If defects in the metal are mobile, they can cause conductance fluctuations in time. The most commonly believed general mechanism for $1/f$ noise in metals is that of defect motion. Such motions can be due to thermal activation of defects at high temperatures, or to quantum tunneling of defects through potential barriers at low temperatures. Dutta, Dimon, and Horn (DDH)[12] showed that low frequency $1/f$ noise in metals over the temperature range 100 - 500 K could be explained as arising from a distribution of thermally activated motions of defects, with typical activation energy scales for hopping in metals (about 1 eV). Feng, Lee, and Stone (FLS) proposed that the sensitivity of the conductance to atomic motions should give rise to $1/f$ noise through the

UCF mechanism at low temperatures.[10] In disordered metals at low temperatures, $1/f$ noise arises from tunneling defects with a broad distribution of potential barrier heights and tunneling distances. A more detailed discussion of $1/f$ noise is given in Appendix A.

In the mesoscopic regime, a connection between quantum tunneling of a single defect and conductance fluctuations offers the chance to study microscopic phenomena which have previously been studied only in the ensemble average.

2.3.1 Defect Dynamics in Different Temperature Regimes

As described above, the dominant dynamics of the defects at high temperatures are thermally activated hopping. A single defect hops with a characteristic time scale τ, where $\tau = \tau_0 \exp(E/k_B T)$, where E is the activation energy for making a transition.[13] A single double-well potential can be characterized by the energy barrier E, and the energy difference between the ground states in each well, called the energy asymmetry, ε.[14] Figure 2.4 (a) shows a schematic diagram for the activation process of a defect over the barrier. At high temperatures, this thermal activation behavior of the defects results from the interaction between the defect and the thermal reservoir of electrons and phonons.

At low temperatures, on the other hand, the defect kinetics are tunneling dominated. In a highly disordered material, one expects the number of active tunneling defects to depend approximately linearly on the temperature.[15] In a mesoscopic sample, the conductance fluctuations due to a *single* defect can be resolved.

When $k_B T << \hbar\omega_0$, where ω_0 is the smallest undamped single-well frequency, the defect tunneling is confined to the lowest states in each well. This quantum system is called a two level system (TLS). In a metal, the temporal behavior of a TLS illustrates the main features of dissipative quantum tunneling,[16] which will be discussed in the next section. Figure 2.4 (b) shows the tunneling behavior between the lowest states in the double-well potential.

For temperatures $k_B T > \hbar\omega_0$, the tunneling mechanism of a single defect is not necessarily described by a simple model. One of the plausible features is a dominant coupling with the lattice phonons. In this regime, phonon energies are much smaller than the potential barrier height, but larger than ω_0. The defect in a well can therefore make transitions to the excited state and tunnel through the barrier to complete the transition to the other well. This process is called "phonon-assisted tunneling". The tunneling rates rapidly decrease with decreasing temperature due to the reduction of transitions to the excited states.

2.3.2 Theory of Dissipative Quantum Tunneling

Consider a single defect that moves in an asymmetric double-well potential with a small bias energy ε between the two ground states located at $\pm q_0/2$ in the defect configuration space. For the case of a nearly-isolated defect (i.e. only weakly interacting with the environment), the defect motion is described by the Hamiltonian

$$H_0 = \frac{\varepsilon}{2}\sigma_z - \frac{\hbar\Delta_0}{2}\sigma_x$$

where ε is the energy asymmetry, Δ_0 is the bare tunneling matrix element given by the WKB approximation as $\Delta_0 = \omega_0 \exp\left(-\sqrt{\frac{2mV_0}{\hbar^2}}\delta r\right)$, and the σ_i are Pauli spin matrices. The tunneling dynamics are, in this case, coherent, and the energy eigenstates are linear combinations of the states in each well.

For a metal at temperature $k_B T << \hbar\omega_0$, the defect tunnels dissipatively, interacting strongly with the bath of conduction electrons. The main features of dissipative quantum tunneling[16] are: (1) incoherent tunneling of the defect, arising from the continuous dephasing of the defect wavefunction by the strong interaction with the electron bath; (2) the renormalization of bare tunneling matrix elements (tunneling matrix element without the interaction with the bath) due to the interaction of the defect with the high-energy (adiabatic) electron-hole excitations, and (3) the low-energy (non-adiabatic) electron-hole excitations directly affect the tunneling dynamics, leading to a striking temperature dependence of the tunneling rates; for $k_B T > \varepsilon$, the rates increase with decreasing temperature, following a power law, $\gamma_f, \gamma_s \sim T^{2\alpha-1}$[17], where α is a coupling parameter which decribes the coupling strength of the defect to the bath excitations. From a theoretical calculation, one has $0 < \alpha < 1/2$ for metals[18].

The theoretical approach to the dissipative quantum tunneling problem proceeds as follows: if the barrier height between the two wells is much larger than the small undamped oscillation frequency, ω_0, in either well, the bare tunneling rate Δ_0 satifies $\Delta_0 << \omega_0$. If, in

addition, $k_B T << \hbar\omega_0$, then the double-well problem can be reduced to an effective, biased two-level system.

The bath of electron-hole excitations can be separated into two classes, which play two quite different roles. The electron-hole excitations of frequency greater than the cut-off frequency, ω_c, are able to follow the tunneling defect adiabatically.[19] This leads to a renormalization of the tunneling matrix element Δ through the relation

$$\Delta = \Delta_0(\omega_c / \omega_0)^{\alpha}. \qquad (2.1)$$

The remaining electron-hole excitations with frequency smaller than ω_c can not follow the defect adiabatically; they are directed toward the center of the double well. This non-adiabatic character of the bath affect the tunneling dynamics of TLS. The assumption of the system being reduced to the effective TLS and the argument of high energy electron-hole excitations give rise to a truncated Hamiltonian, given by

$$H = \frac{\varepsilon}{2}\sigma_z - \frac{\hbar\Delta}{2}\sigma_x + \sigma_z \sum_j G_j (b_j + b_j^{+}) + \sum_j \hbar\omega_j b_j^{+} b_j$$

Caldiera and Leggett[20] showed that the influence of the low energy electron-hole excitations on the tunneling defect can be modelled by a bath of harmonic oscillators. The third term describes the interaction between the defect and the bath, where $b_j^{\dagger}$ and b_j are creation and annihilation operators of the harmonic oscillators, and the G_j are coupling coefficients between the defect and the harmonic oscillators.

The fourth term is the Hamiltonian of the harmonic oscillator bath itself.

The effect of the bath on the defect dynamics depends only on the spectral density[21]

$$J(\omega)=\frac{2}{\hbar^2}\sum_j G_j^2\delta(\omega-\omega_j)$$

For a metal, the spectral density in the continuum limit takes the form $J(\omega)=\alpha\omega$[22]. The coupling of the defect to the bath is characterized in terms of the single parameter α.

In obtaining the tunneling of the defect in the presence of ohmic dissipation due to non-adiabatic electrons, it is also necessary to consider the exclusion of the participation of excitations of arbitrary low energies.[19] Since the defect is not stationary in either well, but spends a finite time τ_i in each well, electrons having energies smaller than $\omega<1/\tau_i$ do not influence the tunneling of the defect. Therefore, the energy of the non-adiabatic electron-hole excitations has not only the upper bound ω_c but also the lower bound Δ_r. From this consideration of the lower bound on the energies of the electron-hole excitations, the tunneling matrix element is *renormalized again* and the renormalized tunneling matrix element Δ_r is obtained as:

$$\Delta_r=\Delta\,(\Delta/\omega_c)^{\alpha/(1-\alpha)} \qquad (2.2)$$

If $\hbar\Delta_r >> \varepsilon,\ \alpha k_B T$, the effects of defect coupling to the electron bath are relatively weak and can be treated as a small perturbation on the

dynamics of the defect. In this regime, the motion of the defect is expected to be a coherent oscillation.[23] If, on the other hand, $\hbar\Delta_r << \varepsilon,\ \alpha k_B T$, then the coupling of the defect is so strong that the rapid fluctuations of the electrons act to break the phase of the tunneling defect so that the tunneling becomes incoherent. The dynamics of the tunneling transitions are characterized by the occupation probability of the defect, $P(t) = \langle\, \sigma_z(t)\, \rangle$, given that for $t < 0$, the particle is localized in the +1 state. According to Leggett et.al[18], the calculation of $P(t)$ is based on the consideration of the path integral over four states ($\sigma_z = \pm 1,\ \sigma_z' = \pm 1$) and transitions between the initial and final diagonal states ($\sigma_z = \sigma_z'$, referred as sojourns) and the off-diagonal states ($\sigma_z = -\sigma_z'$ referred to as blips). Figure 2.5 shows a simplified graphic expression of sojourns and blips. Following their calculation of $P(t)$ for the double-well potential with energy aymmetry ε, one gets:

$$P(t) = -\tanh\left(\frac{\varepsilon}{2k_B T}\right) + \left[1 + \tanh\left(\frac{\varepsilon}{2k_B T}\right)\right] e^{-\gamma t}$$

and a total transition rate of [16,24,25]

$$\gamma = \frac{\Delta_r}{2}\left(\frac{2\pi k_B T}{\hbar\Delta_r}\right)^{2\alpha - 1} \frac{\cosh\left(\frac{\varepsilon}{2k_B T}\right)}{\Gamma(2\alpha)} \left|\Gamma\left(\alpha + i\frac{\varepsilon}{2\pi k_B T}\right)\right|^2 \qquad (2.3)$$

where $\Gamma(x+iy)$ is the complex gamma function. The above equation describes incoherent relaxation with a total transition rate γ. For a

single TLS, the energy asymmetry ε is related to the ratio of the average time spent in each state, averaged over many transitions. This must obey the principle of detailed balance: $\gamma_f / \gamma_s = e^{\varepsilon/k_B T}$. Here, γ_f, γ_s, are the fast and slow transition rates, or the reciprocals of the lifetimes of the excited or ground states, respectively. The total rate equals the sum of the fast and slow rates, $\gamma = \gamma_f + \gamma_s$. From detailed balance, we finally have

$$\gamma_f = \frac{\Delta_r}{4}\left(\frac{2\pi k_B T}{\hbar \Delta_r}\right)^{2\alpha-1} \frac{e^{\varepsilon/2k_B T}}{\Gamma(2\alpha)} \left|\Gamma\left(\alpha + i\frac{\varepsilon}{2\pi k_B T}\right)\right|^2 \qquad (2.4)$$

$$\gamma_s = \gamma_f e^{-\varepsilon/k_B T} \qquad (2.5)$$

For $0 < \alpha < 1/2$ [18], there are two regimes depending on the relative magnitude of T and ε. When $k_B T > \varepsilon$, the tunneling rates increase with decreasing temperature, $\gamma_f, \gamma_s \sim T^{2\alpha-1}$ [17], which is a characteristic feature of dissipative quantum tunneling. When $k_B T < \varepsilon$, the tunneling rates follow a simple picture of stimulated absorption and spontaneous emission. The faster rate γ_f is determined by the sum of the spontaneous and stimulated emission rates, while the slower rate is determined by the stimulated absorption rate. As temperature is lowered, the faster rate is roughly temperature independent and the slower rate decreases rapidly as $e^{-\varepsilon/k_B T}$. Both of these temperature regimes are observed in the experimental data and are discussed in Chapter 4.

References

1. "Solid State Physics", N. W. Ashcroft and N. D. Mermin, Holt, Rinehart and Winston 1976.
2. For review, see G. Bergmann, Phys. Rep. **101**, 1 (1984).
3. P. A. Lee and A. D. Stone, Phys. Rev. Lett. **55**, 1622 (1985).
4. B. L. Al'tshuler, Pis'ma Zh. Eksp. Teor. Fiz. **41**, 530 (1985) [JEPT Lett. **41**, 648 (1985)].
5. B. L. Al'tshuler and D. E. Khmel'nitskii, Pis'ma Zh. Eksp. Teor. **42**, 291 (1985). [JEPT Lett. **42**, 359 (1985)].
6. P. A. Lee, A. D. Stone, and H. Fukuyama, Phys. Rev. **B 35**, 1039 (1987).
7. Y. Aharonov and D. Bohm, Phys. Rev. **115**, 485 (1959).
8. A. D. Stone, Phys. Rev. Lett. **54**, 2692 (1985).
9. B. L. Al'tshuler and B. Z. Spivak, Pis'ma Zh. Eksp. Teor. **42**, 363 (1985) [JEPT Lett. **42**, 447 (1985)].
10. S. Feng, P. A. Lee and A. D. Stone, Phys. Rev. Lett. **56**, 1960, 2772(E) (1986).
11. A. D. Stone, Phys. Rev. **B 39**, 10736 (1989).
12. P. Dutta, P. Dimon, and P. M. Horn, Phys. Rev. Lett. **43**, 646 (1979).
13. P. Dutta and P. M. Horn, Rev. Mod. Phys. **53**, 497 (1981).
14. M. B. Weissman, Rev. Mod. Phys. **60**, 537 (1988).
15. See "Amorphous Solids, Low Temperature Properties", ed. W. A. Phillips, Springer-Verlag, New York, 1981.
16. A. J. Leggett et al., Rev. Mod. Phys. **59**, 1 (1987) and refs. therein.
17. J. Kondo, Physica **124 B**, 25; **125 B**, 279, and **126 B**, 377 (1984).
18. K. Yamada, A. Sakurai and M. Takeshige, Prog. Theor. Phys. **70**, 73 (1983).
19. Y. Kagan and N. V. Prokof'ev, Zh. Eksp. Teor. Fiz. **90**, 530 (1985) [JEPT **63**,1276 (1986)].

20. A. O. Caldeira and A. J. Leggett, Ann. Phys. (N.Y.) **149**, 374 (1983).

21. H. Grabert, Phys. Rev. **B, 46**, 12753, (1992)

22. S. Chakaravarty and A. J. Leggett, Phys. Rev. Lett. **52**, 5 (1984).

23. P. Hanggi, P. Talkner, and M. Borkovec, Rev. Mod. Phys., **62**, 251 (1990).

24. H. Grabert and U. Weiss, Phys. Rev. Lett. **54**, 1605 (1985).

25. M. P. A. Fisher and A. T. Dorsey, Phys. Rev. Lett. **54**, 1609 (1985).

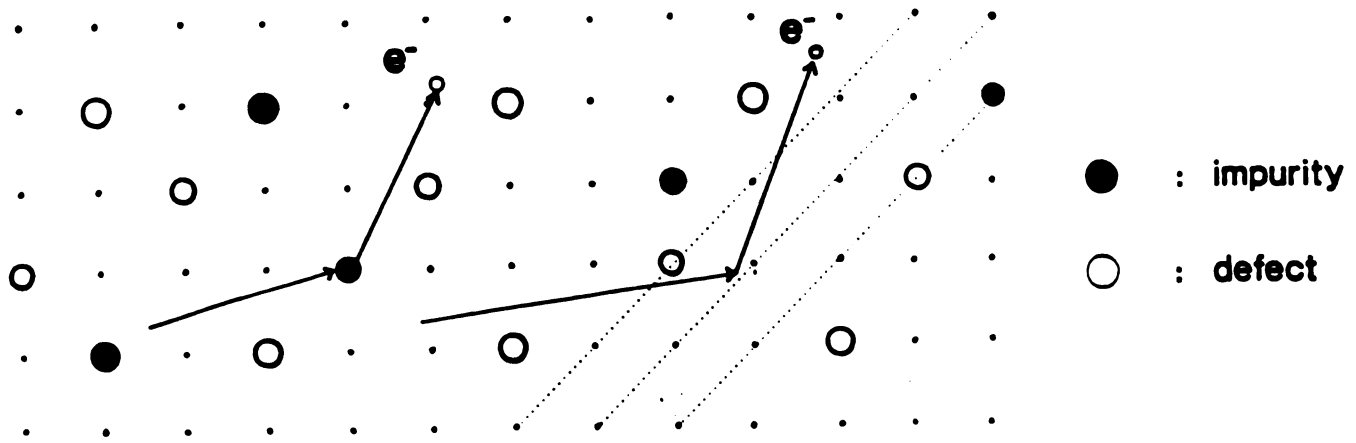

(a)

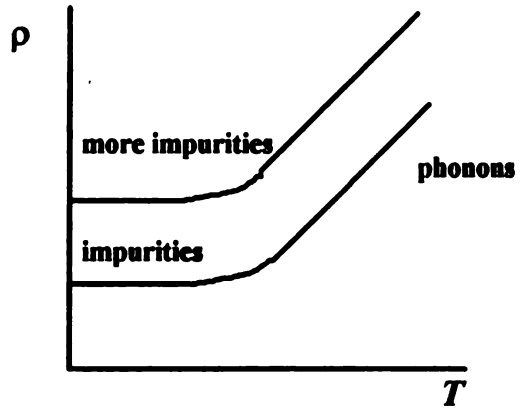

(b)

Figure 2.1 (a) Schematic diagram of the scattering of the conduction electrons off defects, impurities, lattice vibrations and other electrons while they traverse the sample.
(b) Simplified graph of resistivity versus temperature. Due to the decrease of inelastic scattering with decreasing temperature, the resistivity reaches the residual resistivity.

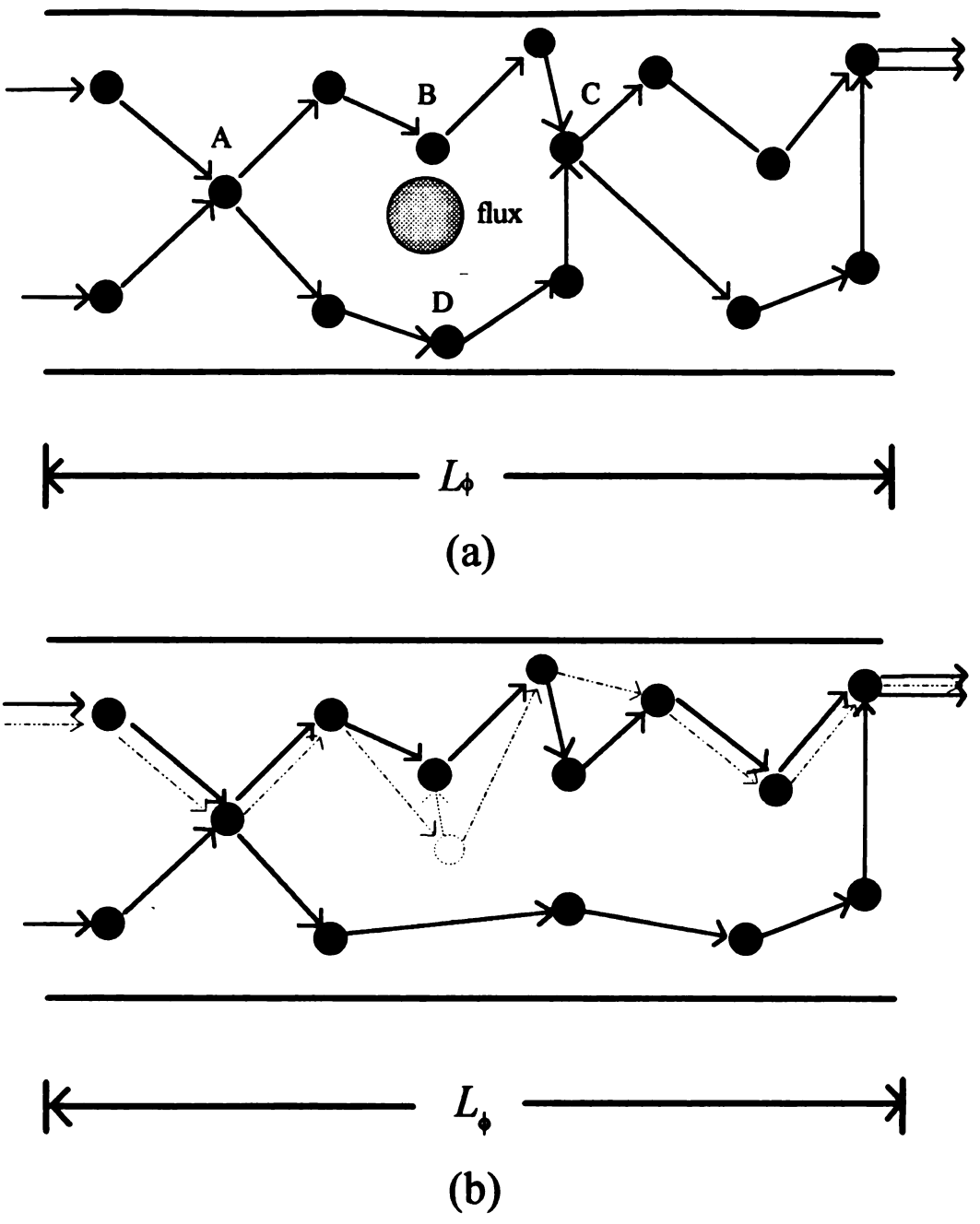

Figure 2.2 (a). The phases of electrons are completely altered by applying a magnetic field, leading to the static conductance fluctuations, called the "magnetofingerprint". (b) By the motion of a single defect, the phases are also changed. The motion of a single defect can induce a conductance fluctuation of order e^2 / h.

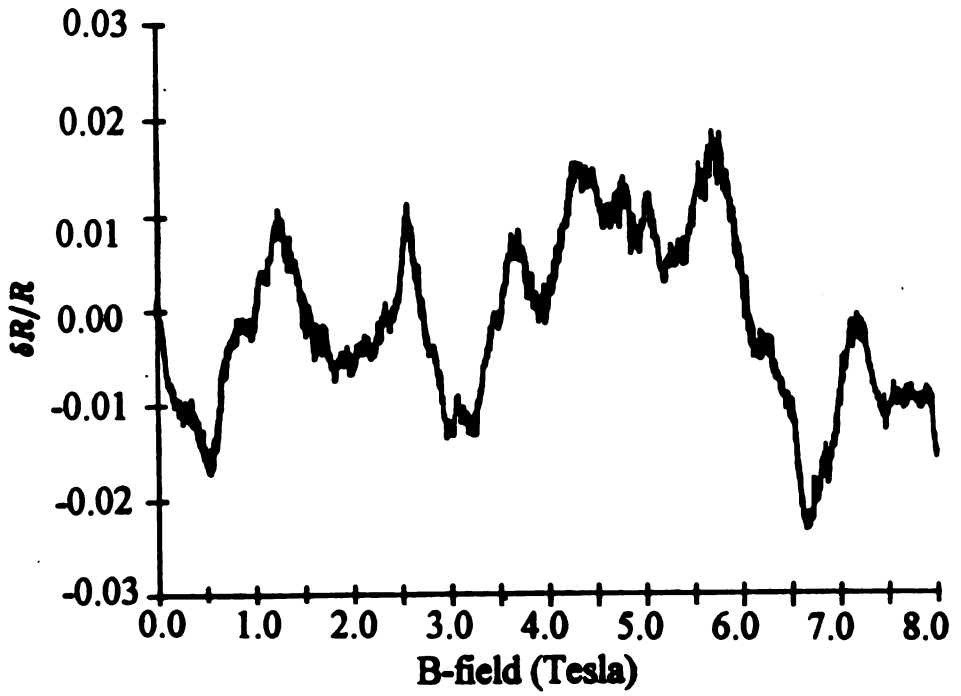

(a)

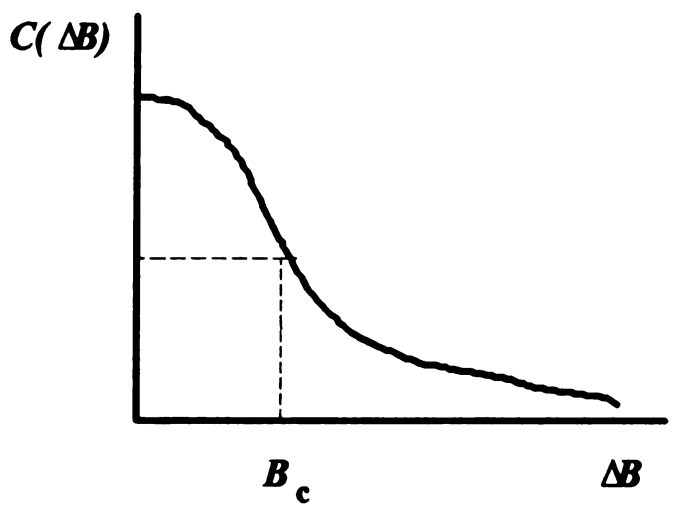

(b)

Figure 2.3 (a) Relative resistance fluctuations, $\delta R/R = -\delta G/G$, as a function of magnetic field (magnetofingerprint) for a Bi wire with dimensions of 3 μm long, 0.15 μm wide, and 10 nm thick. The temperature is 0.8 K. (b) Schematic diagram of the autocorrelation function $C(\Delta B)$ versus magnetic field. The magnetic field where $C(\Delta B)$ drops to half its maximum value is the characteristic field scale, B_c

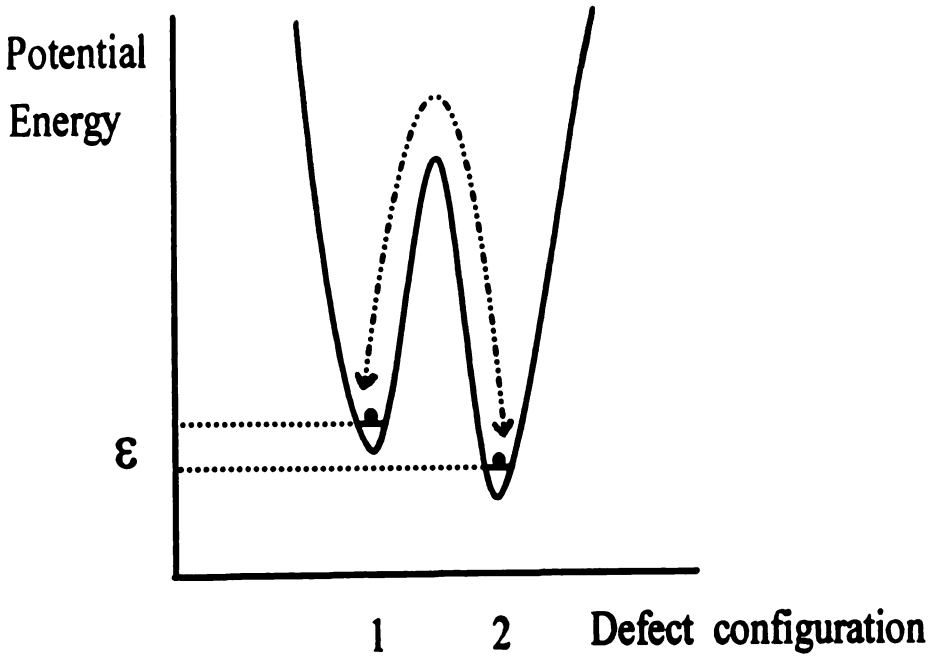

(a)

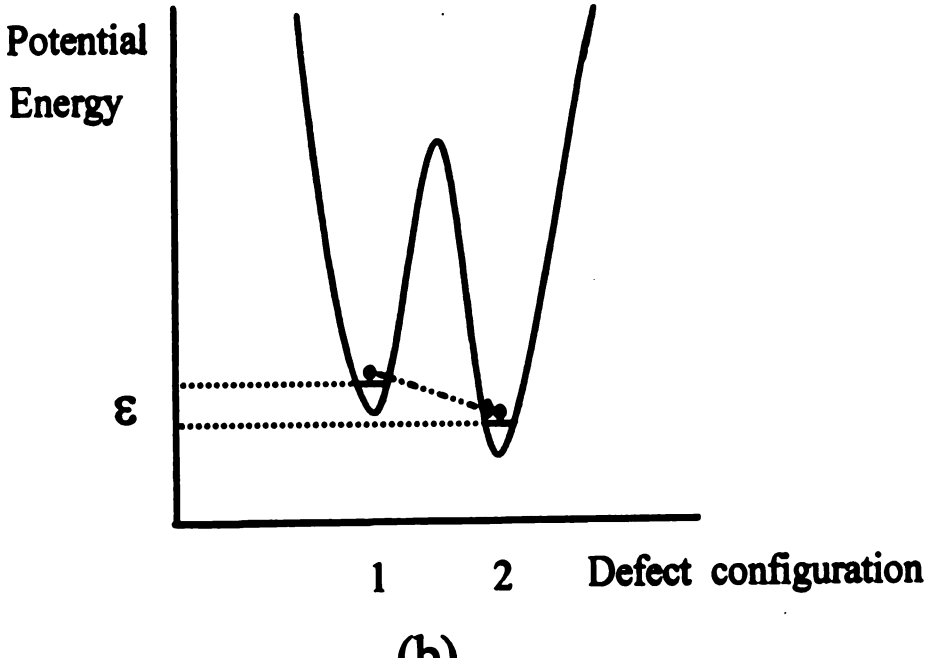

(b)

Figure 2.4 (a) Thermal activation hopping of the defect over the potential barrier at high temperatures. (b) At low temperatures ($k_B T < \hbar\omega_0$), the dynamics of the defect are dominated by tunneling through the barrier between ground states in each well.

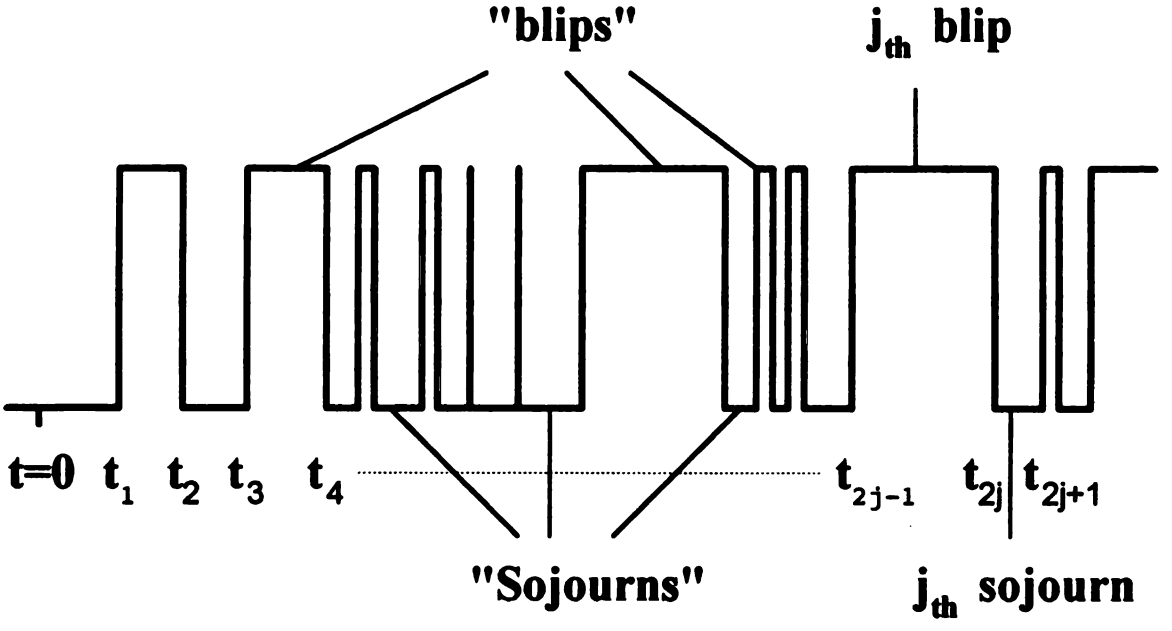

Figure 2.5 Graphic expression for the probability function $P(t)$. The "sojourn" represents no change in the state σ_z, between the initial and final position of the defect after it performs tunneling. The "blip" represents a change in the state during the tunneling process.

Chapter 3

Experimental Methods

3.1 Sample preparation

The samples for this experiment are polycrystalline Bi films 20 nm thick, prepared by thermal evaporation at room temperature onto oxidized Si substrates at a pressure of about 1×10^{-6} Torr. The deposition rates were about 1 nm per second. The films were patterned into five-terminal devices using electron beam lithography.[1-3] Each arm of the sample has nominally identical sample regions with areas of 5×10^{-2} μm^2 (linewidth of 0.1 μm and length of 0.5 μm). Figure 3.1 shows a Scanning Electron Microscope (SEM) picture of a sample and contact pads patterned by electron beam lithography. Each arm of the sample has a resistance of about 1 kΩ.

Electron beam lithography was used to pattern samples with linewidths of 0.1 μm. Operation of the ISI SC-40A Scanning Electron Microscope with a magnification of 15,000× yielded the most reliable and reproducible results. Since the field of view of the SEM is limited to 70 μm at this magnification, the largest attainable width of a pad and the spacing between each pad for five-terminal configuration from electron beam lithography are about 10 μm and 20 μm, respectively. Therefore, it is impossible to make electrical contact between wires of diameter 25 μm and a sample through contact pads patterned only by electron beam lithography. For this reason, we needed both optical and electron beam lithography for patterning the sample and contact pads.

We made primary and secondary contact pads to connect the sample to wires, for measurement of the electrical resistance of the sample. Primary contact pads, patterned by optical lithography, were thermally evaporated gold of thickness 100 nm. The secondary pads, patterned together with the sample by electron beam lithography, were thermally evaporated bismuth 20 nm thick. Figure 3.2 shows SEM pictures of the primary contact pads patterned by optical lithography, and the sample with the secondary pads patterned by electron beam lithography. To make the connection between the primary and the secondary pads, we used a wire shadow technique to make gentle slopes on the edges of the primary pads so that the secondary pads could be connected smoothly. Figure 3.3 shows a simplified schematic diagram of profile of the wire shadow technique. The details about patterning using lithography are given below.

3.1.1 Optical Lithography

Optical lithography, also called "photolithography", is the most common commercial method defining the geometry of electronic devices. Figure 3.4 shows a schematic diagram of the lithography process. We used positive photoresist (Shipley 1800), which is a photosensitive polymer that undergoes a chemical change called "depolymerization" when it is exposed to ultraviolet irradiation. After exposure, the depolymerized area can be dissolved away with the appropriate developer, leading to the generation of the desired pattern.

The photolithography used to make patterns in our experiment consists of two processes. The first process is called "contact

lithography" because the mask for patterning is in firm contact with the photoresist when it is exposed to the ultraviolet light for depolymerization. The process steps are outlined in Table 3.1. The thickness of the spun-on resist layer is about 1.0 - 1.4 μm. The photo-reduced masks are made from high resolution negative films, and are pressed firmly against the resist upon exposure. The exposed substrate is immersed in chlorobenzene to produce a good undercut profile which results from a slower developing rate of the chlorobenzene-smeared upper part of the resist. Additional baking for a short period of time to remove solvent from the resist after immersing is helpful in developing to obtain the desired pattern. Making a good undercut profile is very important in lithography because it avoids the trouble of the metalized pattern being taken off the substrate in the lift-off process. The resolution of the contact pattern is about 10 μm.

If the dimensions of the pattern are near the resolution of the contact lithography, it is not possible to obtain reliable and reproducible patterns. This problem can be overcome by optical projection of the mask onto the resist using an optical microscope. Projection lithography has the same steps as contact lithography and can produce patterns whose dimensions are much smaller and edges are sharper than those of contact lithography. The resolution of projection lithography is better than 1 μm. In our experiment, we used a combination of these two processes through the partial development of the contact pattern, followed by projection exposure and full development. The final pattern has contact leads close enough to overlap with the sample and the secondary pads patterned by electron beam lithography, to be described below.

3.1.2 Electron Beam Lithography

Electron beam lithography is an ideal research tool to define patterns with submicron resolution because of the high quality of electron optics, the availability of high brightness sources to form beams of ultra small diameter and the ability to scan the beam under computer control to define desired patterns. In electron beam lithography a finely focussed beam is scanned in the desired pattern over an electron beam resist which depolymerizes upon electron irradiation. Even though electron optics and electron sources are of a very high quality, and focused beams less than 1 nm in diameter can be generated, it is not readily possible to define a structure on the order of the electron beam size. The resolution of the process is limited by the range of scattered electrons and the intrinsic graininess of the electron beam resist.

When the highly focused, energetic electrons are incident on a solid they undergo scattering within the specimen. Electron scattering is divided into two categories, elastic and inelastic scattering.[4] When elastic scattering occurs, less than 1 eV of energy is transferred from the beam electron to the specimen; this is negligible compared to the incident energy, which is typically 10 keV or more. The electrons are, however, deviated from their incident path as a result of collision. Elastic scattering results from collisions of the energetic electrons with the nuclei of the atoms, partially screened by the bound electrons. A significant fraction of the electron beam emerges from the specimen after having gone through a sequence of elastic scattering events in which the net change in direction is sufficient to be backscattered. (Since the thickness of the Silicon substrate is about

400 μm, it is unlikely for the electrons to pass through the substrate.) These emergent beam electrons are collectively known as backscattered electrons. Due to large angle scattering of these backscattered electrons, the scattering volume of the backscattered electrons is widely spread. Elastic scattering is more probable in high atomic number materials and at low beam energy.

During an inelastic scattering event, energy is transferred to the target atoms and electrons, and the kinetic energy of the beam electron decreases. There are a number of possible inelastic scattering processes, but one of the principal processes under consideration here is the excitation of conduction electrons leading to secondary electron (low energy) emission. The interaction of the beam electrons with the solid can lead to the ejection of loosely bound electrons from the conduction band and these ejected electrons are referred to as secondary electrons. The secondary electrons have a short range scattering effect and are largely responsible for the determination of the resolution in low atomic number materials like polymeric resist.

Polymethl Methacrylate (PMMA) is one of the prime organic resists for electron beam lithography. This positive resist undergoes a chemical change during electron bombardment which renders the material sensitive to developing in a suitable solvent. The developing rate is controlled by the electron dose, e^{-}/cm^{3}, and hence developing for increasing time periods forms contours of electron energy deposition. This contour defines the interaction volume[4], which can be understood in terms of the characteristics of elastic and inelastic scattering, described above. Figure 3.5 is a schematic of the electron interaction volume. For a low-atomic-number matrix like PMMA, inelastic scattering

is more probable, and hence the electron tends to penetrate deeply through the resist into the substrate with relatively little lateral scattering initially to form the "neck" region of the interaction volume. The penetrating electrons lose energy and elastic scattering becomes more probable at lower energy. As a result of elastic scattering, electrons deviate from their initial direction of travel and the lateral scattering contributes to the formation of the "bulbous" region of the interaction volume. This naturally allows us to have a nice undercut profile. However, the generation of the low energy secondary electrons results in a cylindrical exposed volume around the incidence of the beam leading to the broadening of the line width. These are fundamental problems in determining the ultimate resolution, but such effects of electron scattering can be reduced by using high energy electrons. The effect of high electron energy is to narrow the forward scattering distribution and to penetrate through the resist into the substrate deeply enough to smear out the backscattering so that the exposure of a given feature is less influenced by the exposure of its neighbours via the proximity effect.[5]

In our experiment, we fabricated Bi wires with widths as narrow as 100 nm using a bilayer resist process for electron beam lithography. The bilayer resist process uses a bilayer consisting of a layer of PMMA and a layer of copolymer, MMA (methylmethacrylate / methacrylic acid). For high resolution, PMMA is used as the imaging layer and placed at the top, and the copolymer which is more sensitive to electron beam is used as the bottom layer.[6] The processing steps are outlined in Table 3.2. P(MMA/MAA) (KTI I-9 %) is spun on the substrate to produce the bottom layer about 500 nm thick. PMMA(KTI 496-2%) is spun on top of the

copolymer, leaving a layer 200 nm thick. High resolution patterning can be achieved through the use of thin PMMA, but good planarization over the contact pads and better undercut profile are best achieved through the use of a thicker copolymer. Figure 3.6 shows an SEM picture of the profile of the electron interaction in PMMA/MMA bilayer, and a schematic diagram. Electron beam patterning is done with a modified ISI SC-40A SEM, which operates at 30 keV, with the beam position and a beam blanker controlled by a personal computer through a Digital/Analog converter interface. A computer program written in QUICK BASIC was used to control the speed of electron beam writing. The writing speeds were $12\ \mu m/sec$ for the sample and $18\ \mu m/sec$ for the contact pads. The electron beam current was fixed at $I = 1.8\ pA$.

In the SEM, electromagnetic lenses are used to focus the electron beam by the interaction of the electromagnetic field of the lenses on the moving electrons. Commonly used electromagnetic lenses are axially symmetric condenser lenses which consist of windings that induce a magnetic field in the iron core. The condensor lens in combination with the aperture in the probe-forming lens (or objective lens) determines the current in the final probe spot. Although perfect magnetic lenses are assumed to have perfect axial symmetry, machining errors and inhomogeneous magnetic fields within the iron core or asymmetry in the windings cause loss of symmetry, leading to astigmatism. The effect of astigmatism is to produce a stretch of the image in two perpendicular directions. One corrects for the astigmatism in the final objective lens by adjusting the stigmator. The stigmator supplies a weak correcting field to produce the desired symmetrical magnetic field. The stigmator has two major controls, one to correct for the magnitude of

the asymmetry and one to correct for the direction of the asymmetry of the main field. This correction is very important for the patterning of ultra-small samples and should be done prior to the final focusing onto the resist. We used a thin Au film, 50 nm thick, deposited onto a glass substrate as a specimen for correction of astigmatism. After astigmatism was corrected, we used silver paint dashed slightly on the surface of the resist close to the sample site as an object to focus on. Since a small silver cluster at the edge of the silver paint doesn't have a noticeable difference in height from the resist, it provides a nearly perfect focus for patterning.

After exposure, the resists are developed at one time with the same developer [1:3 methyl isobutyl ketone:isopropanol (MIBK :IPA)] at 23 ^{o}C for a minute. An argon ion milling cleaning is used prior to metallization. In ion milling the Ar ions bombard the surface of the resist including that of the patterned area, and remove any resist residue after chemical reaction with developer. After the metallization, the resist surrounding the sample is lifted off by immersing the metallized pattern into a solution of 4:1 methylene chloride and acetone. The resolution of the SEM is about 6 nm in its best operating conditions. With the bilayer process and the considerations made above, we've been successful in fabricating single lines as narrow as 0.06 μm. However, since the real sample is patterned with secondary pads consecutively, we could not totally exclude the proximity effect. Line widths of our samples came out to be about 0.1 μm.

3.2 Electronics

Figure 3.7 shows a simplified schematic diagram of the electronics for our experiment. The five-terminal sample configuration allows the sample to be used as two arms of an ac Wheatstone bridge.[7] With this technique relative changes in the resistance of the two arms can be measured with high sensitivity.

The differential voltage across the bridge due to the change of the resistance of either arm is amplified through a preamplifier (Stanford SR 550), phase-sensitively detected with a lock-in amplifier referred to the drive frequency, and the output connected to digital instruments (analog/digital converter, low pass filter and personal computer) located outside the shielding room. The analog/digital converter is for converting the analog voltage output from the lock-in amplifier to a digitized one. The low pass filter is used to remove any unwanted high frequency noise. When a continuous function is sampled with a sampling interval Δ, its Fourier transform is defined only between the frequencies $-1/2\Delta < f < +1/2\Delta$. This boundary frequency $f_c = 1/2\Delta$ is called the "Nyquist frequency". If an original function that is not bandwidth limited is sampled, then, all of the power spectral density which lies outside of the frequency range $-f_c < f < f_c$ is moved back into that range. This effect is called "aliasing". Any frequency component outside this frequency range is aliased (falsely transformed) into that range by the act of discrete sampling, leading to incorrect Fourier transform of the function. Aliasing can be eliminated only by low pass filtering the original function before sampling. The low pass filter used in the experiment is a Krohn-Hite eight-pole butterworth filter which produces the flattest passband (the region of

frequencies that are relatively unattenuated by the filter) response and has steepness in the transition region from passband to the stopband (the region of significant attenuation). The order of the filter is eight-pole. Increasing the number of poles flattens the passband response and steepens the stopband falloff. It is also used for rejecting line frequency harmonics and higher frequency resistance noise sources in the sample.

The dilution refrigerator is located inside a Lindgren double-electrically-isolated shielded room. The shielded room isolates the refrigerator and electronics from rf (radio frequency) interference, which could otherwise propagate down the sample leads into the refrigerator and heat the electrons in the sample. This problem becomes most severe as the sample size and temperature decrease. The high level analog signals are filtered as they enter or leave the room. Only low-level analog instruments (preamplifier, lock-in amplifier) are kept inside the shielded room. Just inside and outside the shielded room, there are ground breaking boxes to minimize ground loop interference.

The dilution refrigerator has a top loading probe on which the sample and thermometer are mounted. Eighteen low-frequency electrical leads are accessible to the sample region through the top loading probe. The probe is loaded from the top of the dilution refrigerator and slides down to the low temperature region. There are also electrical wires dedicated to measure thermometers near the sample area. One Fisher connector with eighteen electrical leads was used for thermometers of the dilution unit (film burner, cold plate, still, mixing chamber, and 1 K pot) and for heaters of the mixing chamber, film burner and still. All the electrical wires are twisted in pairs or triplets for rejecting

induced magnetic fields when current flows for measurement. For the measurement of temperatures at each unit, home-built conductance bridges which read the conductance of the thermometers are used.

Due to the small size of the sample extreme care is required in handling the sample. Even a static charge from a human body is strong enough to destroy the sample. Therefore, we added sample protection guards which tie the five pads together in the optical lithography process. The guards protect the sample from possible burnout during sample mounting and when leads are attached to the substrate. The guards are disconnected after the sample is silver painted to a pin connector which connects the sample with the electrical leads on the top loading probe. For more precaution, we always wore a grounded wrist strap whenever working with the sample.

3.3 Dilution Refrigerator

Our low-temperature measurements were performed in an Oxford Instruments top-loading helium-3/helium-4 dilution refrigerator in our laboratory. Figure 3.8 shows a simplied schematic diagram of the dilution refrigerator. The principle of operation[8] of the dilution refrigerator is based on the fact that a mixture of the two isotopes of helium separates into two phases -- a concentrate phase which is rich in helium-3 and a dilute phase which is rich in helium-4 --when it is cooled down below a tricritical temperature of 0.86 K. This phase separation occurs in the mixing chamber and cooling is produced there by evaporating helium-3 from the concentrate phase across the boundary to the dilute phase. Helium-3 is pumped away from the still by a room

temperature vacuum pump. The still is maintained at a temperature of 0.6 to 0.7 K by the still heater. The helium-3 is compressed to few hundred milibar and returned to the condenser attached to the 1 K pot where it is precooled and liquified through a high flow impedance. It then passes through the heat exchangers and finally arrives at the mixing chamber. The helium-3 leaving the mixing chamber due to the osmotic pressure between the mixing chamber and the still is used to cool the returning flow of concentrated helium-3 in the heat exchangers. By continuous circulation of helium-3, temperatures as low as 20 mK can be achieved. Since the cooling power of a dilution refrigerator is directly proportional to the flow rate of helium-3, a large cooling power requires very powerful pumps and wide pumping lines. The samples are loaded into the dilute helium phase in the mixing chamber, simplifying thermal grounding. The refrigerator is equipped with a 9-Tesla superconducting magnet for measuring magnetoresistance and magnetofingerprints. To keep the field low near the mixing chamber (for thermometry or other experiments) the magnet has compensation coils.

The top loading probe slides into the refrigerator on a special 'O' ring assembly mounted on top of the vacuum lock. Before inserting the probe, the vacuum lock assembly is pumped using the diffusion pump. When loading a sample into the refrigerator, circulation is stopped, and the mixture is left in a state where it is being cooled by the refrigeration power in the 1 K pot. To introduce the sample, the gate valve is opened and the assembly is lowered slowly into the dilution unit. The lower section of the probe is cooled by the mixture as it passes through the insert and the dilution unit. When the top loading probe is screwed into position, the rotary pump and booster pump are

used to begin circulation of the helium-3 and the dilution unit starts to cool.

3.4 Temperature Calibration of Thermometer

To achieve adequate temperature stability, it was crucial to control the temperature in performing our experiments. A temperature control program was written in Quick Basic and used to control the power supply that supplies current to a heater wrapped around the glass tail of the mixing chamber. With this setup, we controlled the temperature to within 1 % all through the temperature range 0.05 - 1 K. Above 1 K, we controlled the temperature via the pumping speed on the 1 K pot.

Due to the magnetoresistance of the carbon thermometer which measures the temperature of the sample, it was required to calibrate the carbon thermometer as a function of magnetic field. The magnetoresistance of the carbon thermometer was measured at seven different temperatures. At each temperature, the values of magnetoresistance were measured twice at ten different values of the magnetic field up to 7 Tesla, once while increasing the field and immediately after, while decreasing the field. The two results were averaged. The ratio of magnetoconductance to the value of conductance at zero field shows a sharp increase up to 0.5 Tesla and a slow decrease thereafter. We fit our data to the function:

$$\frac{G(T,B)}{G(T,0)} = 1.00 + \frac{a(T)}{B} \cdot (b(T) - B + d(T)B^2) \cdot \frac{c(T)}{e^{a(T)/B} - 1}$$

where $a(T)$, $b(T)$, $c(T)$ and $d(T)$ are polynomials in the zero-field conductance, $G(T,0)$.

A computer program was used to obtain the corresponding $G(T,0)$ value from the given value of $G(T,B)$ measured in the applied magnetic field. The corrected temperature was obtained from $G(T,0)$ and the known temperature calibration of the carbon thermometer. The details about the fitting procedure are described in Appendix B.

References

1. G. J. Dolan and T. A. Fulton, IEEE Electron Device Lett. **4**, 178 (1983).
2. D. J. Bishop, J. C. Licini, and G. J. Dolan, Appl. Phys. Lett. **46**, 1000 (1985).
3. M. J. Rooks, S. Wind, P. McEuen, and D. E. Prober, J. Vac. Sci. Technol. **B 5**, 318 (1987).
4. "Scanning Electron Microscopy and X-Ray Microanalysis", ed., J. I. Goldstein et al., Plenum, New York 1981.
5. K. H. Nicholas, R. A. Ford, H. E. Brockman, and I. J. Stemp, J. Vac. Sci. Technol. **B 1**, 1020 (1983).
6. R. E. Howard, E. L. Hu, and L. D. Jackel, and P. M. Mankiewich, IEEE Trans. Electron Devices **ED-28**, 1378 (1981).
7. J. H. Scofield, Rev. Sci. Instrum. **58**, 985 (1987).
8. See "Experimental Principles and Methods Below 1 K", O. V. Lounasmaa, Academic Press, London and New York 1974.

Table 3. 1 The processing steps of optical lithography.

(1) Clean an oxidized silicon substrate with acetone, methyl alcohol and DI (deionized) water.

(2) Spin photoresist at 5000 rpm for 30 seconds.
(thickness $\approx$ 1.0 μm)

(3) Bake for 30 minutes in air at 95 °C.

(4) Expose with UV (ultraviolet) light using contact mask.

(5) Immerse in chlorobenzene for 10 minutes.

(6) Bake for 10 minutes in air at 75 °C.

(7) Develop for 45 seconds in developer at 23 °C for partial developing.

(8) Clean the substrate with DI water.

(9) Expose in the light source in the optical microscope using projection mask.

(10) Develop for 1 minute in developer at 23 °C.

(11) Evaporate metal.

(12) Liftoff by immersing into acetone.

Table 3. 2 The processing steps of electron beam lithography (bilayer technique).

(1) Clean an oxidized silicon substrate with acetone, methyl alcohol and DI (deionized) water.

(2) Spin KTI I-9 % copolymer at 4000 rpm for 1 minute.
(thickness ≈ 450 nm)

(3) Bake for 1 hour in air at 180 °C.

(4) Spin 496 K PMMA, 2%, at 5000 rpm for 1 minute.
(thickness ≈ 200 nm)

(5) Bake for 1 hour in air at 180 °C.

(6) Expose with electron beam.

(7) Develop for 1 minute in 1:3 MIBK:IPA at 23 °C.

(8) Clean the substrate with IPA and DI water

(9) Clean the substrate with ion milling to remove the resist residue.

(10) Evaporate metal.

(11) Lift-off by immersing in a solution of 4:1 methylene chloride:acetone.

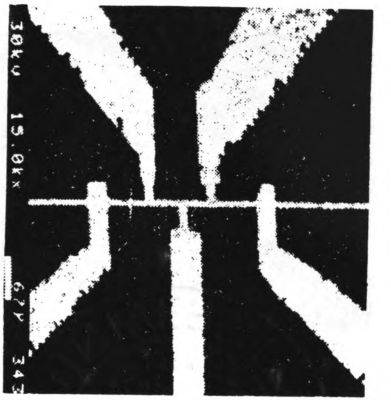

Figure 3.1 (a) SEM picture of a five-terminal Bi sample patterned by electron beam lithography. The dimensions of the sample are 1 μm long, 0.1 μm wide, and 20 nm thick. (b) Schematic diagram of the sample with five leads.

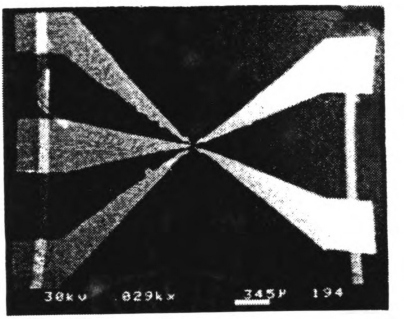

(a)

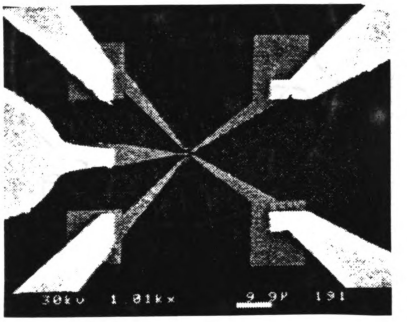

(b)

Figure 3.2 (a) SEM picture of the primary contact pads patterned by optical lithography. (b) SEM picture of the sample with the secondary contact pads patterned by electron beam lithography. The primary contact pads and secondary pads are connected smoothly by the wire shadow technique.

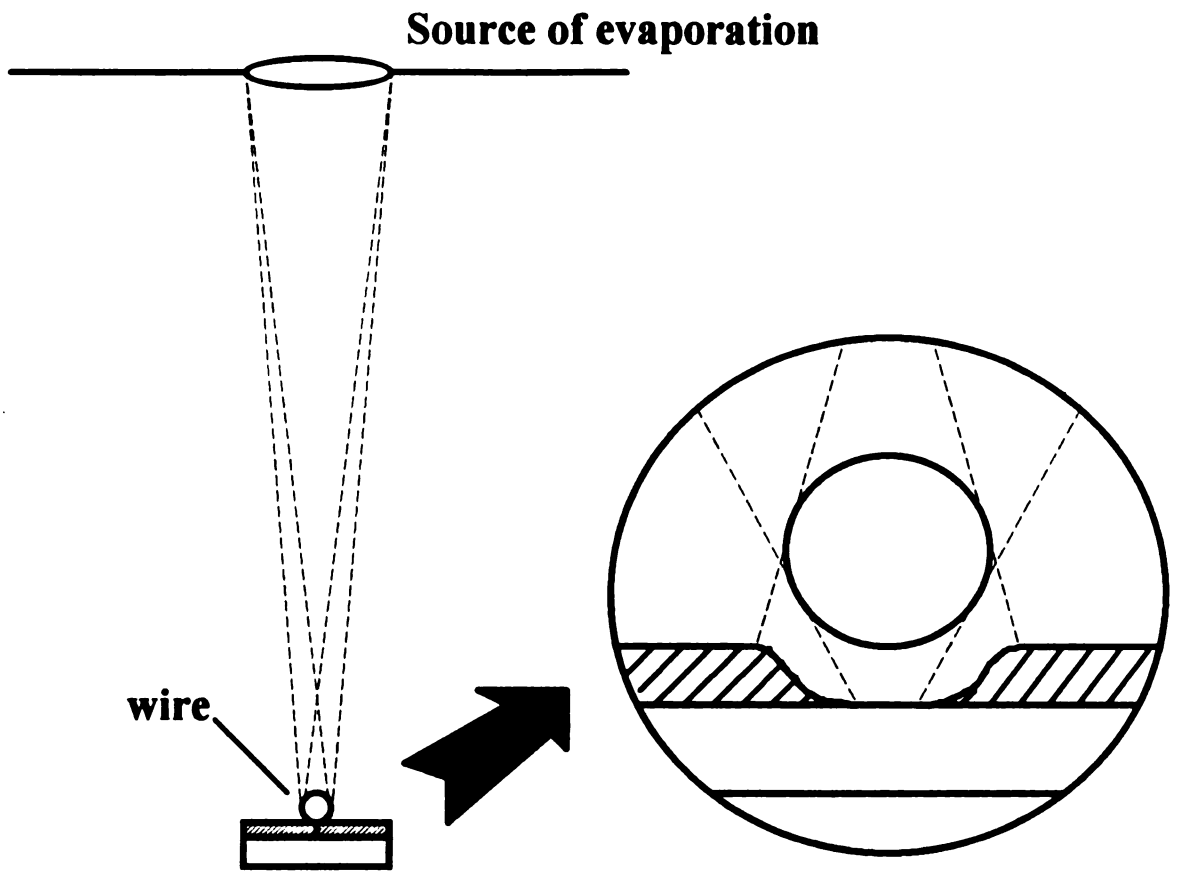

Figure 3.3 Schematic diagram of the wire shadow technique. The shadow of the wire gives rise to gentle slopes on the edges of the primary contact pads. This ensures that the thin secondary pads can make good contact with the primary pads.

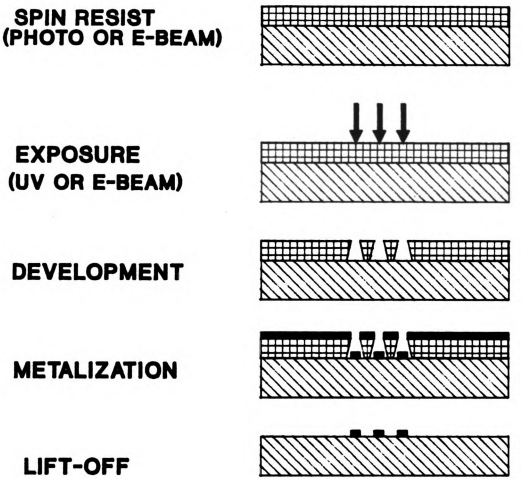

Figure 3.4 Schematic diagram of the lift-off process. The process applies to both optical and electron beam lithography with different types of the resist and different source of exposure. The resolution of optical lithography is about 1 μm, and 10 nm for electron beam lithography.

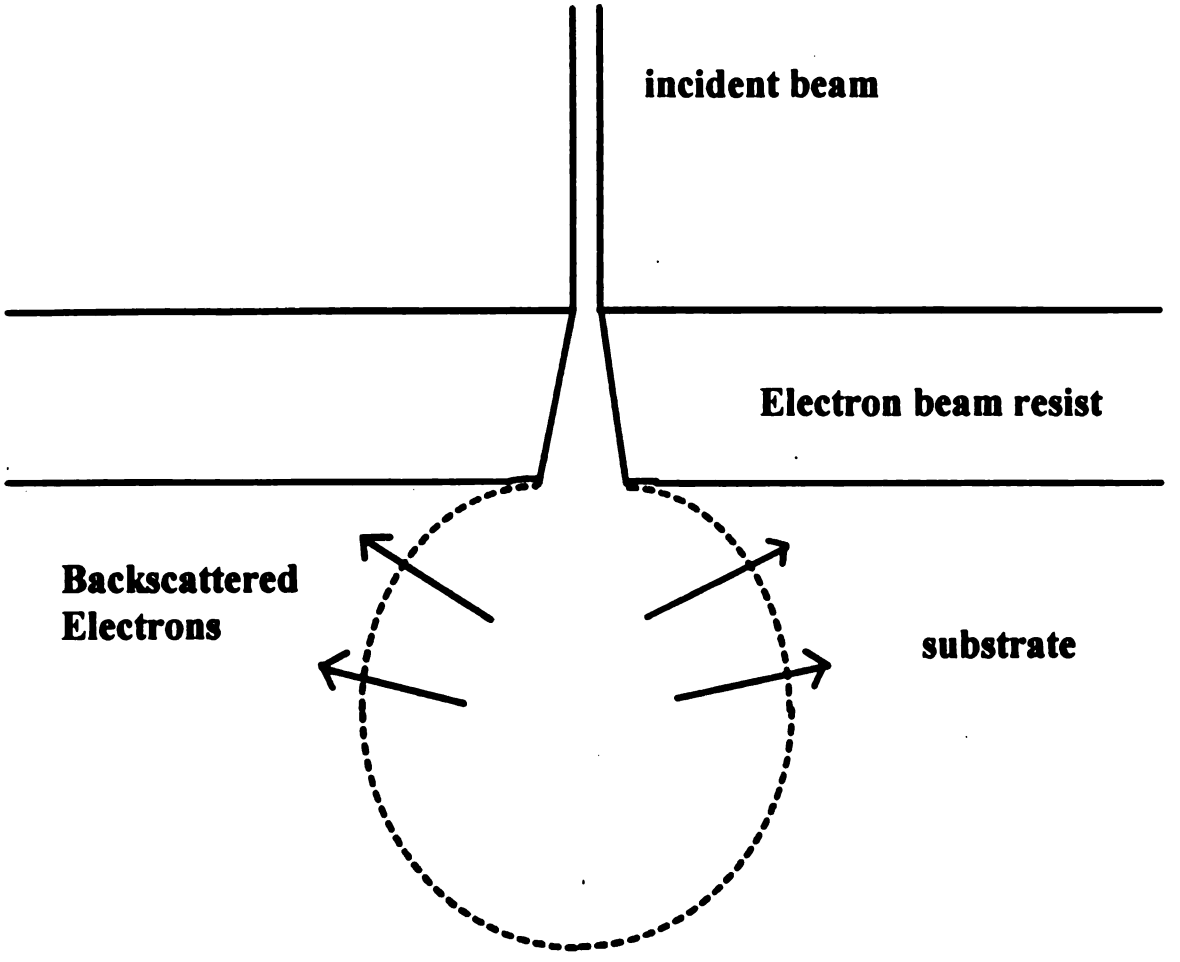

Figure 3.5 Schematic diagram of the electron interaction volume. The pear-shaped interaction volume is formed by the backscattered electrons.

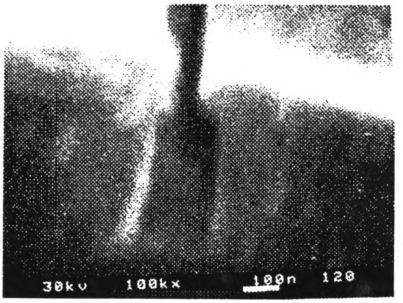

(a)

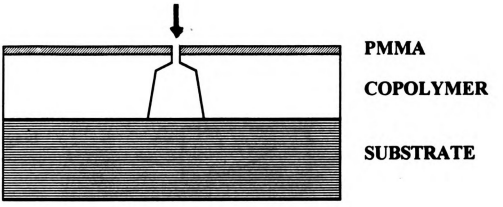

(b)

Figure 3.6 (a) SEM picture of profile of the etched area as a result of electron interaction with PMMA/MMA (electron beam resist/copolymer) bilayer. The difference of sensitivity to the electron beam between the two polymer layers makes a good undercut profile as above. (b) Schematic diagram of the interaction volume in the bilayer.

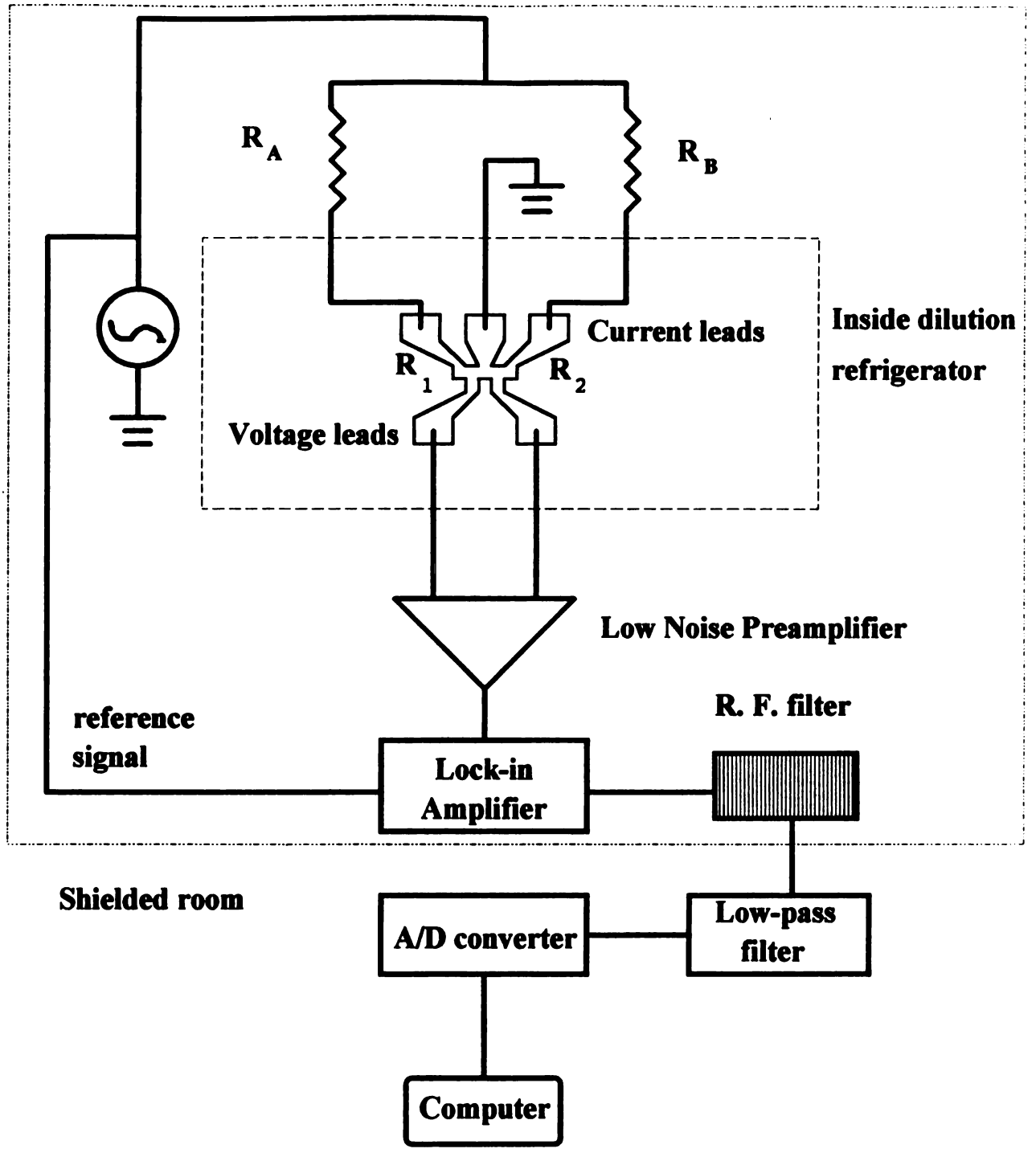

Figure 3.7 Schematic diagram of the experimental circuit. Each lead going into the dilution refrigerator passes through a filter for rejection of interference. Sample size and contact pads are not to scale.

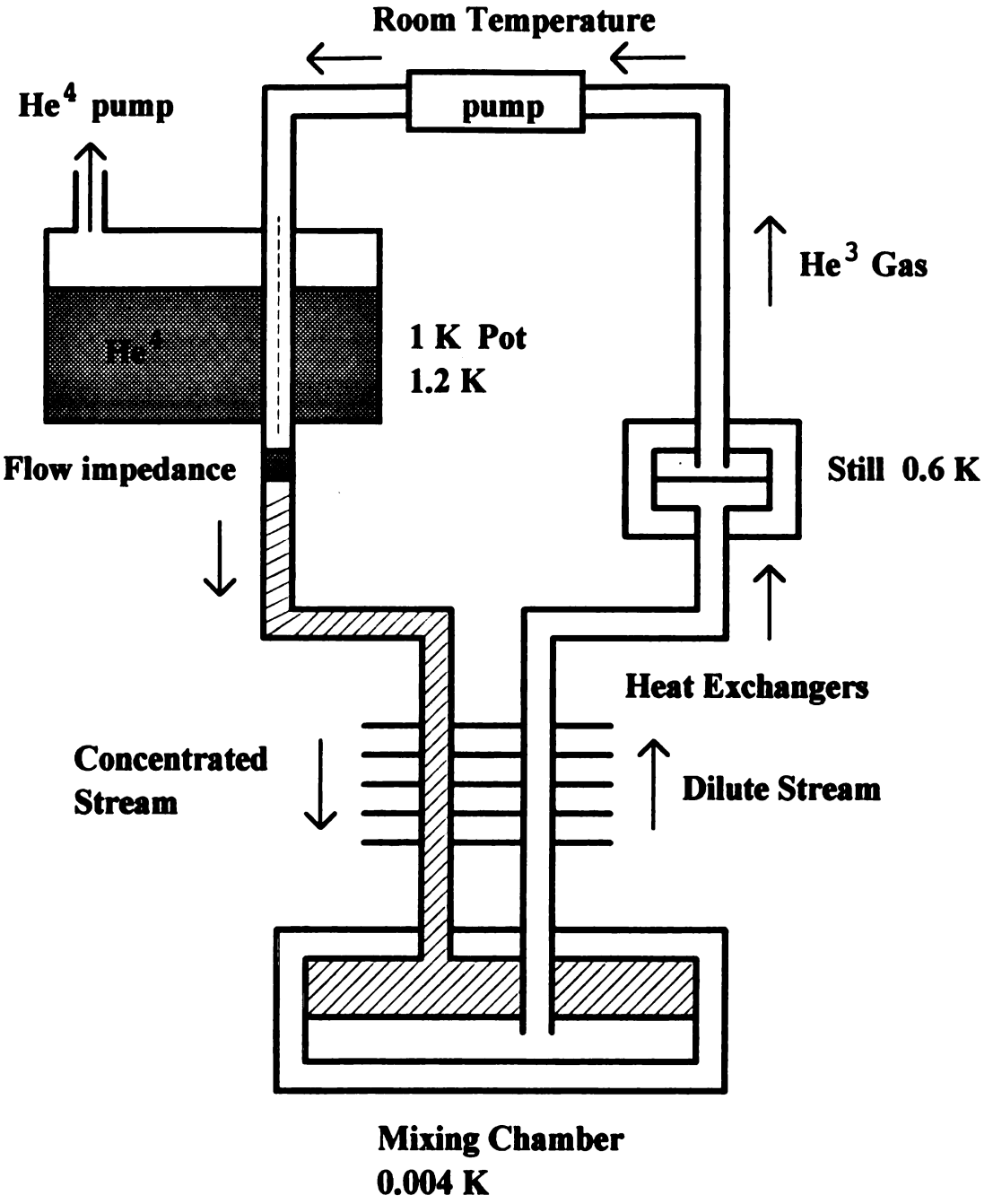

Figure 3.8 Simplified schematic diagram of dilution refrigerator

Chapter 4

Tunneling dynamics of a single defect

4.1 Time Trace of a Single Fluctuator

In our experiments, we measured the electrical conductance of several Bi wires in a five-terminal configuration. In this thesis we present data from a single defect in a single submicron wire. The resistance jumps δR across the bridge due to the motion of a single defect in either arm of the sample, were digitized as a function of time. Figure 4.1 (a) shows a typical time trace of the resistance of the sample. In this wire, the magnitude of δG is of order $0.2e^2/h$ at 1 K and $1.0e^2/h$ at 0.1 K, where e^2/h is about 4×10^{-5} mho. Furthermore, δG increased with decreasing temperature and varied in a random manner with applied magnetic field, as expected from the theory of universal conductance fluctuations.[1-3] In the experiment, the magnetic field was varied very slowly from 0 to 7 Tesla to find the magnetic field values at which the maximum conductance signal due to the motion of a single defect was achieved. By the maximum signal, we mean the signal in which the conductance has only two discrete values, with the total noise from all other sources being much smaller in size than the signal from the defect being pursued. Magnetic fields which contain mixed signals from several defects were not used for analysis. We found four different magnetic fields where the signal for a single fluctuator was clean: B = 0.140 T, 2.274 T, 2.286 T and 6.997 T. At each of these magnetic fields, we measured the transition rates of the defect as a

function of temperature. For good statistics, several hundred transitions of the defect were recorded and analyzed at each temperature.

The experimental temperature range was determined by two factors. Above about 2 K several defects were active, so it was difficult to determine unambiguously the tunneling rates of a particular defect. Below 0.1 K the signal to noise ratio was very small. Although δG increases as the temperature is lowered due to the increasing L_ϕ, the drive current must be decreased even faster to avoid sample heating (See chapter 5). We used a drive current of 0.7 nA at 0.1 K. The conductance (measured as a voltage) was sampled by the computer at a sampling frequency of either 20 or 50 Hz, depending on the fast tunneling rate γ_f of the defect. We recorded 8 to 12 files, each consisting of 16,384 voltage measurements, for each temperature.

4.2 Data analysis

Raw data of conductance as a function of time were analyzed using two independent methods. The first method consists of setting two comparator levels to measure the transitions between the states, and hence the dwell times in each state. The histogrammed dwell times are fit to a single exponential decay function to find the mean dwell times, τ in each state and the transition rates, $\gamma = \tau^{-1}$. The second method is a combination of two different fitting processes; fitting the power spectrum of the time trace to a Debye-Lorenzian lineshape to find the sum of the two transition rates, γ, and fitting the histogram of the raw conductance values to the sum of two Gaussians to obtain the ratio

of the rates. These two analysis methods yield consistent values of the transition rates in each state.

4.2.1 Transition Time Histograms and Setting Comparator Levels

The occurrence of the individual conductance jumps follows a Poisson distribution, which is appropriate for a process described by a constant rate per unit time interval. Figure 4.1 (b) shows two comparator level settings in a time trace. We set the two comparator levels between the two values of conductance corresponding to each state. The dwell times in each state are found by the following scheme; if the digitized input signal is below the lower comparator level, and then goes above the upper comparator level, it is counted as a jump from the lower state to the upper state. The dwell time in the upper state for that particular jump is the time elapsed before the signal moves down below the lower level. This algorithm is identical to a "Schmitt trigger" electronic circuit[4]. A computer program written in Quick Basic was used for the counting and recording processes. Although most of the time traces of the defect were very clean and bistable, there were some cases when the effect of a second defect was noticeable. However, since the second defect was much less active, and had smaller δG than the dominant defect, it was possible to analyze the data by breaking the time trace into several segments and setting different comparator levels in each segment. In determining the two comparator levels, we used the two peak values V_1, V_2 in the distribution of raw conductance values and standard deviation σ, given from fitting two gaussians to a histogram of the conductance values (see the next

section). We set the comparator levels as $V_1+\sigma$, $V_2-\sigma$ for $V_1<V_2$. This method of setting the comparator levels worked in most cases, but manual adjustment of the comparator levels was inevitable when the signal to noise ratio became very small, at temperatures below 0.2 K and above 1.5 K.

Since the dwell times in each state are exponentially distributed, they were histogrammed and fit to a single exponential decay function, $P(t) \propto e^{-t/\tau_i}$, to find the mean dwell time in each state, τ_f, τ_s, and the transition rates γ_f, γ_s, where $\gamma_i = \tau_i^{-1}$ (i=f or s). In the data-taking process, we set the ratio between the sample frequency and the low pass filter cut-off frequency to be f_{sample} / f_{filter} = 4 to reduce the contribution of aliased signals (See section 3.2). We kept data with frequencies $f \le f_c$ where f_c = 0.75 f_{filter}. The filter frequency was either 5 or 12.5 Hz, depending on the sample frequency. Due to the filter, transitions from one state to the other state faster than ~0.1 second were not always detected. As a result, the first bins in the histograms in each state were often less than they should have been. This could lead to errors in determining the mean transition times in each state. To avoid thess errors, we used a two parameter fitting program in which the total number of transitions and the mean transition are parameters to be determined. Figure 4.2 illustrates the fitting of histograms to a single exponential to determine the mean transition time.

4.2.2 Debye-Lorentzian Fit to Power Spectrum and Two Gaussian Fit to the Conductance Histogram

The power spectral density $S_G(f)$ for the single defect was obtained using a fast Fourier transform (or FFT) of the raw data of conductance. The fast Fourier transform is a fast computing algorithm which converts the time series of the experimental measurements to the frequency domain. The power spectrum is determined as follows: the FFT converts each time series to a series of complex Fourier coefficients in the frequency domain. The Fourier coefficients are squared and averaged over many time series to obtain an estimate of the power spectrum $S_G(f_i)$ in a narrow frequency range centered at f_i. Each data file has 16,384 voltage measurements and was divided into two groups for FFT. The frequency range was 10^{-3} Hz$\leq f \leq$10 Hz depending on the measurement time and low-pass filter setting. At each temperature, the power spectrum after background substraction was fitted to a Debye-Lorentzian function to yield the sum of the two transition rates, $\gamma = \gamma_f + \gamma_s$. Figure 4.3 shows the fits of data to fitting function.

Since the histograms of the dwell times in each state show that the transitions are totally independent random events characterized by a single rate for each state, the distribution of raw conductance values in each state is totally independent. Assuming that the distribution of conductance values in each state follows a Gaussian distribution, the overall distribution of raw conductance values is the sum of these two independent Gaussians centered at peak values, V_1, V_2. Fitting a histogram of the raw conductance values to the sum of two Gaussian gives the area and peak values of each Gaussian and standard deviation σ. The ratio of the two areas is the ratio of the transition rates, γ_f / γ_s.

The two gaussian fit to the distribution of raw of conductance values with the two peak values V_1, V_2 and standard deviation σ are illustrated in Figure 4.4. It shows good agreement between the data and the fitting function of the sum of two Gaussians. The value of γ obtained from the fit to the power spectrum and the value of γ_f / γ_s from the two Gaussian fit, together determine both γ_f, and γ_s. The results are in good agreement with those obtained from the first analysis method.

4.3 Detailed Balance and Energy Asymmetry ε

As was described in section 2.3.3, the two transition rates are related by the energy asymmetry ε of the defect through the detailed balance, $\gamma_f / \gamma_s = e^{\varepsilon / k_B T}$. To demonstrate this, we examined the temperature dependence of the rates at fixed magentic field. Figure 4.5 shows a plot of $\ln(\gamma_f / \gamma_s)$ versus $1/T$ for the four data sets, along with linear fits through the origin. The good fits confirm the above relation. The slopes of these lines give values for ε / k_B of 402, 213, 92 and 40 mK, respectively, with a standard deviation of ±10 mK.

4.3.1 Magnetic Field Dependence of Energy Asymmetry

It is obvious from Figure 4.5 that the energy asymmetry ε is strongly modified by the application of a magnetic field. The magnetic field dependence of ε was proposed theoretically by Al'tshuler and Spivak[5] and observed experimentally by Zimmerman, Golding and Haemmerle[6]. The mechanism was explained as follows: the local electron density $n(B)$ is very sensitive to a magnetic field due to

long-range interference from the scattering centers (see section 2.2.1). Then, a charge coupling of the local electron density to the defect would yield an interaction energy $E(B) \propto n(B)$. Since the fluctuation in the local electron density due to the magnetic field is random and can have equal probability of lowering or raising the energy asymmetry, the interaction energy between the defect and the electons should be a random function of the magnetic field. Therefore, the variation of the energy asymmetry, ε, should also be random with the magnetic field. Since it will be shown later that the four data sets at different magnetic fields come from the same defect, Figure 4.5 illustrates this random variation of ε with the magnetic field. In a previous work, Zimmerman et al.[6] found that ε increased at low magnetic fields for three defects studied. In our experiment, we found that the value ε/k_B = 213 mK near zero field is greater than the values of 40 mK and 92 mK at B = 2.274 and 2.286 Tesla, and that the value ε/k_B = 402 mK at B = 6.997 Tesla is the largest. This shows that the variation of ε with the magnetic field is random. Attention should be also made to the rapid varation of ε with the magnetic field, illustrated by its change from 40 to 92 mK when the field changed from 2.274 to 2.286 Tesla.

4.3.2 Characteristic Field Considerations

The amplitude of the conductance fluctuation, $\delta G(B)$, is a random function of magnetic field, with a field scale indicating that it arises from the same mechanism that causes the aperiodic magnetofingerprint $G(B)$. The energy asymmetry, ε, on the other hand, can be strongly affected by magnetic field, with a large increase in higher field, and

smaller reproducible random features[6]. Therefore, the autocorrelation function $\langle \varepsilon(B)\, \varepsilon(0) \rangle$ does not have translational invariance over the magnetic field, unlike the autocorrelation function for the conductance fluctuations. Accordingly, it is more difficult to define a characteristic field scale in this case.

4.4 Temperature Dependence of Tunneling Rates

In this experiment, the defect tunneling rates have been measured as a function of temperature from 0.1 to 2 K. Figure 4.6 shows how the transition rates for the defect vary with temperature at B = 0.14 Tesla. With ε/k_B = 213 mK, it most clearly illustrates three distinct temperature regimes. When $k_B T < \varepsilon$, γ_f is roughly temperature independent, while γ_s decreases rapidly with decreasing temperature. This behavior is in accord with the picture of spontaneous emission and stimulated absorption described in section 2.2.3. As the temperature is raised so that $k_B T > \varepsilon$, the rates cross over to a qualitatively different regime. The ratio of the two rates still obeys detailed balance, but both rates *decrease* with increasing temperature. This behavior is an essential feature of dissipative quantum tunneling in metals. Above 1.2 K, the rates increase rapidly, due first to phonon-assisted tunneling, and eventually to thermal activation over the barrier. The phenomenon of dissipative quantum tunneling is shown more vividly in Figure 4.7. In B = 2.274 Tesla, we have the smallest energy asymmetry ε/k_B of 40 mK, which is far below the lowest temperature taken in this experiment. Therefore, at this magnetic field, the data are always in the regime $k_B T > \varepsilon$, and the rates decrease with increasing

temperature as a power law, $T^{2\alpha-1}$. At B= 2.286 Tesla, we have ε/k_B = 92 mK, which is very close to the minimum experimental temperature. Figure 4.8 also illustrates three temperature regimes, but most of the rates belong to the power law regime. The largest value of ε/k_B of 402 mK for this particular defect is obtained at B = 6.997 Tesla, shown in Figure 4.9. Due to the size of ε/k_B, more than half of the data are in the regime $k_BT < \varepsilon$ at this magnetic field.

4.4.1 The Defect - Electron Bath Coupling Constant α, and the Renormalized Tunneling Matrix Element Δ_r

In section 2.2.3, the temperature dependence of the tunneling rates γ_f, γ_s were calculated in terms of the *doubly* renormalized tunneling matrix element, Δ_r, the energy asymmetry, ε, and the coupling constant, α, between the defect and the electron bath. For the case of incoherent tunneling ($\hbar\Delta_r << k_BT$), the results for the tunneling rates are from equations (2.4) and (2.5):

$$\gamma_f = \frac{\Delta_r}{4}\left(\frac{2\pi k_BT}{\hbar\Delta_r}\right)^{2\alpha-1}\frac{e^{\varepsilon/2k_BT}}{\Gamma(2\alpha)}\left|\Gamma\left(\alpha+i\frac{\varepsilon}{2\pi k_BT}\right)\right|^2 \qquad (4.1)$$

and

$$\gamma_s = \gamma_f e^{-\varepsilon/k_BT} \qquad (4.2)$$

For a defect tunneling in a metal, the coupling constant, α, is constrained to lie between 0 and 1/2. Since the theory of dissipative quantum tunneling describes the tunneling of the particle in the

presence of the conduction electrons, we limit quantative analysis to the temperature range below 1.2 K, i.e . below the onset of phonon-assisted tunneling. With the energy asymmetry, ε, given by the slope of the detailed balance plot, the data were fit to the equations for γ_f, γ_s with two parameter least-squares fits to obtain the values for the coupling constant, α and the renormalized tunneling matrix element, Δ_r. The agreement between theory and experiment is excellent for all temperatures below 1.2 K. The theoretical fits to the data at each magnetic field are illustrated in Figure 4.10 and 4.11. The values of α and Δ_r determined from the fits are given in Table 4.1. For fitting the equations to the data, a program written in FORTRAN with the subroutine called MINUIT in the VAX 4000 was used, incorporated with the CERN library to calculate the complex gamma function. The parameters are completely consistent with the dissipative tunneling model for incoherent tunneling, i.e., $\hbar\Delta_r << \varepsilon, \alpha k_B T$ and $0 < \alpha < 1/2$.[7-9]

Given excellent quantitative agreement between theory and experiment at each value of the magnetic field, the coupling constant α appears to vary with the magnetic field. Since the random variation of ε with the magnetic field is believed to be due to random fluctuations in the local charge density near the defect, and since α also depends on this charge density, it is plausible that α also varies with the magnetic field. Golding et al.[10] argued, however, that the change in α due to the magnetic field is small because α depends on electron-hole excitations with energies up to the Fermi energy whereas the magnetic field affects low-energy processes only. Our attempt to make this argument clear experimentally leads to some difficulty. The statistical uncertainties in α and $\log \Delta_r$ are only about 0.02 and 0.08,

respectively, estimated from contour plots of χ^2[11]. Since α varies over the range 0.14 - 0.22 for the four data sets presented here, a statistical analysis suggests that α does vary with magnetic field. We present an alternative analysis below, based on a scaling fit of the data, that suggests that α does not vary with magnetic field.

The parameters α and Δ_r are highly correlated through the relation between Δ_r and bare (unrenormalized) tunneling matrix element Δ_0. From equation (2.1), we have

$$\Delta = \Delta_0(\omega_c / \omega_0)^{\alpha}$$

where ω_0 and ω_c are the characteristic vibration frequency of the defect in one of its two wells and the upper cut-off frequency of the electron-hole excitations, respectively. Δ is the tunneling matrix element renormalized by the adiabatic approximation for electron-hole excitations. From equation (2.2), we have

$$\Delta_r = \Delta\,(\Delta / \omega_c)^{\alpha/(1-\alpha)}$$

for the tunneling matrix element renormalized again due to the lower bound for non-adiabatic electrons. Inserting equation (2.1) into equation (2.2) yields the relation between Δ_r and Δ_0:

$$\Delta_r = \Delta_0\,(\Delta_0 / \omega_0)^{\alpha/(1-\alpha)} \qquad (4.3)$$

where the cut-off frequency, ω_c, has dropped out. The values of α and Δ_r determined from the four fits are plotted as $\log(\Delta_r)$ versus $\alpha/1-\alpha$

in parameter space (Figure 4.12). It is found that they fall on a straight line . This correlation is highly suggestive. Taking the logarithm of equation (4.3), we have

$$\log(\Delta_r) = \log(\Delta_0) + \log(\Delta_0/\omega_0)\cdot(\alpha/1-\alpha) \qquad (4.4)$$

Assuming that α varies with magnetic field, but Δ_0 and ω_0 do not, equation (4.4) implies a linear dependence of $\log(\Delta_r)$ on $\alpha/1-\alpha$, with an intercept and slope equal to $\log(\Delta_0)$ and $\log(\Delta_0/\omega_0)$. With this interpretation and from the plot of our values α and Δ_r, we obtain the results $\hbar\Delta_0/k_B$ = 1.8×10^{-6} K and $\hbar\omega_0/k_B$ = 0.23 K. While the first of these values is reasonable, the second is not. Not only is 0.23 K extremely low for a vibrational frequency (even for a defect that tunnels at low temperature), but also such a low value violates the condition $k_BT << \hbar\omega_0$ upon which equation (4.1) is based.

A more likely reason for the observed correlation between α and Δ_r can be explained in terms of χ^2 considerations.[11] In the parameter space discussed above, the least-squares fits for each value of the magnetic field determine a line of minimum χ^2. Even the slightest change of α and Δ_r off this line in the parameter space leads to huge increase in χ^2. However, as long as the change of α and Δ_r is along the line, the fits vary only slightly within the experimental temperature range. This line of slowly varying χ^2 turns out to lie along the same line connecting the four points in Figure 4.12. This "coincidence" suggests that perhaps all four data sets can be fit with a unique set of parameters α and Δ_r.

4.4.2 Scaling Function

To test whether the data are consistent with single values of α and Δ_r, we plot all the data in the form $\gamma T^{1-2\alpha}$. From equation (2.4), we have

$$\gamma = \frac{\Delta_r}{2}\left(\frac{2\pi k_B T}{\hbar \Delta_r}\right)^{2\alpha-1} \frac{\cosh\left(\frac{\varepsilon}{2k_B T}\right)}{\Gamma(2\alpha)} \left|\Gamma\left(\alpha + i\frac{\varepsilon}{2\pi k_B T}\right)\right|^2$$

and

$$\gamma T^{1-2\alpha} = \frac{\Delta_r}{2}\left(\frac{2\pi k_B}{\hbar \Delta_r}\right)^{2\alpha-1} \frac{\cosh(1/2x)}{\Gamma(2\alpha)} \left|\Gamma\left(\alpha + i\frac{1}{2\pi x}\right)\right|^2 \qquad (4.5)$$

where $x = k_B T/\varepsilon$ is defined as a scaling variable. Since $\gamma T^{1-2\alpha}$ depends on temperature only through the ratio $k_B T/\varepsilon$, we can write $\gamma T^{1-2\alpha} = f(x)$, where $f(x)$ is a scaling function. In Figure 4.13, we plot $\gamma (T/T_0)^{1-2\alpha}$ versus $k_B T/\varepsilon$, where T_0 = 1 K for α = 0.195. The remarkable consistency between all these data sets suggests that α and Δ_r are independent of magnetic field for this defect. The solid line in Figure 4.13 is a simultaneous least-squares fit to all four data sets, yielding the values $\alpha = 0.195$ and $\Delta_r = 1.34 \times 10^4\ s^{-1}$. Figures 4.14 and 4.15 show the theoretical fits to the data of tunneling rates versus temperature, both with the values of α and Δ_r obtained at each magnetic field and with the single values of α and Δ_r given from the scaling plot. The fits for the case of single values of α and Δ_r to the data are nearly as good as the other case.

The results show that the theoretical fits depend only weakly on α over the experimental temperature range. To determine the dependence of α with magnetic field more accurately, we would need either a larger experimental temperature range, or smaller experimental uncertainties. We have attemped to minimize obvious sources of systematic error. We were very careful to limit Joule heating of the sample from the measurement current. (The tunneling rates provide an excellent measure of the defect temperature, through the detailed-balance relation.) The effect of external interference was minimized by rf filters on all electrical leads to the sample.[12] It is possible that other defects in the sample may influence the dynamics of the defect we are studying.[13] Even small changes in the measured tunneling rates can lead to significant uncertainty in the evaluation of α, especially when $k_B T \leq \varepsilon$. In the future, we will pursue further measurements in the temperature regime $k_B T > \varepsilon$, where we can most accurately determine α.

References

1. P. A. Lee and A. D. Stone, Phys. Rev. Lett. **55**, 1622 (1985).
2. B. L. Al'tshuler, and B. I. Shklovskii, Zh. Eksp. Teor. Fiz. **91**, 220 (1986). [Sov. Phys. JETP **64**, 127 (1986)]
3. P. A. Lee, A. D. Stone, and H. Fukuyama, Phys. Rev. **B 35**, 1039 (1987).
4. "The Art of Electronics", P. Horowitz and W. Hill, Cambridge University Press, New York, 1980.
5. B. L. Al'tshuler and B. Z. Spivak, Pis'ma Zh. Eksp. Teor. Fiz. **49**, 671 (1989). [JEPT Lett. **49**, 772 (1989)]
6. N. M. Zimmerman, B. Golding and W. H. Haemmerle, Phys. Rev. Lett. **67**, 1322 (1991).
7. H. Grabert and U. Weiss, Phys. Rev. Lett. **54**, 1605 (1985).
8. M. P. A. Fisher and A. T. Dorsey, Phys. Rev. Lett. **54**, 1609 (1985).
9. A. J. Leggett et al., Rev. Mod. Phys. **59**, 1 (1987) and refs. therein.
10. B. Golding, N. M. Zimmerman and S. N. Coppersmith, Phys. Rev. Lett. **68**, 998 (1992).
11. See "Numerical Recipes in Fortran", W. H. Press, B. P. Flannery, S. A. Teukolsky, and W. T. Vetterling, Cambridge University Express, New York, 1988.
12. The success of the rf filtering was confirmed by the reproducible behavior of one defect over a two-month period.
13. There is a strong evidence for defect-defect interactions at much higher temperatures; see K. Ralls and R. A. Buhrman, Phys. Rev. Lett. **60**, 2434 (1988).

Table 4.1 Physical parameters of four data sets.

B(T)	ε (mK)	α	Δ_r (s^{-1})	log Δ_r
0.140	213	0.16	2.5×10^4	4.40
2.274	40	0.21	1.0×10^4	4.01
2.286	92	0.14	3.4×10^4	4.53
6.997	402	0.22	8.3×10^3	3.92

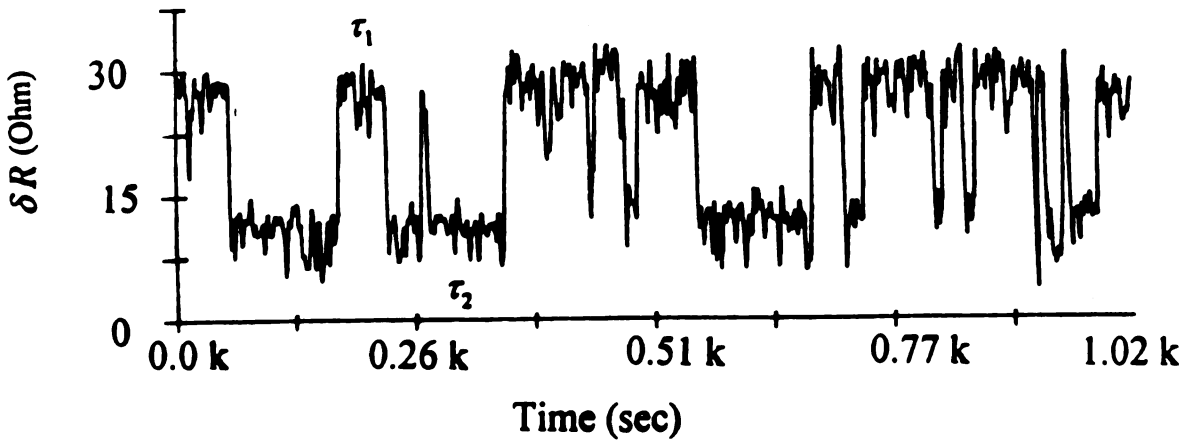

(a)

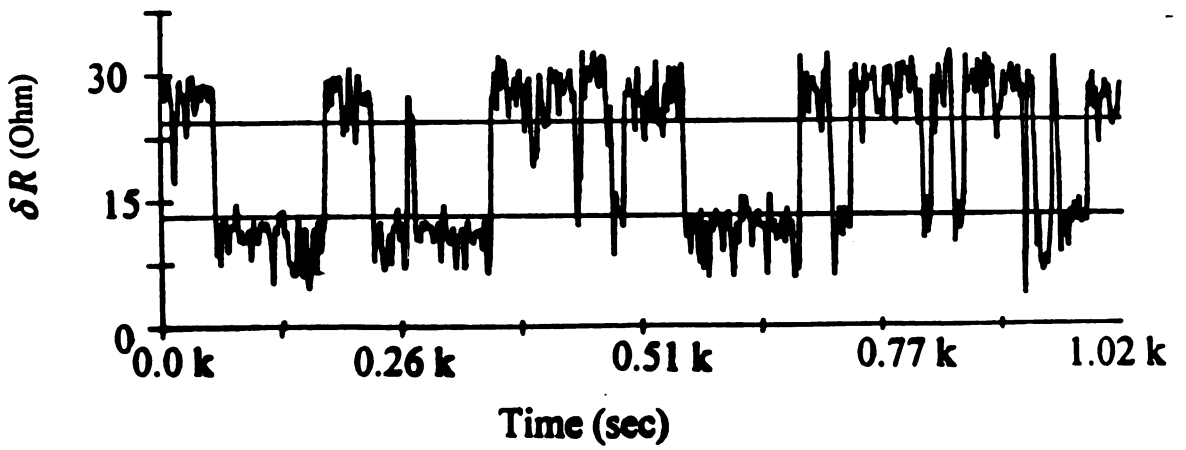

(b)

Figure 4.1 (a) Resistance change δR as a function of time, at $B = 6.997$ T and $T = 0.22$ K. The resistance switches between two values, corresponding to the tunneling of a single defect between two states. The resistance of each arm of the sample is about 1 KΩ and δR in this case is about 20 Ω. (b) Comparator levels are set between the two values of the resistance to measure both the number of the transitions and the dwell times in each state.

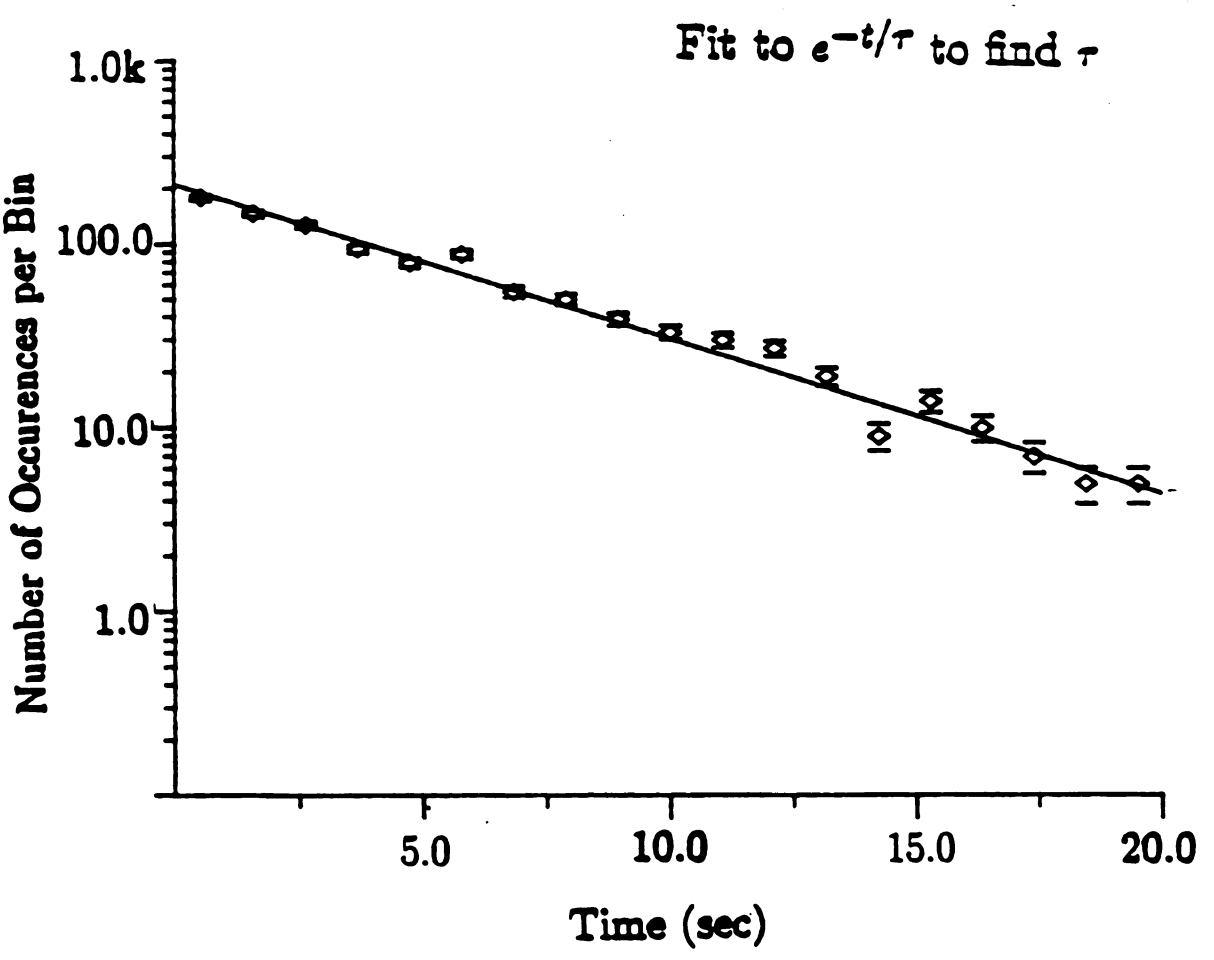

Figure 4.2 The dwell times in each state are histogrammed and fit to a single exponential decay function to find the mean transition time, τ, and the transition rate to the other state, $\gamma = \tau^{-1}$.

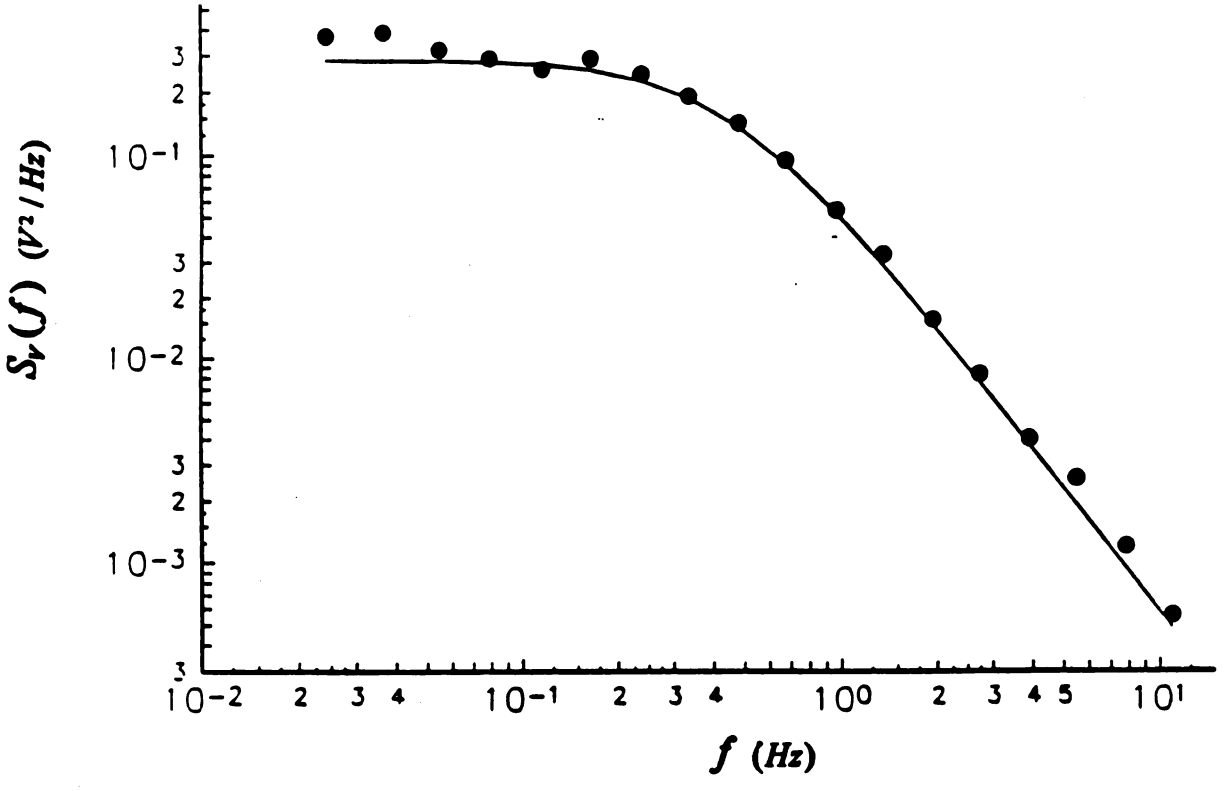

Figure 4.3 The power spectrum of the time trace data. The spectrum is fit with a Debye-Lorentzian function which represents the spectrum of a single two-level system with a characteristic time τ. The amplitude of the resistance jump and the sum of the transition rates are obtained from the fit of the data to the Debye-Lorentzian.

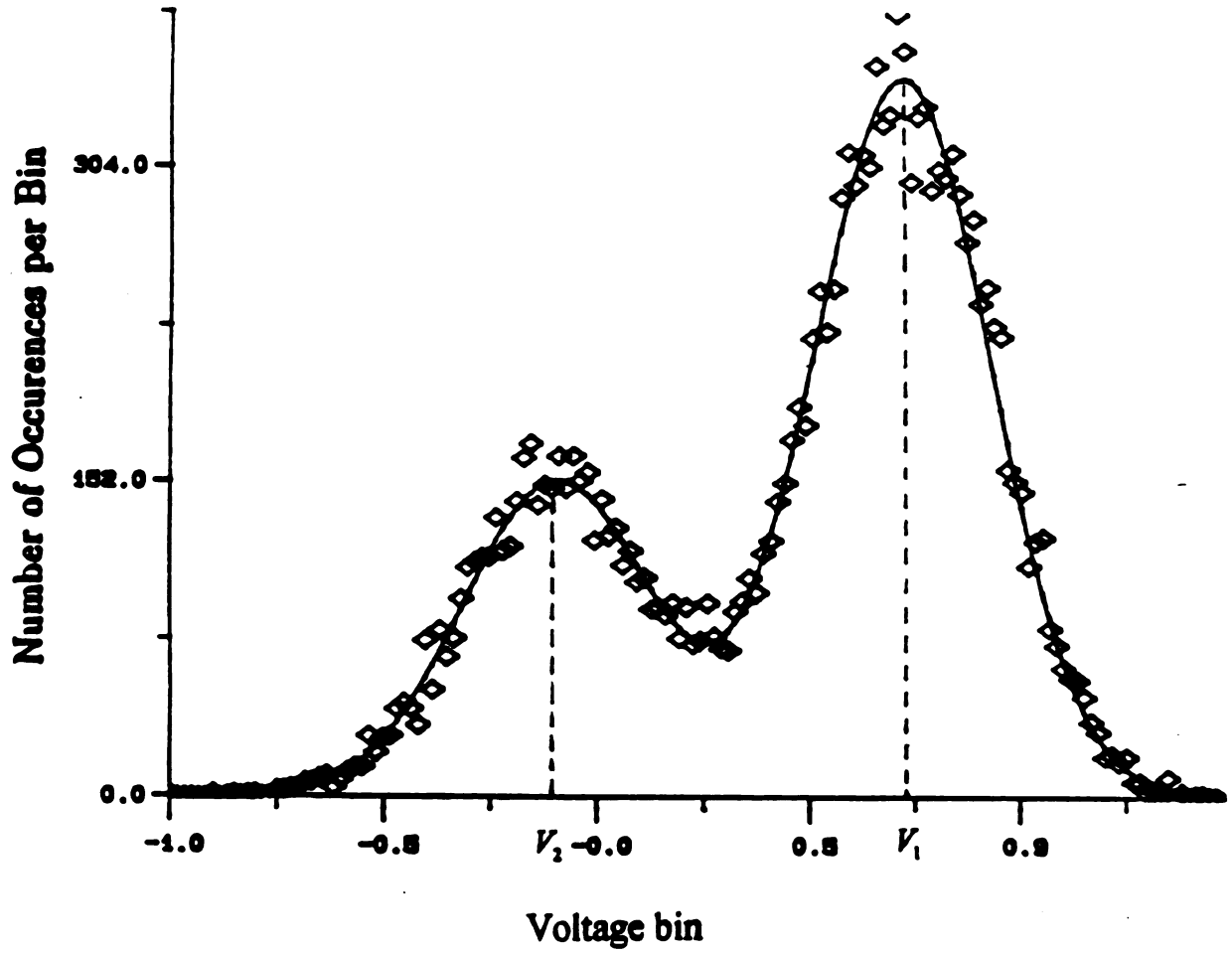

Figure 4.4 Histogram of raw values of resistance. The solid line is a fit to the sum of two Gaussians. The ratio of the areas of the two Gaussian distributions gives the ratio of the two transition rates. Also from the peak values V_1, V_2 and the standard deviation σ, the positions of the two comparator levels were determined.

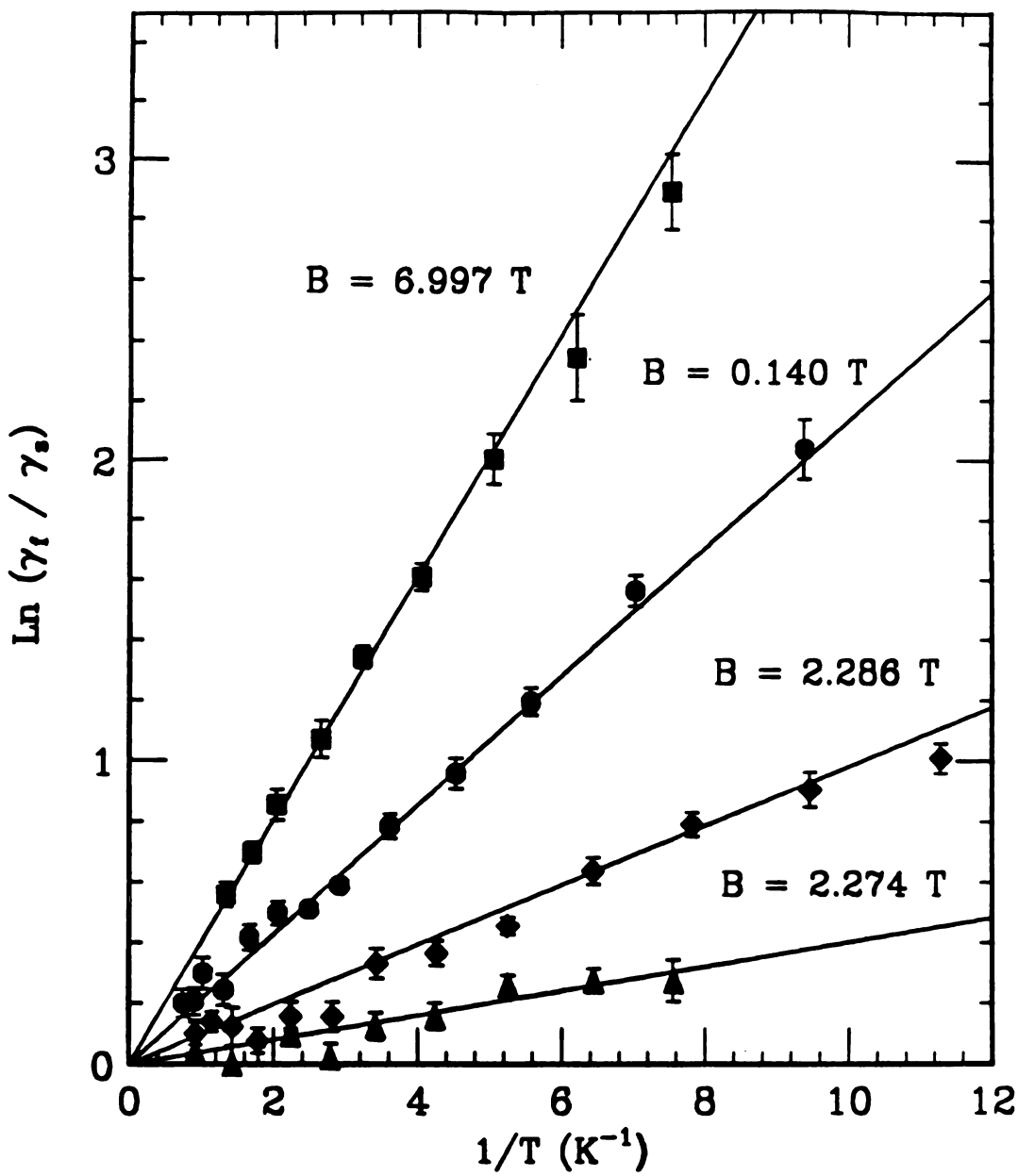

Figure 4.5 *Ln* (γ_f / γ_s) versus $1/T$, for four values of the applied magnetic field. The slopes of the lines are 402, 213, 92 and 40 mK, respectively, with an uncertainty of ±10 mK.

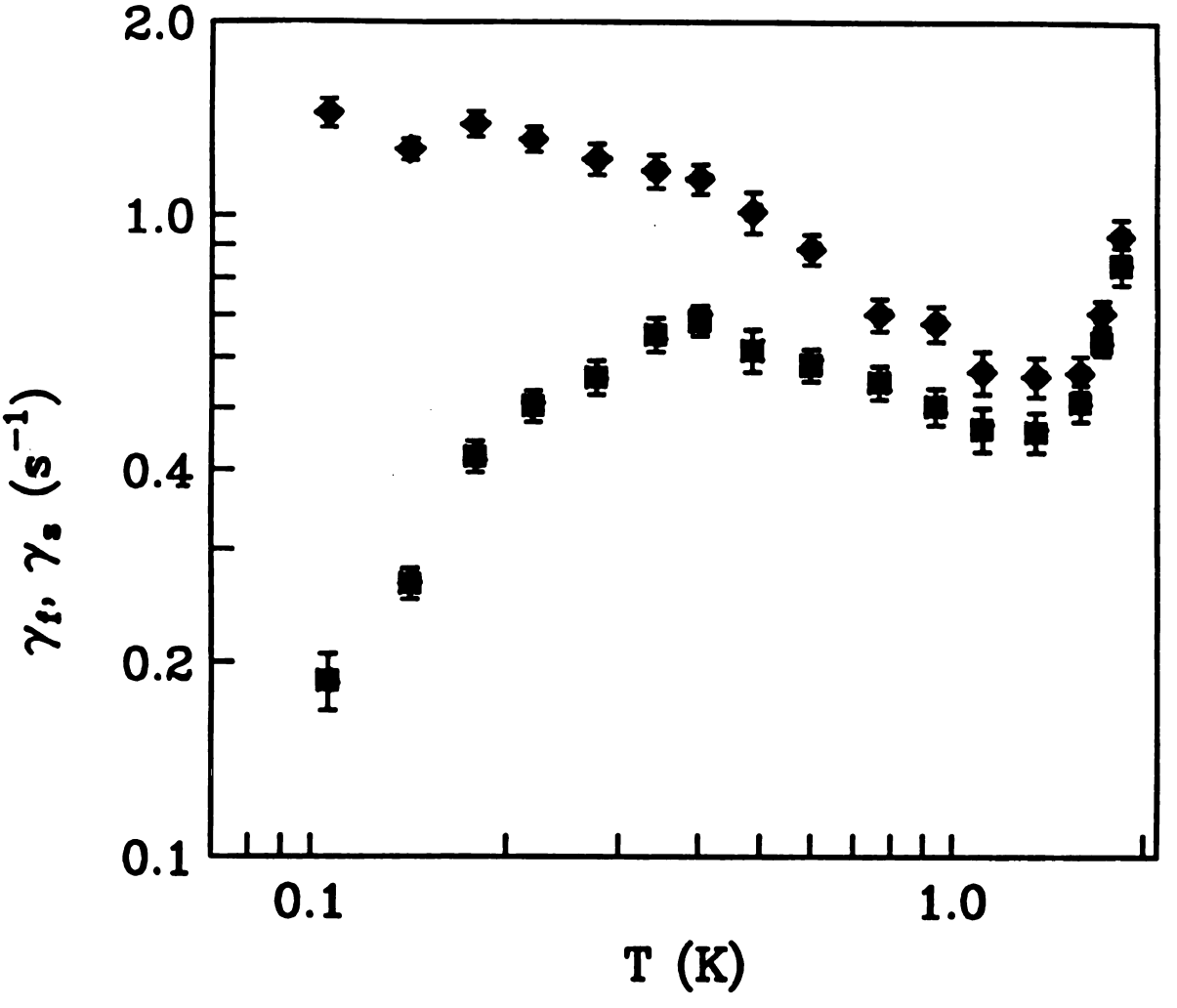

Figure 4.6 Fast and slow transition rates versus temperature at B = 0.140 T. The value of ε / k_B (from Figure 4.5) is 213 mK. The data clearly show three distinct temperature regimes, $T < \varepsilon / k_B$, $T > \varepsilon / k_B$ and $T > 1.2$ K.

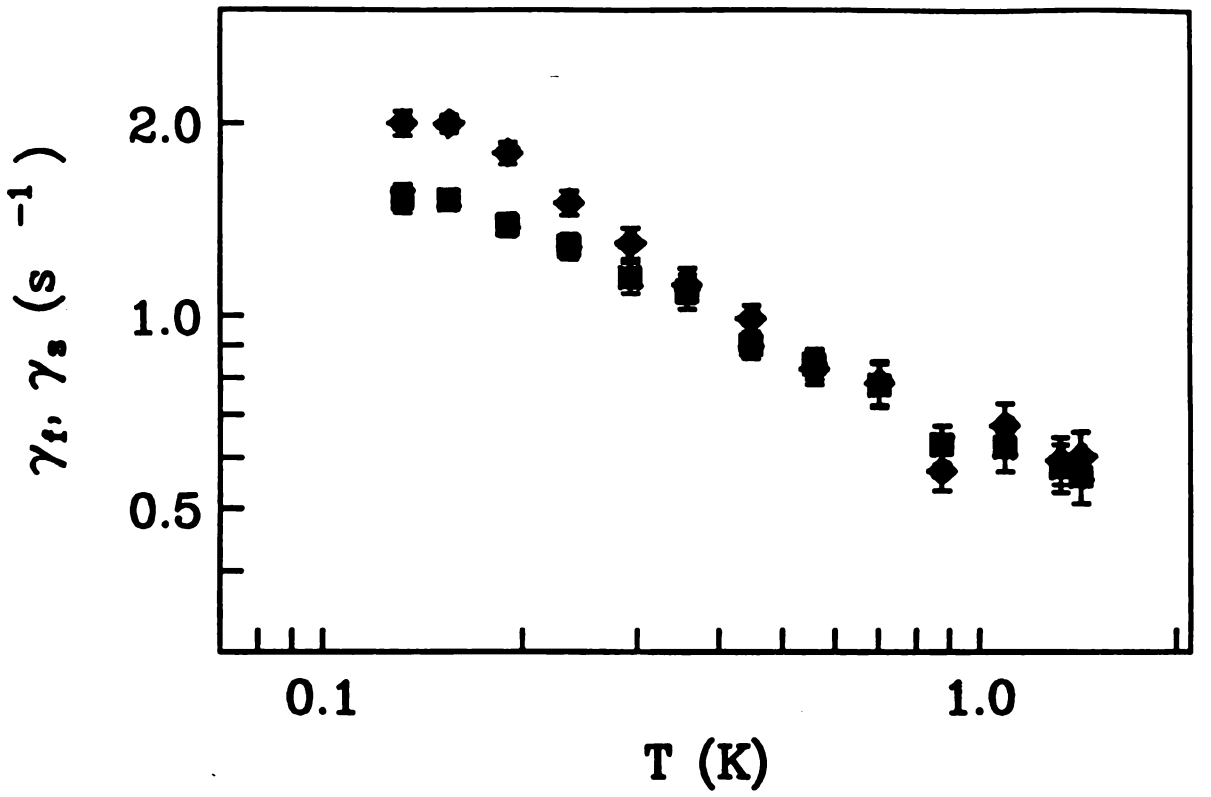

Figure 4.7 Fast and slow rates versus temperature at B = 2.274 T. The value of ε / k_B is 40 mK. The data show the regime $T > \varepsilon / k_B$ only.

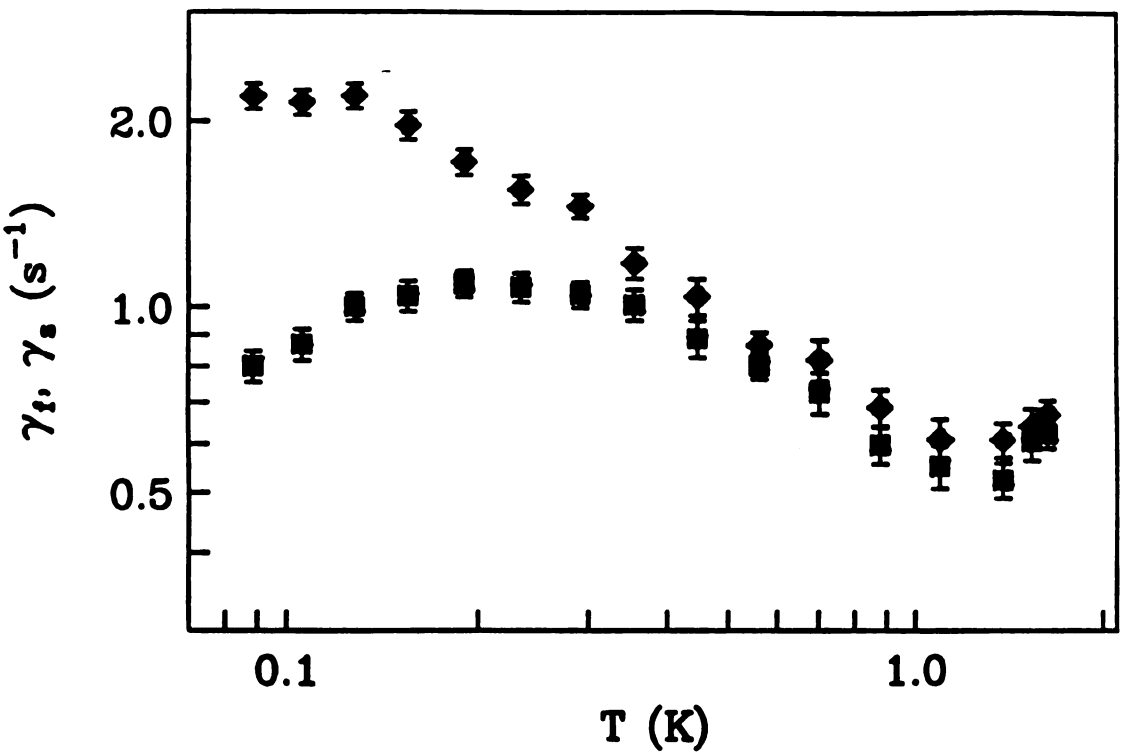

Figure 4.8 Fast and slow rates versus temperature at B = 2.286 T. The value of ε / k_B is 92 mK. The data show three temperature regimes, but most of the data are in the regime $T > \varepsilon / k_B$.

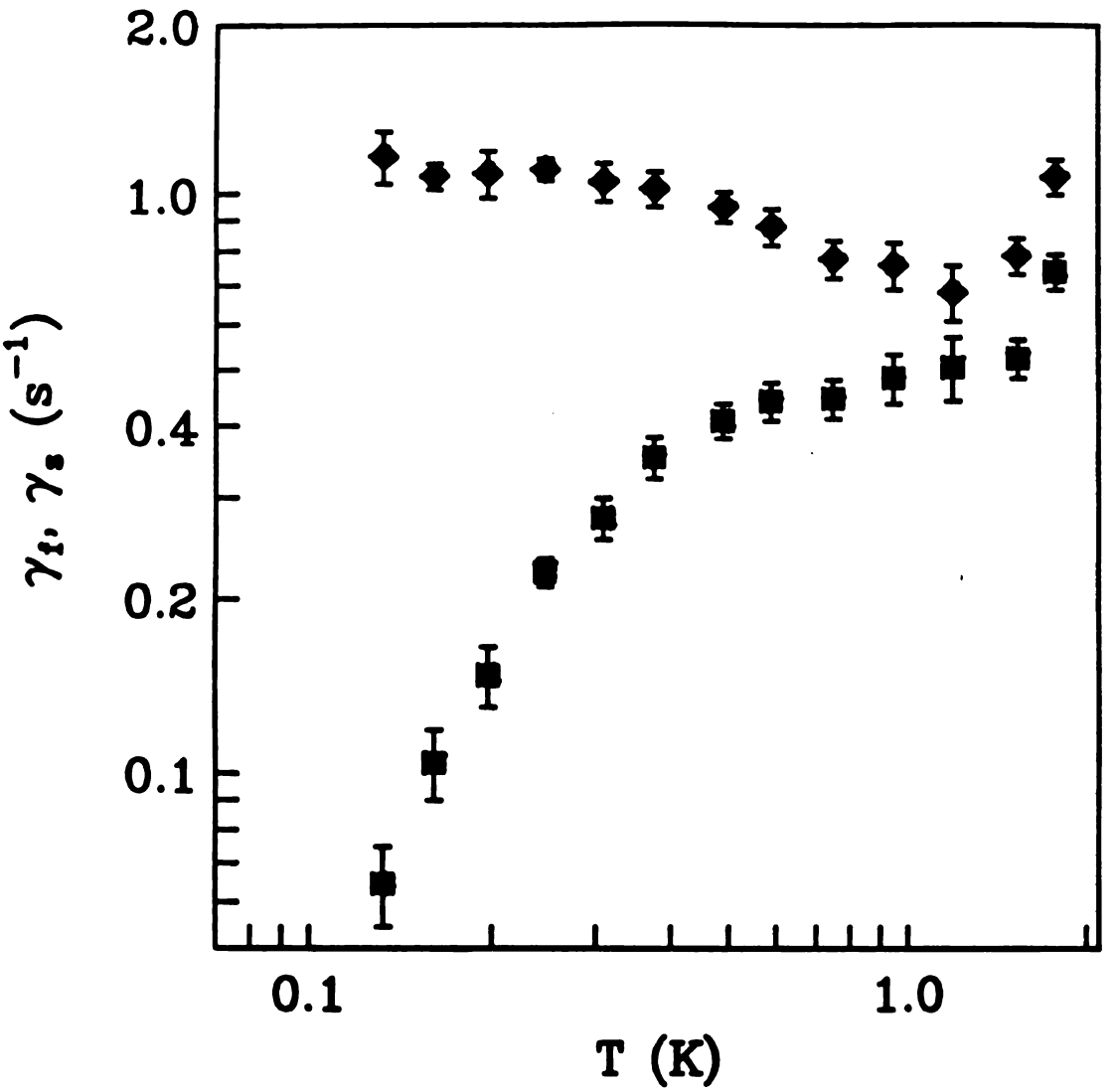

Figure 4.9 Fast and slow rates versus temperature at B = 6.997 T. The value of ε / k_B is 402 mK. About half of the data are in the regime $T < \varepsilon / k_B$.

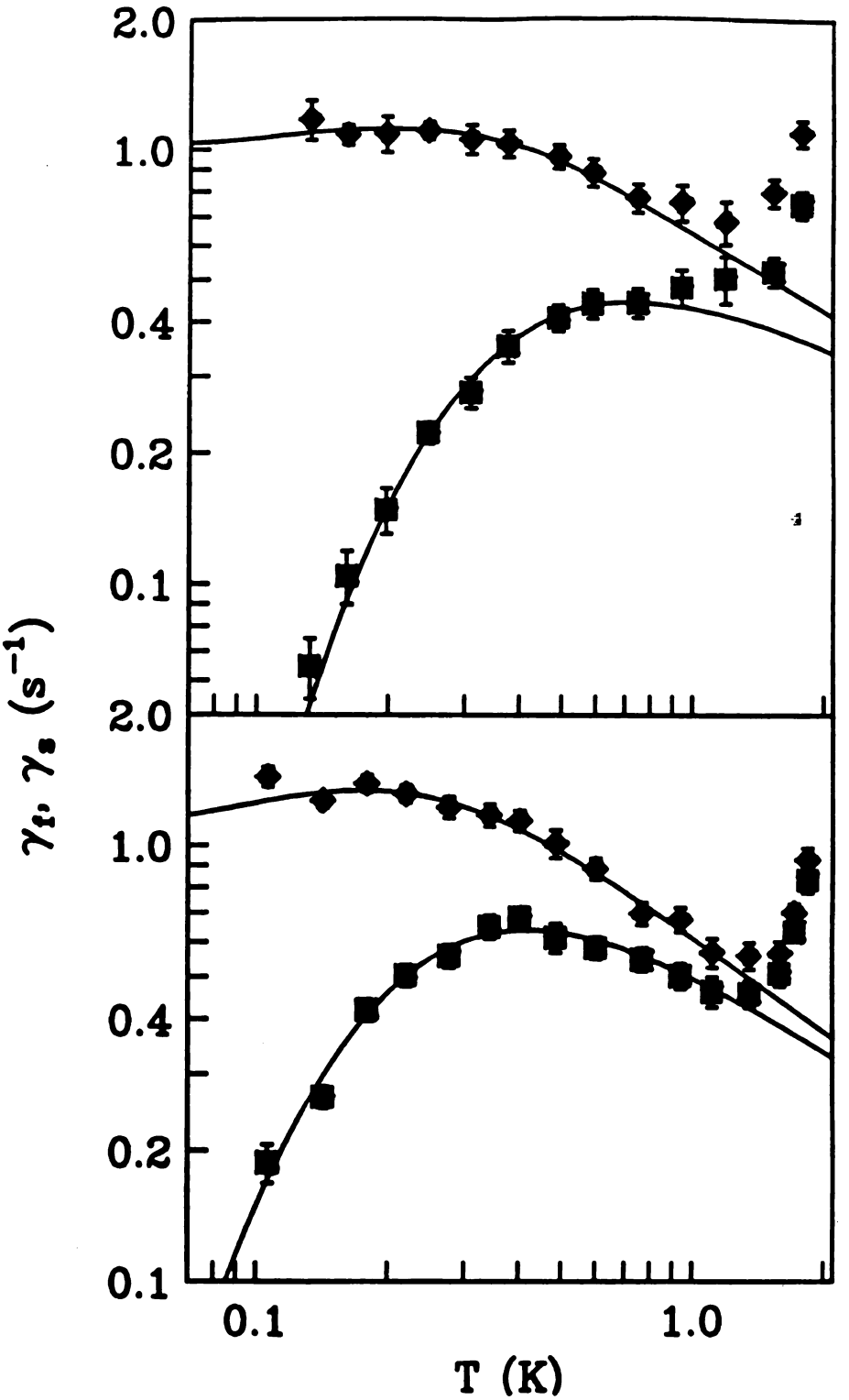

Figure 4.10 Fast and slow transition rates versus temperature at B = 6.997 T and 0.140 T. Solid lines are fits of Equations 4.1 and 4.2 to the data for $T < 1.2$ K. The values of ε / k_B are 402 and 213 mK, from top to bottom. The values of α obtained from the fits are 0.22 and 0.16, respectively, with corresponding values of Δ_r of 8.3×10^3 s^{-1} and 2.5×10^4 s^{-1}. Uncertainties are discussed in the text.

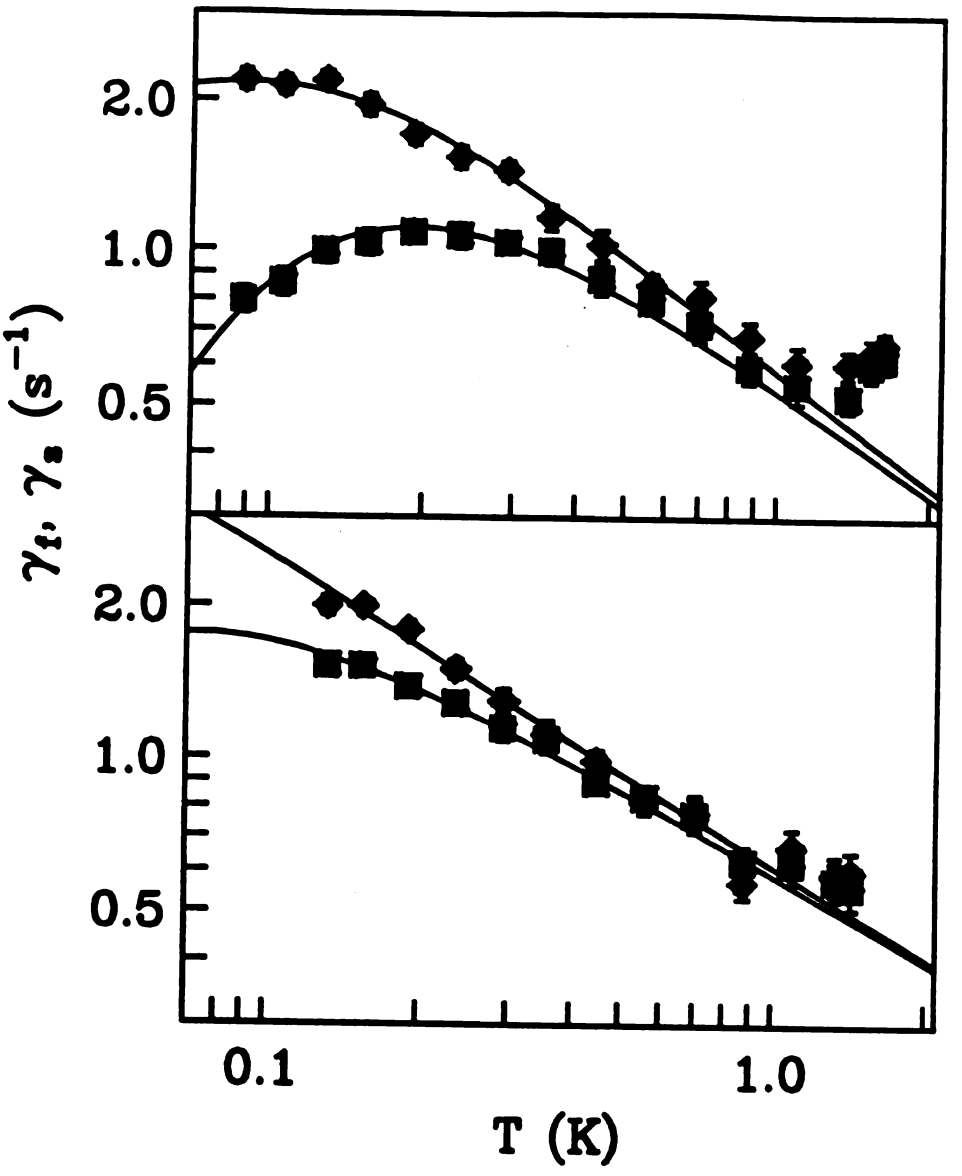

Figure 4.11 Fast and slow transition rates versus temperature at B = 2.286 T and 2.274 T. Solid lines are fits of Equations 4.1 and 4.2 to the data for $T < 1.2$ K. The values of ε / k_B are 92 and 40 mK, from top to bottom. The values of α obtained from the fits are 0.14 and 0.21, respectively, with corresponding values of Δ_r of 3.4×10^4 $s^{-1}$and 1.0×10^4 s^{-1}. Uncertainties are discussed in the text.

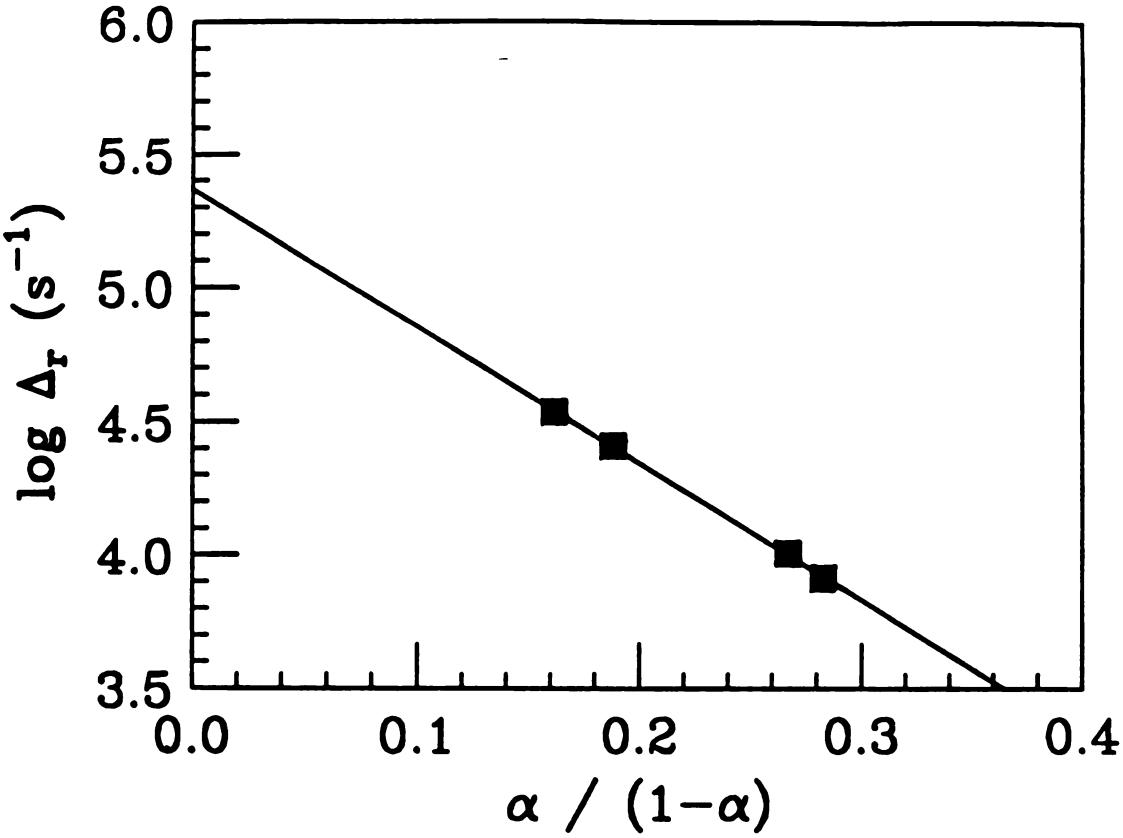

Figure 4.12 Plot of the values of α and Δ_r given from the four fits in the log(Δ_r) versus $\alpha/1-\alpha$ parameter space.

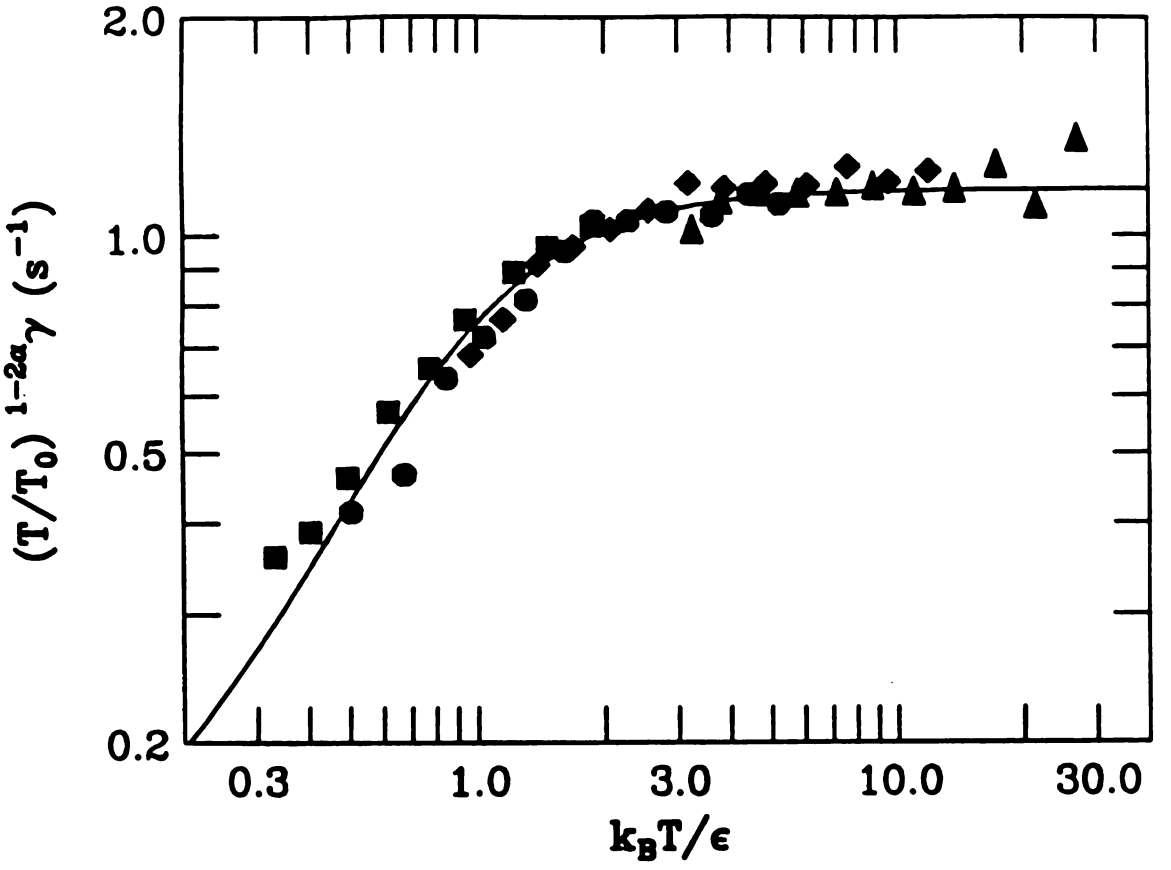

Figure 4.13 Log-log plot of $(T/T_0)^{1-2\alpha}\gamma$ versus k_BT/ε for all four data sets, with $T_0 = 1$ K and $\alpha = 0.195$. The solid line is a fit of Equation 4.5 to all the data, with $\Delta_r = 1.3 \times 10^4\ s^{-1}$. The four data sets are B = 6.997 T (■), 0.140 T (●), 2.286 T (♦), and 2.274 T(▲).

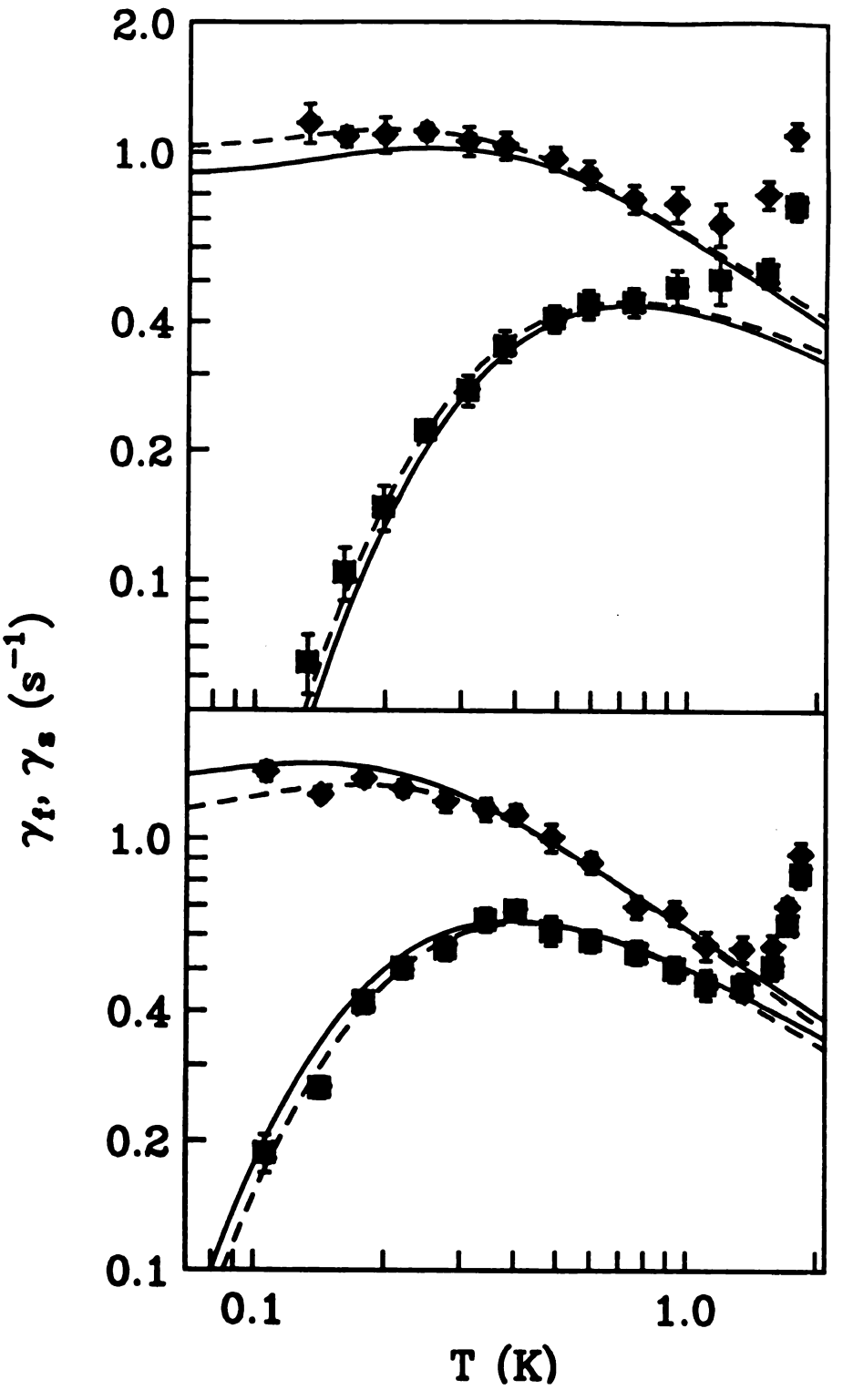

Figure 4.14 Fast and slow transition rates versus temperature at B = 6.997 T and 0.140 T. Dashed lines are fits of Equations 4.1 and 4.2 to the data for $T < 1.2$ K, with the values $\alpha = 0.22$ and 0.16 with corresponding values of Δ_r of 8.3×10^3 s^{-1} and 2.5×10^4 s^{-1}. The solid lines are fits with the global value of $\alpha = 0.195$ and $\Delta_r = 1.34 \times 10^4$ s^{-1}.

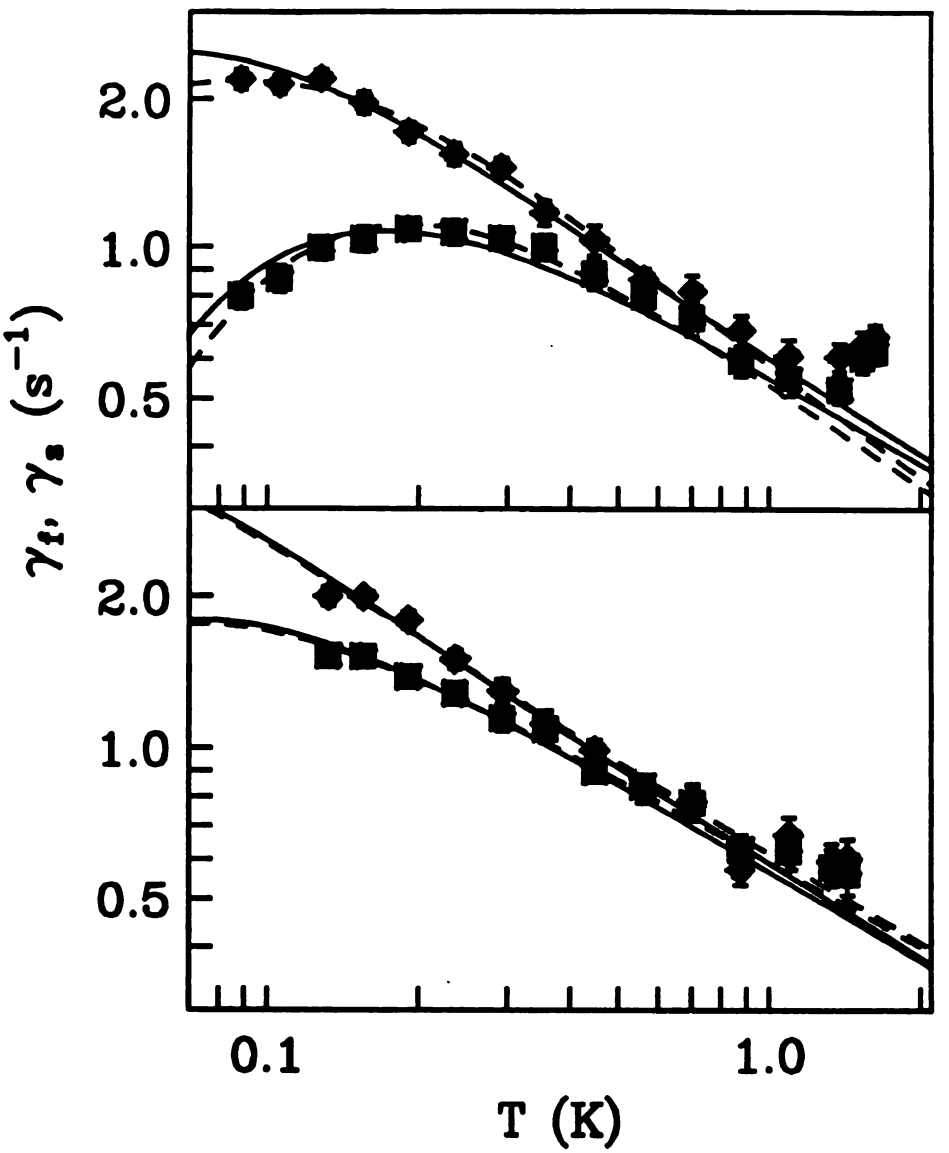

Figure 4.15 Fast and slow transition rates versus temperature at B = 2.286 T and 2.274 T. Dashed lines are fits of Equations 4.1 and 4.2 to the data for $T < 1.2$ K, with the values $\alpha = 0.14$ and 0.21 with corresponding values of Δ_r of $3.4 \times 10^4\ s^{-1}$ and $1.0 \times 10^4\ s^{-1}$. The solid lines are fits with the global value of $\alpha = 0.195$ and $\Delta_r = 1.34 \times 10^4\ s^{-1}$.

Chapter 5

Electron Heating Experiment

5.1 Defect Temperature and Electron Temperature

We have studied the effect of Joule heating on the dynamics of a single bistable defect in a submicron Bi wire below 1 K. At high temperatures, the dominant inelastic scattering mechanism is electron-phonon scattering. At low temperatures, the electron-phonon scattering decreases, and electron-electron scattering becomes the dominant source of inelastic scattering. Due to the weak electron-phonon coupling in this temperature range, the energy transfer from the electrons to the phonons is much slower than the energy absoption of the electrons from the applied current drive. The electron-electron scattering, unlike electron-phonon scattering, acts to thermalize the electrons internally, but does not contribute to the energy transfer to the lattice. The difference in energy flow between the two transport processes gives rise to electron heating to a temperature above the phonon temperature. This temperature difference reflects the rate of energy transport between the electrons and lattice. By applying the idea of electron heating to our sample and measuring the temperatures of the electrons, the defect and the lattice as a function of drive current, we investigated the energy transport between the hot electrons, the defect and the phonons. Figure 5.1 illustrates the energy transport of the system.

This experiment was motivated by the observation that defects with small duty cycles (i.e. with large ratio of the fast transition time and

slow transition time, τ_f / τ_s) are quite sensitive to the amplitude of the measurement current. The ratio of the fast and the slow transition rates of a defect depends on temperature through the detailed balance relation $\gamma_f / \gamma_s = e^{\varepsilon/k_B T}$. When $\varepsilon/k_B T > 1$, this ratio is sensitive to small changes in the temperature seen by the defect. Since the defect is strongly coupled to the conduction electrons in the sample below 1 K, we interpret its sensitivity to drive current as an indication of electron heating and the ratio of the two rates as a local thermometer. The defect temperature is defined from the detailed balance relation as

$$T_{\text{defect}} = \frac{\varepsilon / k_B}{\ln(\gamma_f / \gamma_s)}$$

Using the "defect thermometer" to study heating is attractive because it is based purely on statistical mechanics - a feature it shares with the Johnson noise thermometer used by Roukes et al.[1] in a previous electron heating study. An electron heating study based only on the defect thermometer relies on the assumption that the defect is more strongly coupled to electrons than to phonons. We will show that this assumption breaks down for temperatures above about 1 K, based on fits of our data to dissipative quantum tunneling theory.[2-3] The data presented here were taken well below 1 K, where we expect the assumption to hold. We would have liked to measure the electron temperature directly, and thereby deduce the relative thermal coupling between the defect and the electrons and phonons as a function of temperature. We did not achieve this more ambitious goal, for two reasons. We tried to measure the electron temperature from the amplitude of the resistance

fluctuations induced by the moving defect, but this thermometer did not obey a simple heating model. Also, we could not extend our heating measurements above 1 K due to interference from other defects in the sample.

The sample for this study is the same Bi wire discussed in Chapter 4. Among several different values of the applied magnetic field where the resistance of the sample shows clear transitions between two states of a bistable defect, the data were taken with a magnetic field of 7 Tesla, where the energy asymmetry of the defect was largest, hence the ratio of transition rates was most sensitive to temperature. At each value of temperature and drive, several hundred transitions were recorded and analyzed. The same analysis method as described in the previous chapter was used to obtain the fast and slow transition rates, γ_f, γ_s.

Figure 5.2 shows $\ln(\gamma_f / \gamma_s)$ versus inverse temperature, taken with a low enough drive current that no significant heating of the sample occurs. The data can be fit by a straight line through the origin, with a slope equal to the energy asymmetry of the defect, ε / k_B = 0.420±0.02 K. We performed the heating experiment by increasing the amplitude of the AC drive current used to measure the resistance. We checked that using a large DC current for heating plus a small AC measurement current produced consistent results.

5.2 Power Law Dependence of Defect Temperature on Drive Current

Figure 5.3 shows the results of heating the sample with large drive current, for lattice temperatures of 0.132, 0.247, and 0.490 K. Rather than plot γ_f / γ_s, we plot the defect temperature. For low drive current, the defect temperature rises slowly above the lattice temperature. As the drive current increases, the defect temperature approaches a power law behavior that depends only on drive current, independent of the initial lattice temperature. Behavior similar to that shown in Figure 5.3 has been observed by Roukes et al.[1], who derived an expression for the electron temperature as a function of drive current based on an earlier model of Anderson, Abrahams and Ramakrishnan.[4] (The concept of an "electron temperature" far from equilibrium was justified by Arai.[5]) The model is based on the observation that the thermal conductance between electrons and phonons in a sample of volume V is $\kappa_{\text{el-ph}} = C_{\text{el}} \tau_{\text{el-ph}}^{-1}$, where $C_{\text{el}} = \gamma_{\text{el}} TV$ is the electronic heat capacity and $\tau_{\text{el-ph}}^{-1} = \alpha_0 T^p$ is the electron-phonon scattering rate. The quantity α_0 is the strength of the electron-phonon coupling. The exponent p varies between 2 and 3 for typical disordered films.[6-7] For low drive current, the temperature offset between the electrons and phonons is proportional to the power dissipated in the sample, $\dot{Q} = I^2 R$. As current increases, the electron temperature rises, and the electrons become more efficient at cooling themselves by emitting phonons. Eventually the electron temperature approaches the asymptotic dependence on drive current $T_{\text{el}} \propto I^{2/(2+p)}$, independent of the initial lattice temperature T_0. The rate of the power given to the electrons from the drive current is

$$d\dot{Q}_{in} = 2IR\,dI$$

and the rate of energy loss to phonons is

$$d\dot{Q}_{out} = \kappa_{el\text{-}ph}(T)dT = \alpha_0\gamma_{el}VT^{1+p}dT$$

where T is the electron temperature. Energy balance requires $d\dot{Q}_{in} = d\dot{Q}_{out}$ in the steady state. Integration of the relation from T_0 to T_{el} yields the expression:

$$T_{el}^{2+p} - T_0^{2+p} = \frac{(2+p)}{\alpha_0\gamma_{el}} \cdot \frac{I^2R}{V} \qquad (5.1)$$

The solid lines in Figure 5.3 represent a single global fit of equation (5.1) to all the data shown in the figure, with two free parameters p and $\alpha_0\gamma_{el}$. The values of the parameters obtained from the fit are $p = 2.0 \pm 0.2$, and $\alpha_0\gamma_{el} = (4.5 \pm 1.0) \times 10^{10}$ W/K^{4}m^3 .

Before interpreting these results, we examine the assumptions made regarding heat transfer in the sample. First we consider the thermal coupling of the defect to the electrons and phonons. Figure 5.4 shows a log-log plot of the fast and slow transition rates of the defect versus temperature. The behavior of these rates below 1 K is described by dissipative quantum tunneling theory,[2] and was the subject of Chapter 4. In our experiment, the temperature and energy asymmetry are much smaller than the vibrational level spacing in a single-well, and much larger than the renormalized tunneling matrix element. In this regime,

the only property of the heat bath that enters into the theory is the low-energy spectral density of excitations, $J(\omega) = \omega^n$, where n = 1 or 3 for electrons or phonons, respectively. We showed in chapter 4 that for $T < 1.2\ \mathrm{K}$ the data could be fit with a model that considered only electrons in the heat bath. To fit the data above 1.2 K, one must include the phonon contribution. The solid line in Figure 5.4 is a fit of the data to a function calculated by Grabert[3] that includes the effect of both electrons and phonons. The agreement between the function and the data is quite good. However, this does not mean that the fit shown in Figure 5.4 confirms the formula of Grabert. We clearly need more high temperature data points to confirm it. We are interested in the value of Grabert's parameter T_{ph}, the crossover temperature between electron-dominated and phonon-dominated behavior. For the data shown in the figure, $T_{ph} = 0.95 \pm 0.03$ K. A fit to data from the same defect measured at a different value of the magnetic field (0.14 T) yields $T_{ph} = 0.91 \pm 0.03$ K. Since the lattice temperatures in our heating study are well below T_{ph}, we are justified in neglecting the thermal coupling between defect and phonons.[3]

Another crucial assumption in the analysis leading to equation (5.1) is that the electrons heat while the phonons remain at the temperature of the cryostat. This assumption, already described in section 5.1, is valid if the thermal link between the electrons and phonons is much weaker than that between the phonons and substrate and between the substrate and the cryostat.[8] The latter condition is easily fulfilled. The Si substrate has a surface area 10^8 times larger than the sample area, and is immersed in liquid helium in close proximity to the cryostat thermometer. We believe that the former

condition is also satisfied, by the following argument. The thermal conductance between film and substrate is about $\kappa_{sub}/T^3A \approx 500$ W/m^{2}K^4, where A is the area of the film in contact with the substrate.[9] We estimate $\kappa_{el\text{-}ph}$ in our Bi film as follows: The density of electron and hole states at the Fermi level is generally larger in thin Bi films than in bulk Bi. We take the value $\gamma_{el} = 2$ J/K^{2}m^3, which is twice the value for bulk Bi.[10] The electron-phonon scattering rate was measured by Dorozhkin et al.,[6] who obtained $\tau_{el\text{-}ph} = \alpha_0 T^p$ with p = 3 and $\alpha_0 = 3\times10^9$ s^{-1}K^{-3}. (Our own measurements suggest a smaller value of p, but we will use this as a starting point.) Since the thickness of our sample is 20 nm, we have $\kappa_{el\text{-}ph}/T^4A \approx 120$ W/K^{5}m^2. The above estimates give $\kappa_{sub}/\kappa_{el\text{-}ph} \approx 4$ at 1 K and 40 at 0.1 K.

A final assumption usually made in a heating experiment is that the electron and phonon temperatures are uniform throughout the sample. Unfortunately, this assumption is not valid in our experiment, due to the very small sample size. (This small size is necessary to enable us to detect the motion of a single defect.) In our sample, shown in Figure 2.1, heat dissipated in the sample can flow within the electronic system directly out the leads to the large pads, without first equilibrating with the phonons in the sample. We estimate the thermal conductance out the leads using the Wiedemann-Franz relation: $\kappa/\sigma T = 2.5\times10^{-8}$ WΩ/K^2, where κ, σ are thermal and electrical conductivity, respectively. The longest distance from any part of the sample to the large pads is about 0.5 μm, corresponding to about half the sample resistance, i.e. 1 kΩ. Hence the thermal conductance of the electrons from the hottest part of the sample to the cool part is about $2.5\times10^{-11}T$ W/K^2. In comparison, the thermal conductance between the

electrons and phonons *inside one arm of the sample* ($A^2 = 0.05\ \mu m^2$) is only $6 \times 10^{-12} T^4$ W/K^5 according to the estimate made above. These numbers show that the Joule heat generated within the sample diffuses out the leads at least as quickly as it transfers to the phonon system, giving rise to a temperature gradient in the sample.

This last consideration precludes us from obtaining an absolute estimate of the electron-phonon scattering rate from our data. Equation (5.1) was derived assuming that all the Joule heat dissipated in the sample transfers to the phonons within the sample volume. If we try to interpret the value of α_0 obtained from Figure 5.3 this way, we find $\alpha_0 = 2 \times 10^{10}$ s^{-1}K^{-2}, which is a factor 7 larger (1 K) than the value obtained by Dorozhkin et al.[6] The discrepancy reflects the fact that the heat in the electron system diffuses out the leads, and therefore has a larger volume in which to transfer to the phonon system. Nevertheless, our estimate of the temperature dependence of the electron-phonon coupling may still be valid. Our value $p = 2.0 \pm 0.2$ is lower than the value p = 3 obtained by Dorozhkin et al.[6] in a low-temperature heating experiment, but it is consistent with the values between 2 and 2.5 obtained from weak-localization studies carried out at higher temperatures,[7] including those in reference [6].

The above analysis presents a consistent, but not unique, explanation of the data in Figure 5.3. An alternative explanation for an observed value of p = 2 has been proposed recently by Kanshar, Wybourne and Johnson[11], who point out that the heating model leading to equation (5.1) assumes good thermal coupling between the phonons in the films and substrate. By allowing the coupling to vary, these authors show that data from a heating experiment can obey a power law

varying anywhere from p = 2 to p = 3. According to this work, the 100 nm thick oxide on our substrate may reduce the high-frequency component of the phonon coupling between film and substrate. Another concern is our estimate of the electron-phonon scattering rate, $\tau_{el\text{-}ph}^{-1} = \alpha_0 T^p$, based on reference [6]. The experiments of reference [7] give p = 2, and $\alpha_0 = 2 \times 10^{10}$ $s^{-1}K^{-2}$. With this larger value of α_0, we find $\kappa_{sub} \approx 0.6$ $\kappa_{el\text{-}ph}$ independent of temperature, so our assumption that the electrons heat while the phonons stay cold may be questionable. We also find with this value of α_0 that the thermal conductance out the leads is less important, and our measured value $\alpha_0 = 2.2 \times 10^{10}$ $s^{-1}K^{-2}$ agrees fortuitously with the values from reference [7]. We cannot distinguish between these interpretations of our data, but we can assert that our measured value of α_0 represents an upper bound on the electron-phonon scattering rate in our sample.

5.3 Attempt to measure Electron Temperature based on Universal Conductance Fluctuations Theory

In our experiment, we tried to measure the electron temperature directly, based on the temperature dependence of the amplitude of the resistance fluctuations, δR. We can compare the observed behavior of δR, shown in the Figure 5.5, with that predicted by the theory of universal conductance fluctuations.[12-13] Near 1 K, the phase coherence length, L_ϕ, in our sample is between 0.1 and 0.2 μm.[14] Thus the sample is just barely in the 1-D limit, defined by $L_x, L_y < L_\phi < L_z$, where L_x, L_y and L_z are again the sample thickness, width and length, respectively. In this limit, $\delta R \propto L_{min}^2 \cdot L_\phi^{1/2}$, where L_{min}

is the smaller of L_ϕ and thermal length L_T. At these low temperatures we expect $L_\phi \propto T^{-1/2}$, due to electron-electron scattering, hence $\delta R \propto T^{-5/4}$. The observed dependence is about T^{-1}, which is rather good agreement. As the temperature is lowered, the sample dimensionality will cross over to 0-D when L_ϕ becomes comparable to the sample length of 0.5 μm. In this regime the theory predicts $\delta R \propto L_\phi^{-1/2} \propto T^{-1/4}$, which is consistent with the roll-off seen in the Figure 5.5 at the lowest temperatures.

Since δR depends only on L_ϕ and L_T, both of which depend only on the electron temperature, we hoped that δR would serve as a good electron thermometer. Figure 5.6 shows a plot of the electron temperature, deduced from δR, versus drive current. These data were taken simultaneously with those shown in Figure 5.3. Unlike the data in Figure 5.3, however, the data in Figure 5.6 can not be fit with equation (5.1), because the electron temperature, T_{el}, does not asymtotically vary as a power law with drive current. In addition, T_{el} appears to increase with drive current initially much faster than the defect temperature, T_{def}. This latter observation would be plausible if the defect were only weakly coupled to the electrons, but in the present circumstance we find it disturbing. Given the choice between our two thermometers, we trust more the reliability of the defect thermometer because of its connection to statistical mechanics. We do not know why δR does not serve as a reliable electron thermometer, but we mention incidentally that Bergmann et al.[15] found the Coulomb-interaction resistance anomally to be a poor thermometer in a heating study of gold films, possibly due to violations of Ohm's law.

Reference

1. M. L. Roukes et al. Phys. Rev. Lett. **55**, 422 (1985).
2. See "Quantum Tunneling in Condensed Matter", ed. Yu. Kagan and A. J. Leggett, Elsevier, New York 1993; also A. J. Leggett et al., Rev. Mod. Phys. **59**, 1 (1987) and references therein.
3. H Grabert, Phys. Rev. **B 46**, 12753 (1992). Grabert's form for the spectral density of bath excitations can be written as $J(\omega) = K\omega(1+(\hbar\omega / k_B T_{ph})^2 / 2\pi K)$, where $K \approx 0.2$ is the coupling parameter between the defect and electron-hole excitations. The ratio of phonon coupling to electron coupling is then roughly $0.25(T_{lattice} / T_{ph})^2$, where $T_{lattice}$ is the actual lattice temperature in the experiment, and $T_{ph} = 0.95$ K, from Figure 5.4.
4. P. W. Anderson, E. Abrahams and T. V. Ramakrishnan, Phys. Rev. Lett. **43**, 718 (1979).
5. M. R. Arai, Appl. Phys. Lett. **42**, 906 (1983). Arai justifies the concept of "electron temperature" without assuming that electron-electron collisions occur more frequently than electron-phonon collisions. This latter condition is nonetheless true in disordered metals below a few K.
6. S. I. Dorozhkin, F. Lell and W. Schoepe, Solid St. Comm. **60**, 245 (1986).
7. F. Komori, S. Kobayashi, and W. Sasaki, J. Phy. Soc. Jap. **52**, 4306 (1983); also P. H. Woerlee, G. C. Verkade and A. G. M. Jansen, J. Phys. C: Solid St. **16**, 3011 (1983).
8. We follow the point of view of refs. 1, 4 and 5 here, where the phonon-substrate coupling is characterized by a thermal conductance, κ_{sub}. At higher temperatures, it may be necessary to consider a more sophisticated model that treats each phonon frequency independently. See ref. 11 , based on the model of N. Perrin and H. Budd, J. Phys. (Paris) Colloq. **33**, C4-33 (1972).

9. We use the same value for the thermal boundary resistance as in ref. 1, taken from W. A. Little, Can. J. Phys. **37**, 334 (1959). Many solid-solid interfaces have similar values of thermal boundary resistance, c.f. E. T. Swartz and R. O. Pohl, Rev. Mod. Phys. **61**, 605 (1989).

10. N. E. Phillips, Phys. Rev. **118**, 644 (1960). Our guess for γ_{el} in our Bi film is based on the discussion in ref. 14 and refs. therein.

11. M. Kanshar, M. N. Wybourne, and K. Johnson, Phys. Rev. **B 47**, 13769 (1993). See also J. C. Nabity and M. N. Wybourne, J. Phys. Cond. Matt. **2**, 3125 (1990).

12 B. L. Al'tshuler and B. Z. Spivak, Pis'ma Zh. Eksp. Teor. **42**, 363 (1985) [JEPT Lett. **42**, 447 (1985)]; S. Feng, P. A. Lee and A. D. Stone, Phys. Rev. Lett. **56**, 1960, 2772 (1986).

13. The UCF calculation is strictly valid only for an ensemble of defects.

14. N. O. Birge, B. Golding, and W. H. Haemmerle, Phys. Rev. **B 42**, 2735 (1990).

15. G. Bergmann, W. Wei, Y. Zou and R. M. Mueller, Phys. Rev. **B 41**, 7386 (1990).

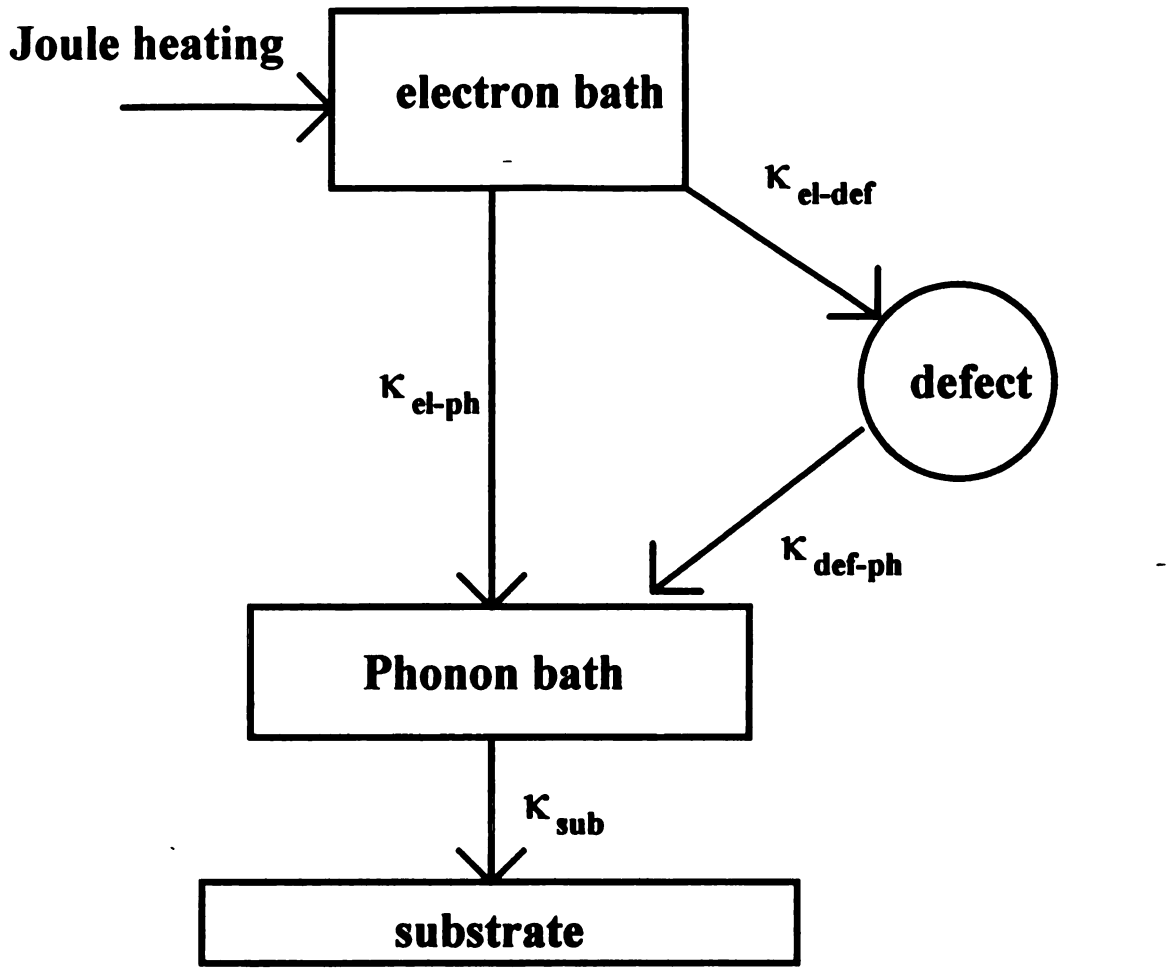

Figure 5.1 Simplied schematic diagram of energy transfer from the electrons to defect and to the phonon bath. κ is a thermal conductance.

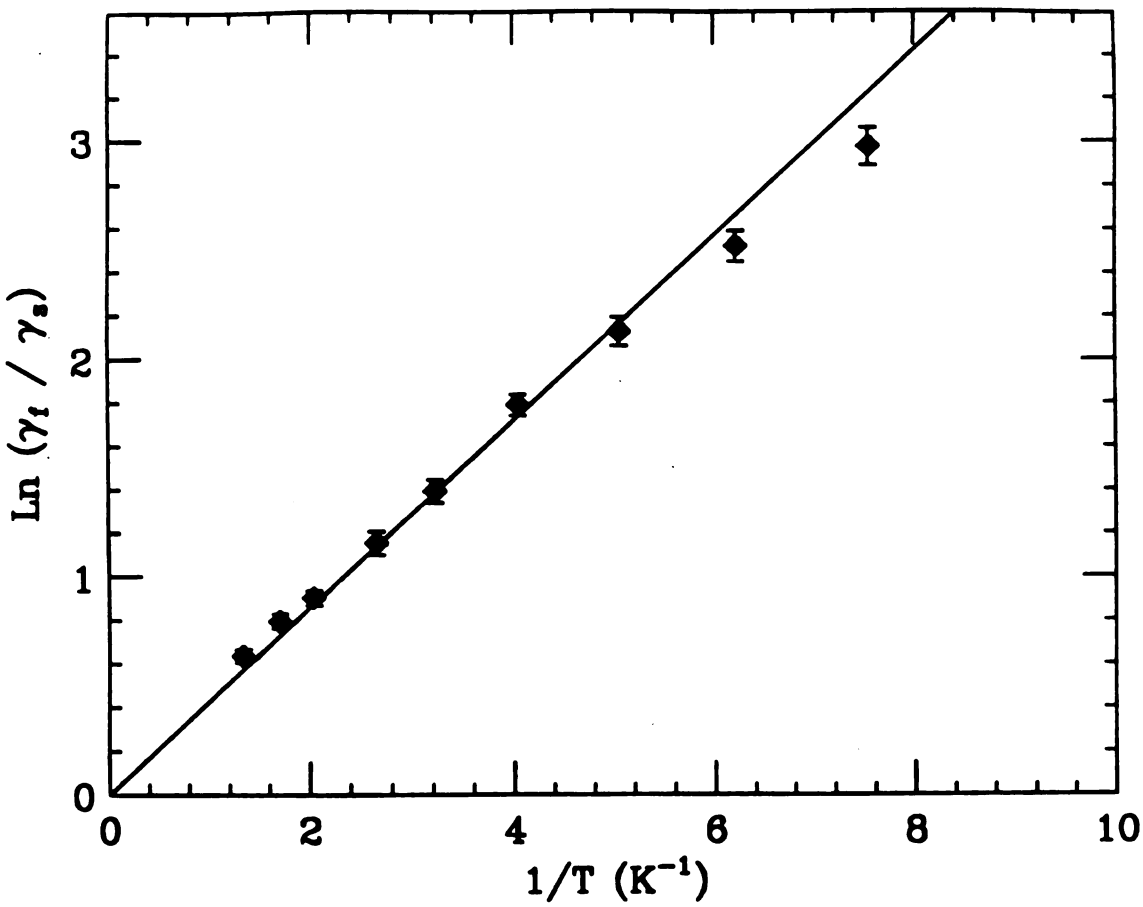

Figure 5.2 *Ln* (γ_f / γ_s) versus $1/T$ at B = 6.997 T. The transition rates obey the detailed balance relation with a slope of 0.42±0.02 K.

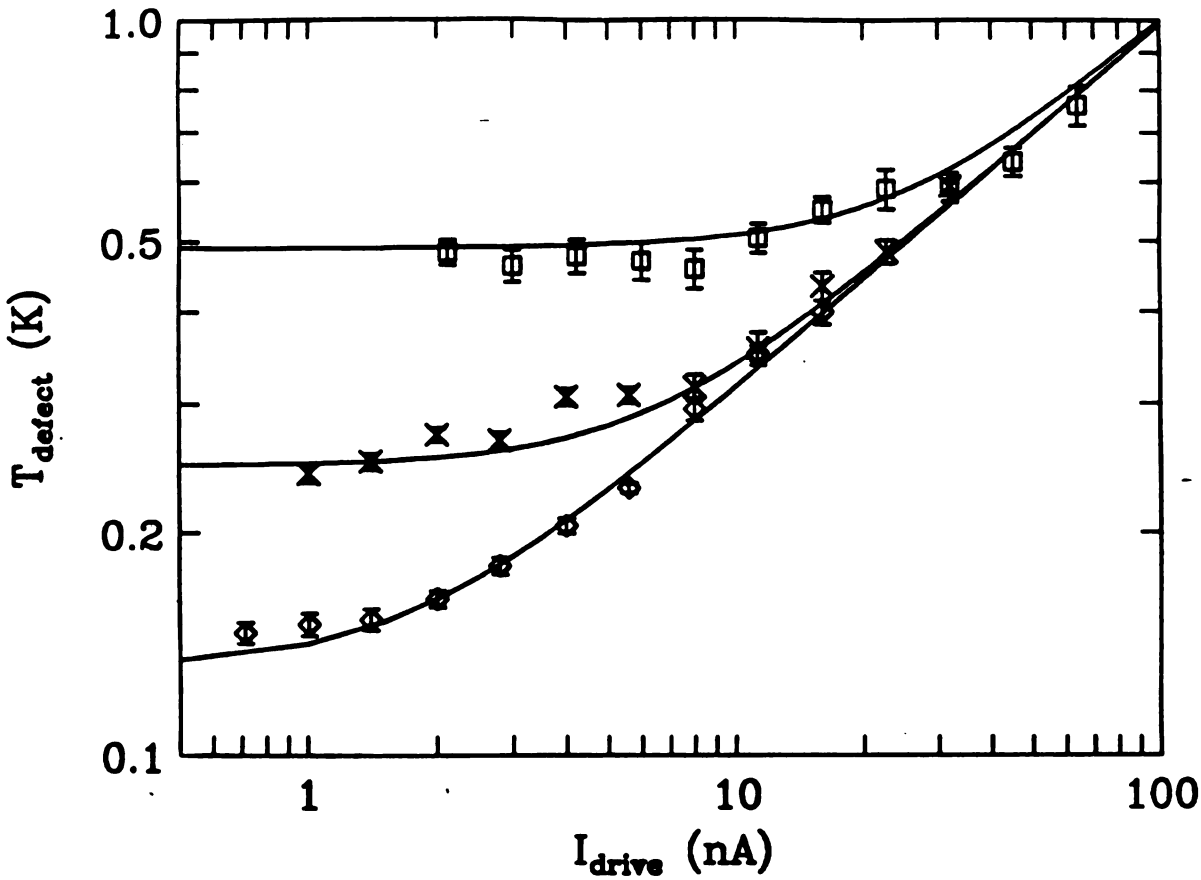

Figure 5.3 Log-log plot of defect temperature versus drive current, for three different values of the lattice temperature, $T_{lattice}$ = 0.132, 0.247 and 0.490 K. The defect temperature is determined from the ratio of fast and slow transition rates via the detailed balance relation. The solid lines represent a global least-squares fit of the data to Equation 5.1 with two parameters, p = 2.0 and $\alpha_0\gamma_{el} = 4.5\times10^{10}$ W/K^{4}m^3.

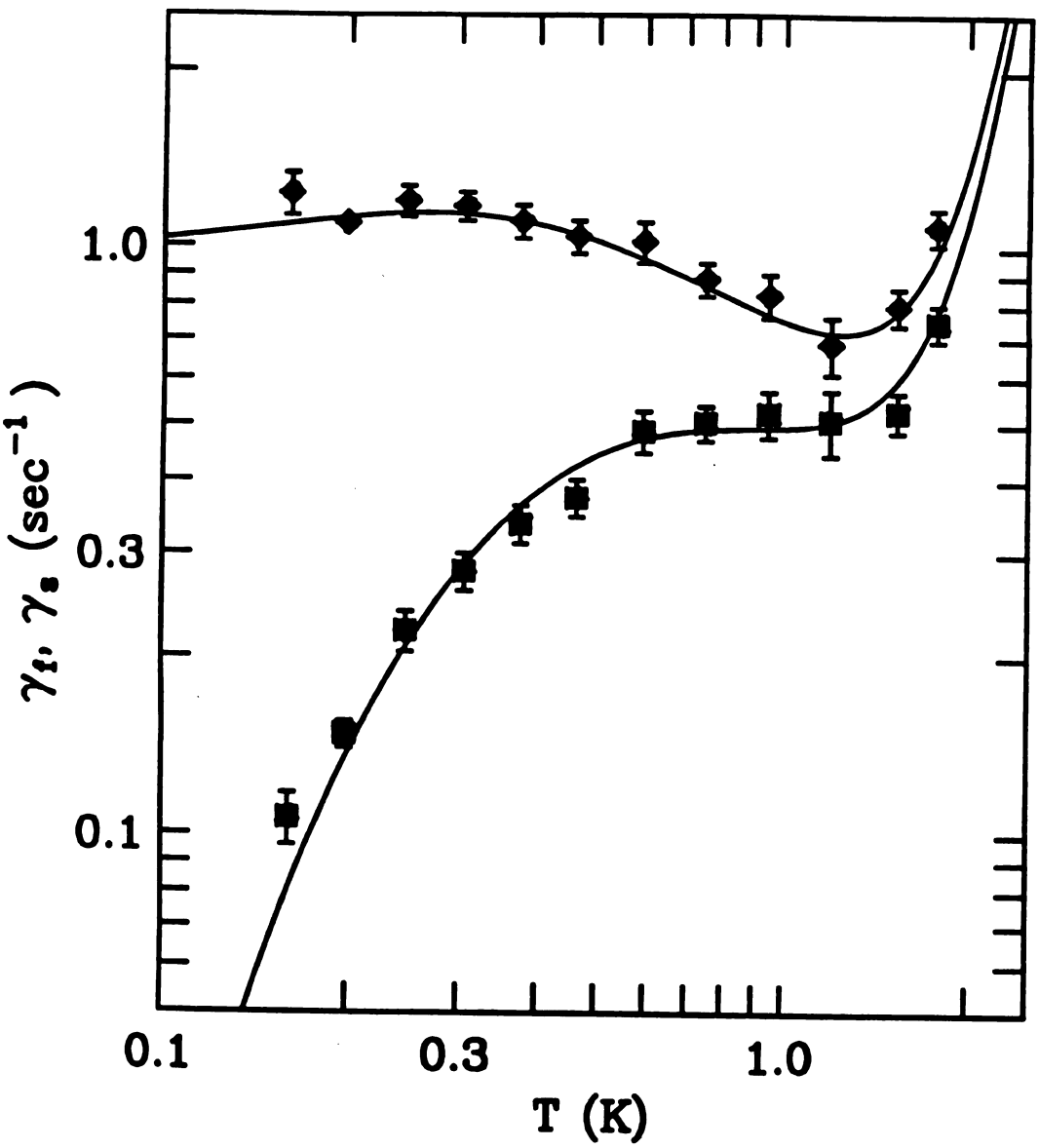

Figure 5.4 Log-log plot of fast and slow transition rates versus temperature at B = 6.997 T. The solid line is a least-squares fit to the theoretical function calculated by Grabert in ref. 3. The crossover between electron-dominated and phonon-dominated tunneling occurs at $T_{ph} \approx 0.95$ K.

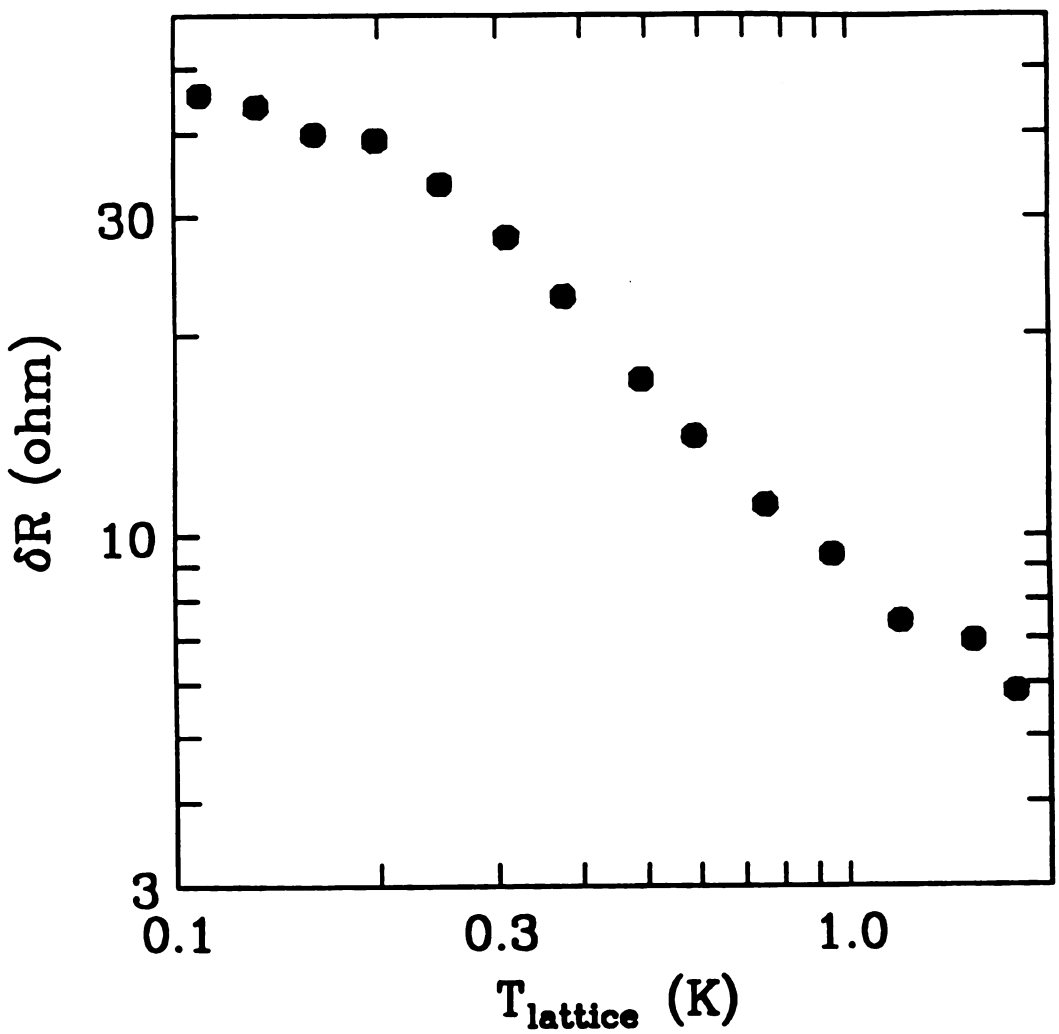

Figure 5.5 Plot of the amplitude δR of the defect resistance jump versus temperature. The increase of δR with decreasing temperature is due to the universal conductance fluctuation mechanism.

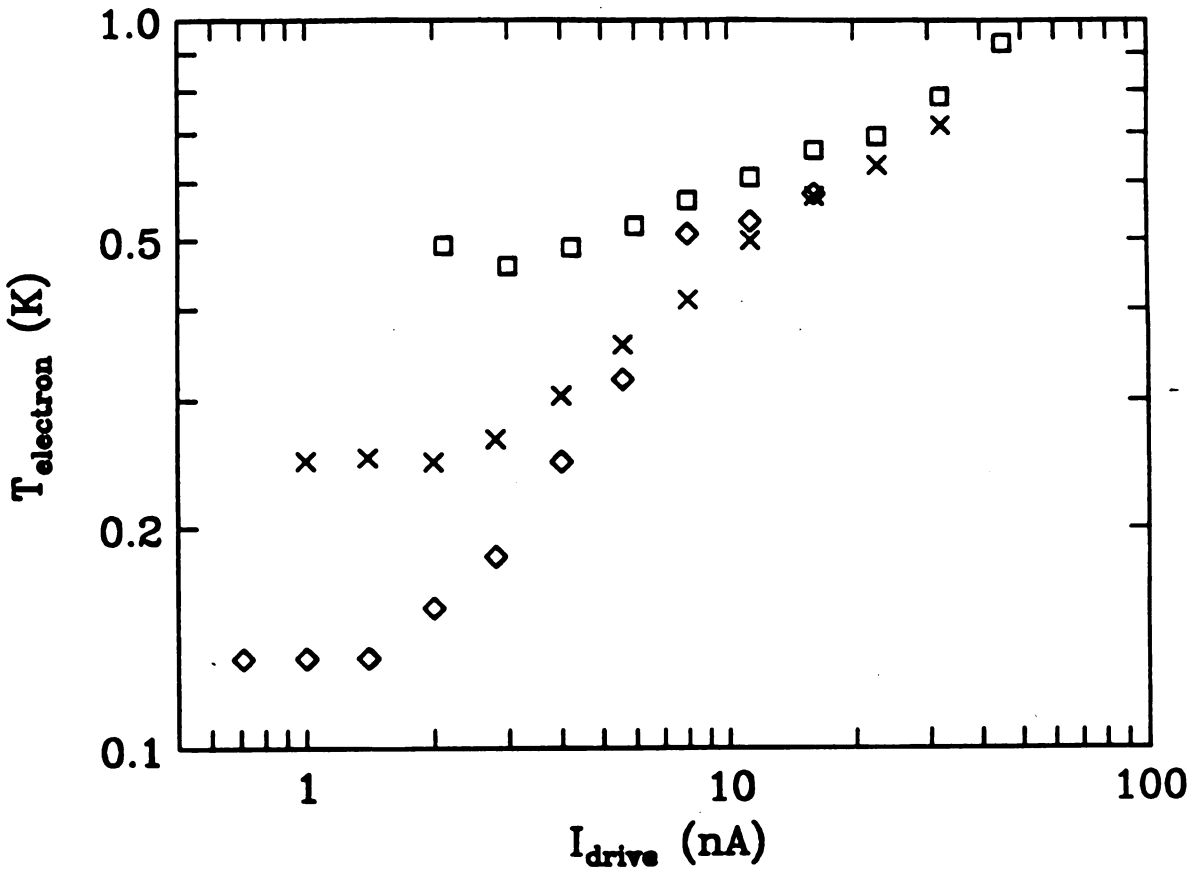

Figure 5.6 Log-log plot of electron temperature versus drive current, for the same three lattice temperatures shown in Figure 5.3. The electron temperature is deduced from the amplitude of the defect resistance jump δR. These heating data do not obey Equation 5.1.

Chapter 6

Summary

We have measured the tunneling rates of a single defect in a metal over a broad range of temperature and magnetic field. Our work covers the temperature range from 0.1 K to 2 K, which allows us to make a thorough comparison between experiment and theory. Above 1 K, the rates increase rapidly, due presumably to phonon-assisted tunneling. Below 1 K, the temperature dependence of the defect tunneling rates agrees quantitatively with predictions of dissipative quantum tunneling theory, spanning the temperature range from $k_B T << \varepsilon$ to $k_B T >> \varepsilon$. We also observe a random variation of the defect energy asymmetry ε, with magnetic field, but the minimum value of ε for this particular defect occurs for $B \neq 0$. Our data are consistent with the hypothesis that the defect-electron bath coupling constant, α, is independent of field. These results illustrate the power of conductance measurements of mesoscopic samples to obtain microscopic information about individual defects. Such experiments are especially useful in the study of disordered materials, where the microscopic parameters characterizing the defects are broadly distributed.

In an electron heating experiment, we have shown that the transition rates of a single defect can be used as a local thermometer under non-equilibrium conditions, via the detailed balance relation. We have used this defect thermometer to study electron heating in a submicron Bi sample, and we find the results consistent with a simple

heating model, where the electron-phonon scattering rate is proportional to T^p with p = 2. An electron thermometer based on the the amplitude of the dynamic universal conductance fluctuations does not follow the simple heating model. We can not obtain the absolute electron-phonon scattering rate from this experiment, due to the nonuniform temperature profile of the hot conduction electrons in the sub-micrometer sample.

Appendix A

$1/f$ noise spectrum

The standard way to measure resistance fluctuations of a resistor is to apply a constant current through the sample, and monitor the voltage across the sample as a function of time. The noise is usually characterized by an autocorrelation function

$$K_V(t) = \langle \delta V(\tau)\, \delta V(\tau + t) \rangle$$

where $\delta V(t) = V(t) - \langle V \rangle$, and the brackets refer to a time average over all times τ. This autocorrelation function contains information about the noise in the time domain. The power spectrum of the voltage noise is then given by

$$S_V(\omega) = \frac{1}{2\pi} \int_{-\infty}^{\infty} K_V(t)\, e^{-i\omega t}\, dt$$

At high frequencies, the noise spectrum is roughly flat, and its magnitude is determined by the Nyquist-Johnson formula, $S_0 = 4k_B T \langle R \rangle$. At low frequencies, a noise called "flicker noise" of the spectral form $S_V(\omega) \propto 1/\omega$ $(\omega = 2\pi f,\ S_V(f) = 2\pi S_V(\omega))$ is observed in most of the metallic systems. This is the $1/f$ noise. The $1/f$ noise is due to fluctuations in the sample resistance, and obeys Ohm's law: $S_V(\omega) = I^2 S_R(\omega)$.

The resistance noise spectrum is given as a superposition of contributions from all moving defects, each having some typical time scale τ. One has

$$S_R(\omega) \propto \int d\tau\, D(\tau) \frac{\tau}{1+(\omega\tau)^2}$$

where $D(\tau)$ is the distribution of characteristic time constants of the moving defects. The function $\tau/\left[1+(\omega\tau)^2\right]$ is the Debye-Lorenzian power spectrum of a fluctuating two-state defect having a characteristic time scale τ.

At high temperature, the motion of defects is thermally activated, so for a given defect one has $\tau = \tau_0 \exp(E/k_B T)$, where E is the activation energy barrier for the defect to hop from one site to another and $1/\tau_0$ is the attempt rate. If there is a distribution of such activation energies, $D(E)$, which has a regime where $D(E)$ is constant for $E_{\min} < E < E_{\max}$, then one has $D(\tau) \propto 1/\tau$ for the time interval $\tau_{\min} < \tau < \tau_{\max}$, where $\tau_{\min} = \tau_0 \exp(E_{\min}/k_B T)$ and $\tau_{\max} = \tau_0 \exp(E_{\max}/k_B T)$. This then leads to a $1/f$ spectrum of $S_V(f)$ for $\tau_{\max}^{-1} << \omega << \tau_{\min}^{-1}$. This behavior is shown in schematic diagrams in Figure A.

At low temperatures, defects move via quantum tunneling. By a similar argument as the one described above, the conductance fluctuations have low frequency $1/f$ noise due to the distribution of tunneling rates in a disordered material. The tunneling time scale depends exponentially on the barrier height and barrier width. Assuming that the barrier height is broadly distributed, the same argument as above leads to $1/f$ noise.

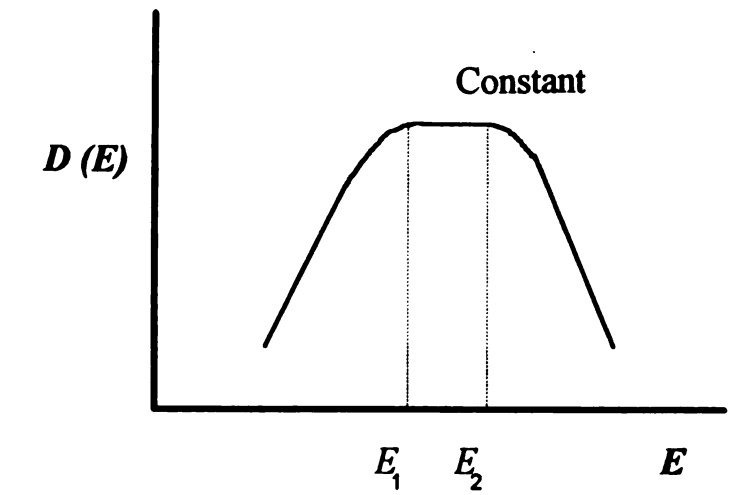

(a)

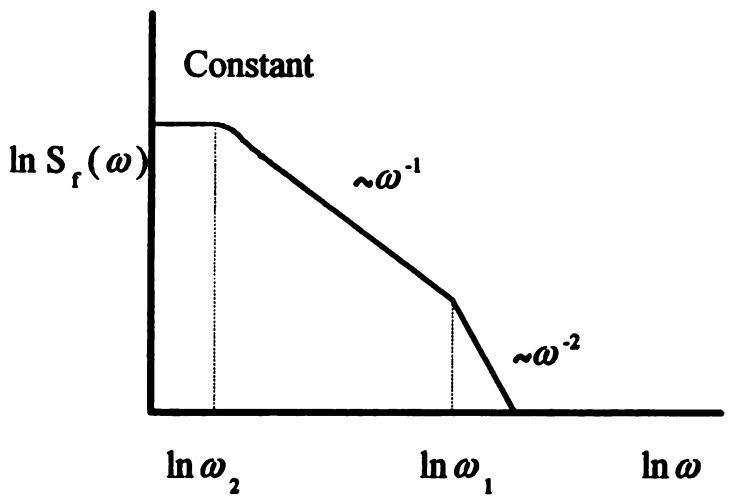

(b)

Figure A (a) "Flat" energy distribution of thermally activated process. (b) Frequency spectrum resulting from this distribution.

Appendix B

Thermometer Calibration in a magnetic field

The fitting function for the correction of magnetoconductance of the carbon thermometer is

$$\frac{G(T,B)}{G(T,0)} = 1.00 + \frac{a(T)}{B} \cdot (b(T) - B + d(T)B^2) \cdot \frac{c(T)}{e^{a(T)/B} - 1}$$

The coefficients $a(T)$, $b(T)$,$c(T)$ and $d(T)$ are given as polynomial functions of magnetoconductance of zero field $G(T,0)$ such that

$$a(T) = a_0 + a_1 \cdot G(T,0) + a_2 \cdot G(T,0)^2$$
$$b(T) = b_0 + b_1 \cdot G(T,0) + b_2 \cdot G(T,0)^2 + b_3 \cdot G(T,0)^3 + b_4 \cdot G(T,0)^4$$
$$c(T) = c_0$$
$$d(T) = d_0 + d_1 \cdot G(T,0) + d_2 \cdot G(T,0)^2 + d_3 \cdot G(T,0)^3 + d_4 \cdot G(T,0)^4$$

where the coefficients are

$a_0 = 0.2476$, $a_1 = -0.08853$, $a_2 = 0.02137$

$b_0 = 10.0561$, $b_1 = -8.5684$, $b_2 = 3.5406$, $b_3 = -0.65894$, $b_4 = 0.04894$

$c_0 = 0.0114$

$d_0 = -0.0270$, $d_1 = -0.0857$, $d_2 = -0.0418$, $d_3 = -0.0089$, $d_4 = -0.0007$

Figure B shows the good fits of $G(T,B)/G(T,0)$ to the data for three different nominal temperatures.

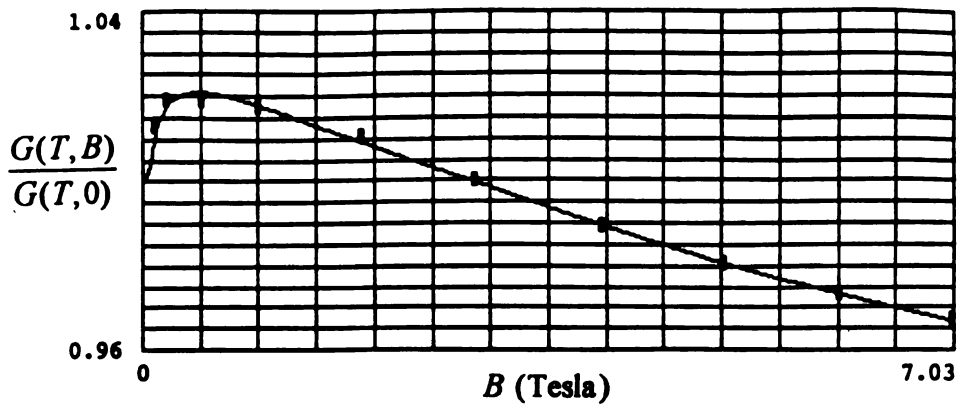

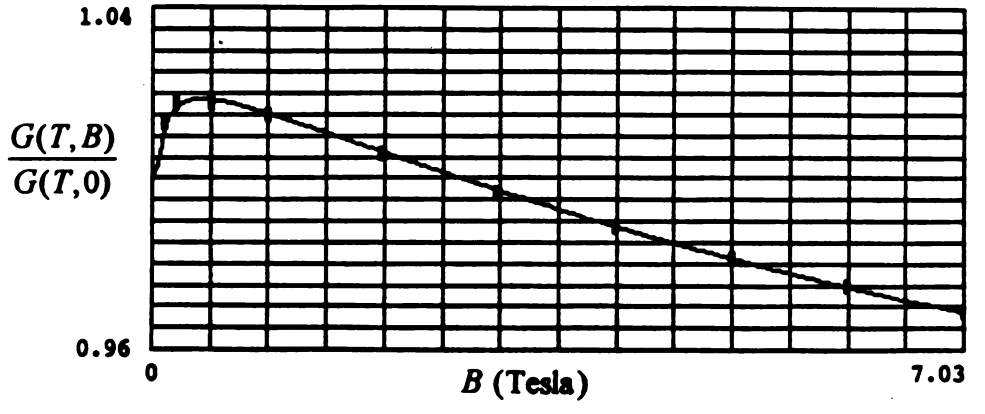

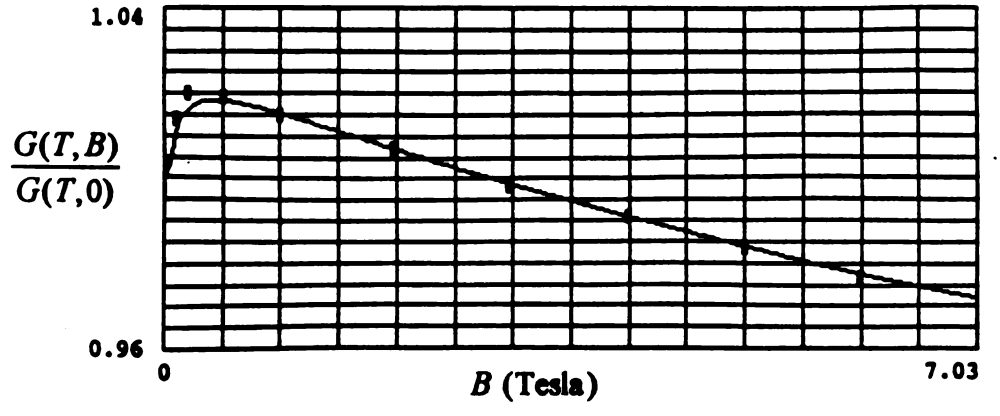

Figure B. Plot of magnetoresistance of the carbon thermometer versus magnetic field for three different values of the nominal temperature, 565, 400 and 283 mK. The solid line is the function $G(T,B)/G(T,0)$ calculated with different values of the coefficients $a(T)$, $b(T)$, $c(T)$ and $d(T)$.